Doctoral Dissertation
博士論文

An observational study of ejecta in supernova remnants using spatially resolved X-ray spectroscopy
（超新星残骸のX線観測による爆発噴出物の研究）

A Dissertation Submitted for the Degree of Doctor of Philosophy

December 2021
令和3年12月博士（理学）申請

Department of Physics, Graduate School of Science,
The University of Tokyo
東京大学大学院理学系研究科
物理学専攻

Tomoaki Kasuga
春日　知明

Abstract

Type Ia supernovae are the main factory of iron-group elements in space and important probes to measure the distance to distant galaxies as "standard candles" thanks to the uniformity of their light curves. However, the origin of these supernovae is proposed to have some diversities: whether the counterpart of the parent binary is a non-degenerate star (single degenerate scenario) or another white dwarf (double degenerate scenario)? This makes differences of the process toward the explosion and affects the properties of its supernova as the production mass of iron-group elements. One of the main differences after the explosion in each scenario is the existence of the dense circumstellar media in addition to pre-existing interstellar media. The single degenerate origin supernova leaves remaining accreting matters or blown off out-layer of the counterpart, in addition to the ejected materials.

The X-ray observation of the remnant object of supernovae (supernova remnants) is one of the powerful methods to search such circumstellar media. In addition to the direct detection of emissions from them, the kinematics of the ejecta can also help us. Their dynamics must be inhibited by such a dense environment they feel. The supernova ejecta emit characteristic X-rays after being heated by shocks up to $\sim 10^7$ K. By measuring the Doppler velocity of emission lines, we can estimate the line-of-sight velocity structure of the ejecta. Using this information, we approach the interaction of the ejecta and the environment.

In this thesis, we choose two young type Ia supernova remnants in the ejecta dominant phase, named Kepler and Tycho. The former one is reported with strong X-ray emission from the dense circumstellar media. The high-resolution spectroscopy by a grating detector shows the deceleration of ejecta with $\sim$1,000 km sec^{-1} in our side and the shrinkage of the kinematics at the central torus. The latter one is not reported with any X-ray emission from both circumstellar and interstellar media. Our spatially resolved X-ray spectroscopy by CCD detectors shows, on the other hand, its deceleration with $\sim$2,500 km sec^{-1} in the all azimuth angle of this remnant.

Both of our results suggest the existence of the circumstellar media in each supernova remnant, which supports the single degenerate scenario for their origin. The difference in the X-ray morphology could be due to the timing of the interaction or their production mechanism.

Contents

List of Figures

List of Tables

Table 0: Abbreviation list

Abbreviation	Definition
ACIS	Advanced CCD Imaging Spectrometer
AGB	Asymptotic Giant Branch
AGN	Active Galactic Nucleus
AOCS	Attitude & Orbit Control Subsystem
ARF	Auxiliary Response File
AtomDB	Atomic DataBase
CC	Core-Collapse
CCD	Charge-Coupled Device
CCF	Current Calibration File
CD	Contact Discontinuity
CI	Charge Injection
CIAO	Chandra Interactive Analysis of Observations
CIE	Collisional Ionization Equilibrium
CMOS	Complementary MOS
CSM	CircumStellar Media
CTI	Charge Transfer Inefficiency
CXB	Cosmic X-ray Background
DD	Double Degenerate
D^6	Dynamically-Driven Double-Degenerate Double-Detonation
DDT	Deflagration-Detonation-Transition
DOF	Degree Of Freedom
EPIC	European Photon Imaging Camera
ESA	European Space Agency
eV	electron Volt
FOV	Field-Of-View
FS	Forward Shock
FWHM	Full Width at Half Maximum
GTI	Good Time Interval
HEASoft	High Energy Astrophysics Software
HRMA	High Resolution Mirror Assembly
IGE	Iron Group Elements
IME	Intermediate Mass Element
ISM	InterStellar Media
keV	kilo electron-Volt

Table 0: `(continued)`

Abbreviation	Definition
NASA	National Aeronautics and Space Administration
NEI	Non-Equilibrium Ionization
MOS	Metal-Oxide Silicon
NXB	Non X-ray Background
ODF	Observation Data File
OM	Optical Monitor instrument
SAS	the *XMM-Newton* Scientific Analysis System
SD	Single Degenerate
SN	SuperNova
SNR	SuperNova Remnant
SXS	Soft X-ray Spectrometer
RFC	RGS Focal plane Camera unit
RG	Red Giant
RGA	Reflection Grating Array
RGS	Reflection Grating Spectrometer
RMF	Response Matrix File
RS	Reverse Shock
WD	White Dwarf
XRS	X-Ray Spectrometer
XSPEC	X-ray SPECtral fitting package

Chapter 1

Introduction

A supernova, the explosion at the moment of the death of a star, is one of the most energetic phenomena in the universe. Supernovae play an important role for humanity as a factory of "heavy" elements. Baryonic matter distributed to interstellar space mostly consists of hydrogen and helium, and other heavier elements have mainly been generated in the core of stars by nuclear fusion processes. Although recent studies have revealed significant contributions of neutron-star mergers for r-process elements, elements up to the iron group are still thought to be mainly produced at the supernova explosions. Supernovae are the only phenomena for distributing such elements to the interstellar space as the ejecta. Therefore, we owe what we are to supernovae.

Although supernovae are in a sense critical phenomena for us, the explosion mechanism and their evolution are not clearly understood. This thesis picks up the thermonuclear burning type supernovae, called type Ia. Type Ia supernovae are adopted as a "standard candle" because of their uniformity of the optical light curve at the moment of explosion. However, this uniformity is still phenomenological. In the first place, the origin of type Ia supernovae is not determined. This explosion is generally accepted to be occurred at a white-dwarf in a binary system, but we have mainly two scenarios for the counterpart of it; a non-degenerated star like a red-giant for the single degenerate scenario and another white-dwarf for the double degenerate scenario. The white-dwarf mass at the moment of the former scenario reaches near-Chandrasekhar mass, in contrast to the latter one which does not need to this condition. The mechanism of the ignition to the explosion is also not simple. Many theoretical models have proposed how ignition flames are accelerated toward the sonic speed and how many ignition points they have. We need to admit such varieties in type Ia supernovae in spite of the similarity of their light curves. Thus, one of the most important interests in this field focuses on distinguishing them and determining the fractions of their contributions.

However, these explosion scenarios make an obvious difference for us; how the iron group elements are produced by one supernova. Type Ia supernovae produce that group of elements more than other types, and especially the single degenerate scenario plays this role because irons are mainly produced at the core of near-Chandrasekhar white-dwarf. High spectroscopy observation of Perseus cluster measured iron group element abundance (Hitomi Collaboration et al., 2017) and revealed that we need both scenarios to explain the chemical composition of the iron group elements what we observe now. However, the present observational efficiency for detecting such elements is not sufficient to distinguish each type for a single event of supernova.

This study focuses on another major difference. The remaining accreting flow or the companion star in the single degenerate scenario constitutes circumstellar media associated with the explosion system. The existence of circumstellar media can be a strong diagnostics to distinguish explosion scenarios. To search for them, we observe the remnant objects of supernovae, called supernova remnants. Supernova remnants consist of ejecta materials, circumstellar media, interstellar media, and shock waves if they exist. Unlike supernovae as compact objects, supernova remnants are extended sources and can be resolved spatially. They are suitable for studying details of supernovae.

As a probe, we observe the X-ray emission from supernova remnants, which is emitted from materials heated up to $\sim 10^7$ K by shocks. Some studies directly observe the emission from circumstellar media. This method is definitive in the positive detection cases, but we cannot easily determine whether there are no materials or existing matter that do not radiate X-ray emission when X-rays are not detected. Our study instead observes emission from the ejecta elements and measures their kinematics. The ejecta kinematics will be affected by the environment surrounding the supernova. Such kinematic probes will give an indirect evidences of unshocked matter around the remnant.

Measuring motions of emission sources in the angular direction can be simply concluded by comparing differences of the snapshots of 2-dimensional X-ray images faced on us at different timing. However, the supernova remnants have a 3-dimensional structure. Our study focuses on the kinematics in the line-of-sight direction instead. Combining both information, we for the first time know the 3-dimensional feature.

This thesis is organized as follows. At first, we review the properties of type Ia supernovae and their remnants in Chapter 2, and the X-ray observatories *XMM-Newton* and *Chandra* in Chapter 3. In Chapter 4, we select a famous type Ia supernova remnant, Kepler, as a representative of those with strong emission from circumstellar media, and analyze it by spatially resolved spectroscopy. We also analyze it by high resolution spectroscopy in Chapter 5, and discuss the kinematics of Kepler in Chapter 6. Chapter 7 analyzes another remnant, Tycho, without direct emission from circumstellar media also by spatially resolved spectroscopy, and we discuss the kinematics in Chapter 8. Finally, we unify the discussion on our results of two different characteristic type Ia supernova remnants in Chapter 9. In addition to the main thesis, we point out a critical trouble occurred in an observation data set of Tycho by a *Chandra* detector in Chapter A.

Chapter 2

Reviews of supernovae and supernova remnants

2.1 Supernovae

Stars are generated from the gas of InterStellar Media (ISM). Its mass is conventionally normalized by that of the sun, $M_\odot$. Except for very light stars <0.08 $M_\odot$, which contain only hydrogen and will be brown dwarfs, main sequence stars >0.08 $M_\odot$ will cause nuclear fusion at their core. The death of main-sequence stars is an explosion called SuperNova (SN). SNe are historically classified into some types. According to its optical spectrum, type I and II SNe are defined by the absence or existence of the hydrogen absorption lines, respectively (Minkowski, 1941). In type I, type Ia has a deep absorption line of $\lambda6355$ from silicon, which represents the line whose wave length is 6355 Å. Type Ib has instead $\lambda5876$ from helium, and the remaining exceptions are classified to type Ic.

In terms of the explosion mechanism, type Ib, Ic, and all type II are Core-Collapse explosions (CC). Their gravitational energy is supported by the energy emission from nuclear fusion at their core. This equilibrium comes failure at the moment of generating a nickel-iron core which is the terminal of the fusion process, and the core starts collapsing with the photodisintegration of iron. The bounce of this rapid collapse proceeds nuclear fusion of outer layers and causes an explosion. On the other hand, only the type Ia SNe has completely different process, therefore we mainly classify SNe into type Ia vs CC. Following subsections describe reviews on type Ia SNe.

2.1.1 Overview of type Ia supernovae

In the core of light stars $<4\ M_\odot$, the nuclear fusion proceeds to generate a carbon+oxygen core, and they remain as a White Dwarf (WD). A WD supports the gravitational pressure due to its own mass M by the electron degeneracy pressure. There exits the upper limit of M because the gravitational pressure could exceed the electron degeneracy pressure when the mass exceeds it. This limit is called Chandrasekhar limit $M_{\rm Ch}$ (cf., Chandrasekhar, 1935). Although the $M_{\rm Ch}$ has a slight range of 1.38–1.44 $M_\odot$ and there remains questions whether and how M close to $M_{\rm Ch}$, type Ia SNe shows relative uniformity compared with CC SNe, thanks to the common value $M_{\rm Ch}$. At the moment of explosion, the explosion energy from thermonuclear burning overcome the gravitational energy. There seems to be $\sim 0.6\ M_\odot$ of ^{56}Ni as the main product, and the energy released for burning from C+O to ^{56}Ni is estimated to $E_0 \sim 10^{51}$ erg, or $\sim 10^{44}$ J. The maximum optical luminosity is achieved to $\sim 10^{43}$ erg sec^{-1}. The main process of optical emission after the explosion is the radioactive decays of $^{56}\mathrm{Ni} \rightarrow {}^{56}\mathrm{Co} \rightarrow {}^{56}\mathrm{Fe}$ in 9 and 114 days, respectively. Thus, the final product of type Ia SNe is mainly iron, in contrast to CC SNe with deconstructing Iron. This uniformity of its maximum luminosity and decay time, called Phillips relation (Phillips, 1993), help us to measure the distance to the emission source. Therefore, type Ia SNe are known as "standard candles" in cosmology. For example, Riess et al. (1998) and Perlmutter et al. (1999) measured the distance to many type Ia SNe and revealed the accelerating universe.

2.1.2 Origins of type Ia supernovae

Despite general acceptance of type Ia SNe as a useful standard candle, the progenitor origin is not fully understood. We have mainly two different scenarios. One is a WD with a non-degenerate companion star, which is called Single Degenerate scenario (SD) (Whelan & Iben, 1973). In an SD situation, a WD gets its mass by the accretion from its counterpart toward $M \sim M_{\rm Ch}$. So it is generally not a mistake that we regard this scenario as a near-$M_{\rm Ch}$ explosion. The companion star could still remain at the moment of the explosion and after long years. The other scenario is Double Degenerate (DD), which is occurred in a WD-WD binary (Iben & Tutukov, 1984; Webbink, 1984). Such scenario was at first though to result in collapse to a neutron star and not in type Ia (e.g., Nomoto & Iben, 1985). However, recent studies instead have revealed that the merging with high temperature and high density could trigger type Ia SNe even if the mass is not achieved to $M_{\rm Ch}$ (e.g., Pakmor et al., 2012).

It is still investigated how to discriminate the origin of each SN scenario. One of the observable differences remaining after the explosion is the outstanding existence of CircumStellar Media (CSM). The SD scenario is caused by blowing off the non-degenerated companion star. Such materials remain as the CSM and they tend to be denser than the ISM. For example, Hachisu et al. (2008) proposed that the progenitor wind from a WD (Hachisu et al., 1996) stripped the outer layer of its counter part and it results in a torus-like CSM around there. Such materials makes its environment complicated. In the DD scenario, on the other hand, both components of a binary are the degenerated WDs and explodes in the sparse ISM environment. This difference could affect the kinematics of ejected materials of SNe, because dense CSM could inhibit their motion. This is the main motivation of our study.

Another difference is production of Iron Group Elements (IGEs). Different from sub-$M_{\rm Ch}$ explosion of the DD scenario, the electron capture reaction ($\rm p + e^- \rightarrow n + \nu_e$) occurs at the dense core of a WD in the near-$M_{\rm Ch}$ explosion. This reaction create more ^{58}Ni and ^{55}Co because of neutron excess. These elements are observed as ^{58}Ni and ^{55}Mn in the remnant and could be a strong indicator of SD scenario (e.g., Yamaguchi et al., 2015). Hitomi Collaboration et al. (2017) measured the metal abundance in the Perseus cluster, and found we need both scenarios to explain its near-solar abundance ratio of IGEs.

2.1.3 Mechanisms of type Ia supernovae

In addition to the variation of the origin, the mechanism of an explosion is also still in discussion. The propagation process of thermonuclear fusion is classified into mainly two types: deflagration and detonation. The deflagration is subsonic flame and detonation is supersonic. The complicated combination of each flame occurs in the core of a WD. The delayed-detonation, or so-called Deflagration-Detonation-Transition (DDT), is regarded as the main process of near-$M_{\rm Ch}$ (Khokhlov, 1991). In this process, the initial subsonic deflagration at the core is accelerated by turbulence to supersonic speed, and proceeds the nuclear synthesis of outer layers.

Another mechanism is the double-detonation in the sub-$M_{\rm Ch}$ WD explosion (Woosley & Weaver, 1994). The accretion process ignites the WD surface detonation at first, and this detonation triggers another detonation in the core. The violent merging of two double-detonated WDs could occur, which is known as the Dynamically-Driven Double-Degenerate Double-Detonation (D^6) (Shen et al., 2018). Such different mechanisms could make differences of abundance patterns or ejecta kinematics in the remnant objects (e.g., Ferrand et al., 2019, 2021).

2.2 Supernova remnants

For approaching the questions of SNe, especially about type Ia SNe in this thesis, the optical observation of their light curves and spectra is certainly one of the strong clues. However, SN itself is a very compact object and not good for spatially resolved analysis. We have to analyze a contaminated spectrum including many different emissions. Here, we focus on the remnant objects of SNe, which are called SuperNova Remnants (SNRs), for spatially resolved studies.

2.2.1 Components

As we described above, the SN explosion is the only phenomenon for distributing nuclear synthesized heavy elements produced at the core of a WD to the space. Such elements are still observed as ejecta in the SNR phase. They are observed with pre-existing ISM elements. The abundance of the ejecta can be assumed pure-metal where the abundance ratio $[\mathrm{M/H}]/[\mathrm{M/H}]_\odot \gg 1$, whereas the ISM abundance pattern is almost similar to that in the solar system. In addition to these, we can observe elements of the CSM, whose origin is the out layer of stars. CSM is generally observed in CC SNRs because the progenitors of them lose their own mass before explosion and produce a dense environment. Type Ia SNRs do not necessarily require CSM, but the existence of non-degenerated counter part in the SD scenario results in CSM in the remnant, which includes the remains of a stellar wind at the moment of accretion (Hachisu et al., 1996), for example. The abundance of CSM is expected to be also near-solar values but depends on its origin.

2.2.2 Ejecta dominant phase

In the initial phase of SNRs soon after the explosion, the initial velocity of the ejecta reaches $\sqrt{E_0/2M_{\mathrm{ej}}}$ ~10,000 km sec^{-1}, where M_{ej} is the ejecta mass. This velocity is quite higher than the sound speed of the ambient media $\sqrt{\gamma p/n_{\mathrm{p}} m_{\mathrm{p}}}$ ~10 km sec^{-1}, where γ is the adiabatic index, p is the gas pressure, n_{p} is the number density of the ambient media, and m_{p} is the proton mass. This difference generates outward shocks called blast wave or Forward Shock (FS). The forward shock heats the ambient media with sweeping them up. During M_{ej} overwhelms the swept-up mass M_{sw}, the kinematics of the forward shock and ejecta is nearly free expansion. Free expansion means that the shock velocity V_{s} is represented by R_{s}/t, where R_{s} is the radius of the forward shock and t is the age of the remnant. This phase is called the ejecta dominant phase, and their velocities are still observed as ~1 % of the light speed in SNRs whose age is below ~2,000 yr old.

2.2.3 Transition to the Sedov phase

When $M_{\rm sw}$ reaches $M_{\rm ej}$, SNRs transits into the Sedov phase (Sedov, 1959). Note that this Sedov phase is sometimes called the adiabatic phase, but the ejecta dominant phase is also adiabatic. In the Sedov phase, the forward shock gets decelerated by the swept-up materials. The simplest calculation by assuming uniform density ρ_0 for the ambient media is called the Sedov–Taylor self-similar solution (Taylor, 1950; Sedov, 1959) that:

$$R_{\rm FS} = \left(\xi \frac{E_0 t^2}{\rho_0} \right)^{1/5} , \tag{2.1}$$

$$V_{\rm FS} = \frac{{\rm d}R_{\rm FS}}{{\rm d}t} = \frac{2}{5} \frac{R_{\rm FS}}{t} , \tag{2.2}$$

where ξ is 2.026 for $\gamma_{\rm ad} = 5/3$ as non-radiative monatomic gas. More generally, we assume the density profile as $\rho_{\rm am}(r) \propto r^{-s}$, then:

$$R_{\rm FS} \propto t^{\beta} , \tag{2.3}$$

$$V_{\rm FS} = \beta \frac{R_{\rm FS}}{t} , \tag{2.4}$$

where $\beta \equiv 2/(5-s)$. The $s = 0$ situation is expanding in the uniform ISM, and $s = 2$ suggests accompanying materials like CSM originated from a stellar wind.

However, we should take into account the ejecta there especially in the transition phase of the ejecta dominant phase to the Sedov phase. The outermost ejecta translates its energy to the SNR shell, but the inner ejecta still expands freely. This separation generates another "inward" shock called Reverse Shock (RS) (McKee, 1974). For young SNRs whose age is below ~1,000 yr old, the reverse shock could be expected not to reach the innermost ejecta. Chevalier (1982) introduced the density profile for ejecta as $\rho_{\rm ej}(r) \propto r^{-n}$. The β parameter is changed to that:

$$\beta \equiv \frac{n-3}{n-s} . \tag{2.5}$$

Type Ia SNe expect the $n = 7$ expansion, whereas CC SNe expect larger n. Using more generalized model in Truelove & McKee (1999), which represents smooth transition to the Sedov β, the reverse shock is expected to move "outward" at first (see Figure 5 in Truelove & McKee, 1999). The relationship of the reverse shock velocity in the ejecta-static frame, $\tilde{V}_{\rm RS}$, and that in the observer frame, $V_{\rm RS}$, is that:

$$\tilde{V}_{\rm RS} = \frac{R_{\rm RS}}{t} - V_{\rm RS} , \tag{2.6}$$

$$V_{\rm RS} = \frac{{\rm d}R_{\rm RS}}{{\rm d}t} . \tag{2.7}$$

When $|\tilde{V}_{\rm RS}| < V_{\rm FS}$ at the early stage, the shocked ambient media is still hotter than shocked ejecta. As time goes on, $|\tilde{V}_{\rm RS}| > V_{\rm FS}$ makes the inverse of their temperature. At the last stage when the reverse shock reached the center of the remnant, all of the ejecta material is heated and emits X-rays as described in the next section.

Figure 2.1 shows the 3-dimensional velocity profile of the ejecta in the situation surrounded by the uniform ISM whose density is $\sim$0.3 cm^{-3} by a 1-dimensional hydrodynamic simulation (cf., Truelove & McKee, 1999). This picture is a snapshot at the moment before the reverse shock reaches the center of the remnant. The ejecta before interacting with the reverse shock are free expanding. When they are shocked by the reverse shock, they get decelerated for the first time. After the deceleration, the ejecta velocity keeps constant toward the outer edge. Even when considering the Rayleigh-Taylor instability which we observe in fact and we can find in multi-dimensional simulations, this consistency will be also valid (cf., Blondin & Ellison, 2001).

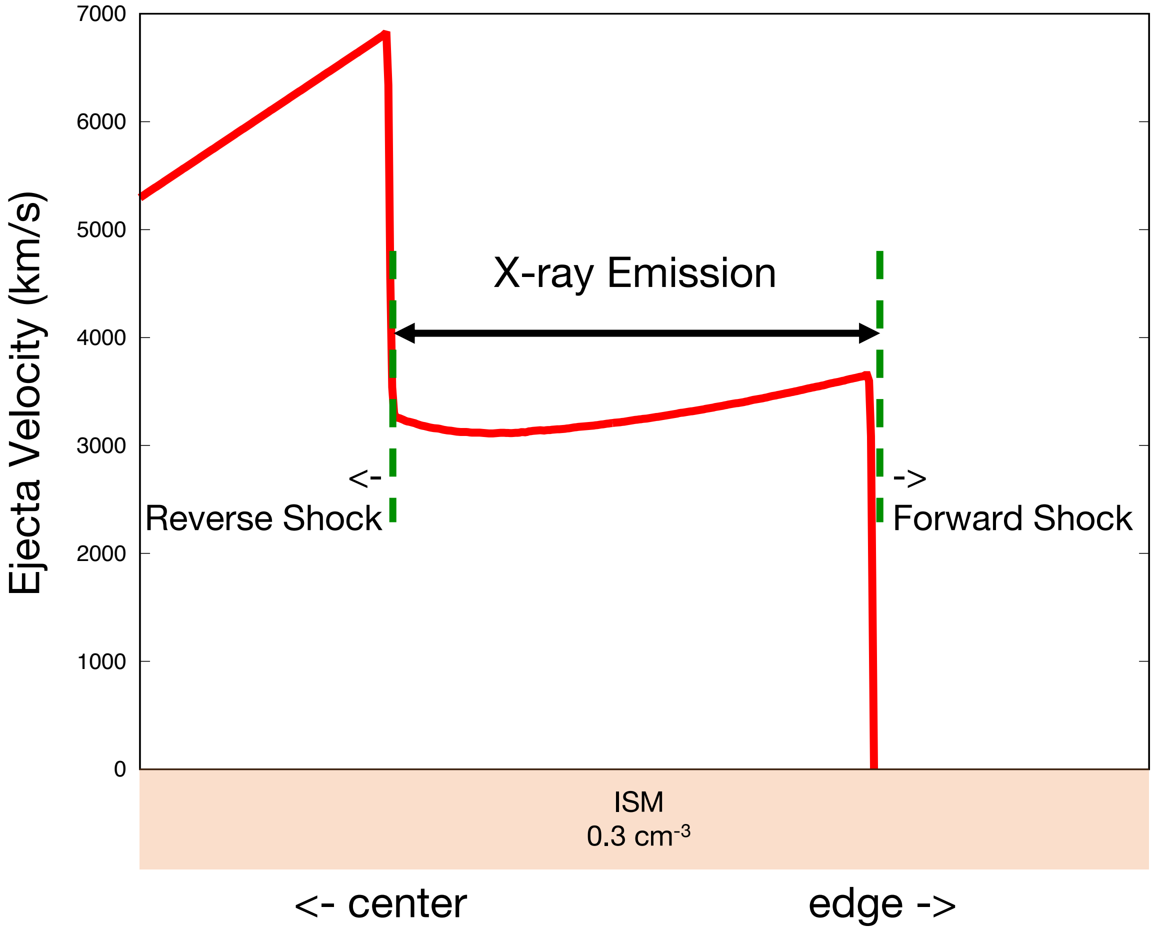

Figure 2.1: Simulational example of the radial profile of the 3-dimensional ejecta velocity in a uniform sparse ambient.

2.2.4 Interaction with dense CSM

The picture described above is the most basic one appearing in a situation without CSM. Here, we introduce another shock generated by the interaction with dense materials, called reflected shock (cf., Hester et al., 1994; Dwarkadas, 2005). The reflected shock also moves inward, so it could be confused with the reverse shock. However, it can be generated independently to the generation of the reverse shock.

Figure 2.2 also shows the 3-dimensional velocity profile of the ejecta but with dense clouds ∼100 cm^{-3}. In addition to the deceleration by the reverse shock, we can find the ejecta is re-decelerated by the reflected shock after that. Since their velocity is decelerated significantly, we expect this effect will be observed as clearly non-uniform kinematics of the ejecta. For example, Sato et al. (2018) found the ejecta moving inward in SNR Cassiopeia A and concluded this is the result of the interaction with the reflected shock generated by the molecular cloud associated with that SNR.

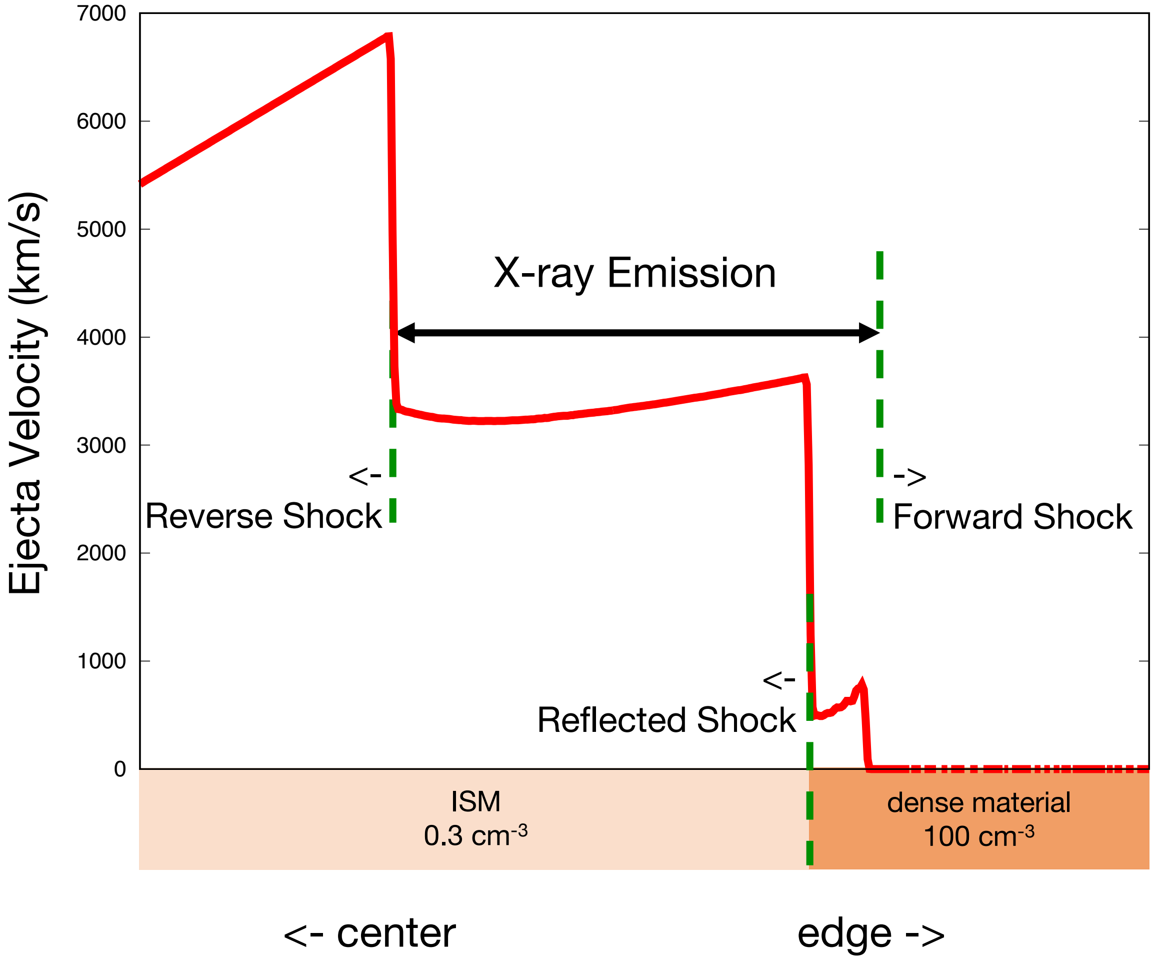

Figure 2.2: Same as Figure 2.1 but with a dense material in the outer region.

2.3 Supernova remnants in X-ray astrophysics

2.3.1 Heating by shocks

As described above, some types of shock heat materials in SNRs. The shock interaction in such sparse environment ~0.1–1 cm^{-3} is not the particle-particle interaction but the collision-less heating. The post-shock temperature kT by the Rankine-Hugoniot equation is calculated as:

$$kT = \frac{2(\gamma-1)}{(\gamma+1)^2} m_i v_\mathrm{s}^2 \ , \tag{2.8}$$

where m_i is the mass of particle i. In SNRs, the Mach number which is defined as the ratio of the shock velocity to the sound speed, is quite high ~100–1000. In this situation, the adiabatic index $\gamma = 5/3$, and:

$$kT_i = \frac{3}{16} m_i v_\mathrm{s}^2 = \frac{3}{16}(m_i c^2)\left(\frac{v_\mathrm{s}}{c}\right)^2 \ , \tag{2.9}$$

where c is the light speed. Considering the proton mass $m_\mathrm{p}c^2$ ~1 GeV and using the typical shock velocity v_s/c ~0.01 in young SNRs, the proton temperature kT_p is heated up to 10^7 K. It is the "keV" band, which is namely the X-ray band. In other words, we should care that we can observe only shock-heated elements in the X-ray band.

2.3.2 Line Emissions from non-equilibrium ejecta

Ejecta is heated by the reverse shock because this shock moves inward. The shock heating gives them a sudden jump in the temperature and density. It takes a finite time length to reach the equilibrium between the ionization and recombination for the ejecta plasma because they will keep their ionization balance by collisions. Before this Collisional Ionization Equilibrium (CIE), we have to regard that the ejecta in young SNRs are in the Non-Equilibrium Ionization (NEI) state.

The recombination process changes the ion valence z to $z-1$ by the radiative recombination and the dielectric recombination, where the total recombination rate is R_z. The ionization in contrast is the process of z to $z+1$ by the collisional ionization or the excitation-autoionization, where the total ionization rate is I_z. Then, the NEI state is described as:

$$\frac{1}{n_\mathrm{e}(t)}\frac{\mathrm{d}}{\mathrm{d}t}\vec{n}(Z,t) = \mathbf{A}(Z, kT(t))\ \vec{n}(Z,t) \tag{2.10}$$

where $\vec{n}$ is the $(Z+1)$-dimensional vector of the density of the ionization state z, n_z. The transition matrix **A** satisfies these relationships as:

$$\begin{aligned} z = 0 &: \frac{1}{n_{\mathrm{e}}}\frac{\mathrm{d}}{\mathrm{d}t}n_0 = -n_0 I_0 + n_1 R_1 \ , \\ z > 0 &: \frac{1}{n_{\mathrm{e}}}\frac{\mathrm{d}}{\mathrm{d}t}n_z = n_{z-1} I_{z-1} - n_z I_z - n_z R_z + n_{z+1} R_{z+1} \ , \\ z = Z &: \frac{1}{n_{\mathrm{e}}}\frac{\mathrm{d}}{\mathrm{d}t}n_Z = n_{Z-1} I_{Z-1} - n_Z R_Z \ , \end{aligned} \tag{2.11}$$

where we abbreviate the time variable t. The time evolution of NEI plasma is parameterized by:

$$\tau = \int \mathrm{d}t \ n_{\mathrm{e}}(t) \ . \tag{2.12}$$

When the ionization timescale τ reaches $\sim 10^{12}$ cm^{-3} sec^{-1}, NEI plasma transits to CIE plasma, where we can ignore the time dependence of $\vec{n}(Z,t)$ in Equation 2.10.

In contrast to CIE plasma, where we can determine the ionization state of elements only by one parameter (see Figure 7 in Kaastra et al., 2008, as an example of the function of temperature), we should describe it by both the electron temperature and the electron density (see Figure 3 in Yamaguchi et al., 2015, as an example). Although almost all elements as the ejecta in SNRs proceed to the He-like or H-like state, especially the ionization state of iron shows varieties from H-like to even Ar-like (e.g., Yamaguchi et al., 2014a). These heated elements emit characteristic X-rays, whose energy is unique to each ionization state. Table 2.1 and 2.2 show main observable characteristic emission lines in young SNRs (cf., Yamaguchi et al., 2014a; Foster, 2015).

2.3.3 Continuum emissions

The X-ray emission from SNRs is not only limited to the lines but also the continuum emissions. For example, the thermal Bremsstrahlung is emitted from decelerated free electrons colliding with ions. The emissivity ϵ is described as:

$$\epsilon \propto \frac{\alpha \sigma_{\mathrm{T}} c n_{\mathrm{e}} n_{\mathrm{i}} Z_{\mathrm{eff}}^2}{E} \left(\frac{m_{\mathrm{e}} c^2}{kT}\right)^{1/2} g \mathrm{e}^{-E/kT} \ , \tag{2.13}$$

where α is the fine structure constant; σ_{T} is the Thomson cross-section; Z_{eff} is the effective charge of the ion; g is the Gount factor; E is the emitted photon energy. The spectral shape of this emission is flat at the condition of $E \ll kT$ but drops exponentially after $E > kT$. We can measure the plasma temperature kT by observing this bending point at $E \sim kT$.

We mention another continuum radiation process, synchrotron radiation. This is not thermal radiation but emitted from relativistic electrons accelerated by the magnetic field at the shock front of SNRs. In the X-ray energy band, this emission is observed as a power-law spectrum with the spectral index is 2, E^{-2}.

Table 2.1: Main emission lines from SN ejecta in the X-ray band (0.5–8 keV)

Element	Valence	State	Line	Energy (keV)
Oxygen	6	He-like	O VII Kα (O Heα)	0.574
			O VII Kβ (O Heβ)	0.666
	7	H-like	O VIII Kα (O Lyα)	0.654
			O VIII Kβ (O Lyβ)	0.775
Neon	8	He-like	Ne IX Kα (Ne Heα)	0.922
			Ne IX Kβ (Ne Heβ)	1.074
	9	H-like	Ne X Kα (Ne Lyα)	1.022
			Ne X Kβ (Ne Lyβ)	1.211
Magnesium	10	He-like	Mg XI Kα (Mg Heα)	1.352
			Mg XI Kβ (Mg Heβ)	1.579
	11	H-like	Mg XII Kα (Mg Lyα)	1.473
			Mg XII Kβ (Mg Lyβ)	1.754
Silicon	12	He-like	Si XIII Kα (Si Heα)	1.865
			Si XIII Kβ (Si Heβ)	2.183
	13	H-like	Si XIV Kα (Si Lyα)	2.006
			Si XIV Kβ (Si Lyβ)	2.377
Sulfur	14	He-like	S XV Kα (S Heα)	2.461
			S XV Kβ (S Heβ)	2.884
	15	H-like	S XVI Kα (S Lyα)	2.623
			S XVI Kβ (S Lyβ)	3.106
Argon	16	He-like	Ar XVII Kα (Ar Heα)	3.140
			Ar XVII Kβ (Ar Heβ)	3.685
	17	H-like	Ar XVIII Kα (Ar Lyα)	3.323
			Ar XVIII Kβ (Ar Lyβ)	4.150
Calcium	18	He-like	Ca XIX Kα (Ca Heα)	3.902
			Ca XIX Kβ (Ca Heβ)	4.584
	19	H-like	Ca XX Kα (Ca Lyα)	4.107
			Ca XX Kβ (Ca Lyβ)	4.864

Table 2.1: `(continued)`

Element	Valence	State	Line	Energy (keV)
Titanium	20	He-like	Ti XXI Kα (Ti Heα)	4.750
Chromium	22	He-like	Cr XXIII Kα (Cr Heα)	5.682
Iron	16	Ne-like	Fe XVII L	0.727
				0.826
				1.023
	17	F-like	Fe XVIII L	0.704
				0.771
				0.873
	18	O-like	Fe XIX L	0.917
	19	N-like	Fe XX L	0.964
	20	C-like	Fe XXI L	1.009
	21	B-like	Fe XXII L	1.053
	22	Be-like	Fe XXIII L	1.056
			Fe XXIII Kα	6.589
	23	Li-like	Fe XXIV L	1.109
			Fe XXIV Kα	6.641
	24	He-like	Fe XXV Kα (Fe Heα)	6.700
			Fe XXV Kβ (Fe Heβ)	7.882
	25	H-like	Fe XXVI Kα (Fe Lyα)	6.973
Nickel	26	He-like	Ni XXVII Kα (Ni Heα)	7.806

Table 2.2: Weak emission lines from odd-Z ejecta

Element	Valence	Line	Energy (keV)
Nitrogen	5	N VI Kα (N Heα)	0.500
Aluminium	11	Al XII Kα (Al Heα)	1.598
Phosphorus	13	P XIV Kα (P Heα)	2.152
Chlorine	15	Cl XVI Kα (Cl Heα)	2.790
Manganese	23	Mn XXIV Kα (O Heα)	6.180

2.4 Measurement of the ejecta kinematics

2.4.1 Observation angle

We will study the ejecta kinematics. Since we can observe only from the earth, unfortunately, we need to observe the expansion of SNRs in the angular direction and the line-of-sight direction, independently. For the angular direction, we measure the motion using a differential image of snapshots within an interval between each observation. This method is effective for measuring the motion of structures with clear emission shape. For example, the forward shock at the outer edge of the remnant generally shows filamentary shape with synchrotron X-rays. Using X-ray imagers with good spatial resolution, *Chandra* ACIS for example (see §3.2), we can resolve its motion in the unit of 0.1 arcsec yr^{-1} (e.g., Katsuda et al., 2008). The shape of the ejecta structure, however, is diffused and hard to determine. Some studies have tried to measure the angular velocity for only bright knots, whose emission shape may not be changed in several years, but this method is not suitable for determining the general expansion structure.

On the other hand, we can more easily measure the line-of-sight velocity of the ejecta. Here we use the line information, which is shifted by the Doppler effect. This method is independent of the emission shape but requires a strong emission line in the observed spectrum and a precise understanding of plasma conditions. For young SNRs, the ejecta emission lines are outstanding and suitable for measuring the Doppler shift. We concentrate on this point, and study the whole kinematics of the ejecta in young SNRs throughout measuring the line-of-sight velocity structure.

2.4.2 Kinematics in the line-of-sight direction and line profiles

Line centroid

The exact value of the line centroid E_0 shown in Table 2.1 and 2.2 can be observed when the emission source is at static state. If it moves with the line-of-sight velocity $v_{\parallel}$, the energy E is shifted by the Doppler effect, as:

$$\frac{E_0 - E}{E_0} = \frac{v_{\parallel}}{c} \ . \tag{2.14}$$

When it moves far away from us, $v_{\parallel}$ is positive and E gets lower than E_0. We call this "red-shift". Otherwise, E gets higher in the "blue-shift" situation.

In young SNRs, the ejecta velocity is $\sim 0.01c$. For Fe XXV Kα line, for example, the line shift $|E - E_0|$ is $\sim$67 eV. If it is red-shifted, the observed energy E gets close to the static energy of Fe XXIV Kα and Fe XXIII Kα. Like so, it is a little dangerous to determine the ionization state only by the line centroid.

Line width

At first, the line width σ_{D}, in the unit of eV, of the Gaussian profile of each emission is broadened by the thermal Doppler broadening, as:

$$\left(\frac{\sigma_{\mathrm{D}}}{E_0}\right)^2 = \left(\frac{\sigma_{\mathrm{t}}}{E_0}\right)^2 + \frac{kT_i}{m_i c^2} \ , \tag{2.15}$$

where σ_{t} is the broadening due to its turbulent velocity and T_i and m_i is the temperature and mass of the emission source i. For high kinematic velocity ejecta in young SNRs, the turbulent velocity can be ignored and:

$$\frac{\sigma_{\mathrm{D}}}{E_0} \simeq \sqrt{\frac{kT_i}{m_i c^2}} = \sqrt{\frac{3}{16}\frac{v_{\mathrm{s}}}{c}} \ . \tag{2.16}$$

With the energy resolution of existing detectors in the X-ray observatories so far (see Chapter 3), we should consider another broadening effect. When both red-shifted ($v_{\mathrm{r}} > 0$) and blue-shifted ($v_{\mathrm{b}} < 0$) sources exist in the same line-of-sight direction, only the summed up single Gaussian can be observed. The difference between the original two Gaussian centroids is $(v_{\mathrm{r}} - v_{\mathrm{b}})/c$, and the observed line width of single Gaussian is also broadened to its comparative value.

This broadening effect is dominated in young SNRs and can be used as a test of the expansion structure of the ejecta. When we observe the center region of the spherical expanding remnant, the velocity difference ($v_{\mathrm{r}} - v_{\mathrm{b}}$) is largest. The line width is also expected to be widest there. When we observe outer regions, the velocity difference gets smaller and the line width gets narrower. Therefore, the line width is monotonously decreased from the center to the edge for the uniform and isotropic expansion structure. In other words, we can suspect such simple structure if the line width behaves differently.

Chapter 3

X-ray Observatories

Due to the absorption by the atmosphere around the earth, we cannot observe cosmic X-rays by the ground telescopes. Therefore, we need to observe them in the space. Except for temporary observation projects using rockets or balloons, we adopt large satellites for long-term X-ray observatories. This chapter introduces two famous X-ray observatories and main detectors on board them, which we use in this thesis.

3.1 *XMM-Newton* observatory

3.1.1 Overview

The *XMM-Newton* space observatory (Jansen et al., 2001) is one of the most used observatories in X-ray astrophysics over these twenty years. This spacecraft was launched on December 10, 1999, by the European Space Agency (ESA) and is still active on the front line even at the end of 2021. The strong point of this spacecraft is ten times larger effective area than other famous one *Chandra* described in the following section. Such large effective area helps observing dark targets especially in the Fe-K emission band around 6 keV. The total size of this spacecraft is ∼10 m and the weight is ∼4 tones.

3.1.2 X-ray Telescopes and Mirrors

The observatory name "*XMM*" is the abbreviation of "X-ray Multi-Mirror Mission"[1]. This spacecraft contains three X-ray telescopes (Figure 3.1), including a 58-shell Wolter-1 X-ray mirror for each (Aschenbach et al., 2000). The X-ray energy is too high to bend

---

[1] Which the abbreviation of the second "M" refers to "mirror" or "mission" differs in references. In the first place, *XMM* was "X-ray Multi-Mirror observatory" (Gondoin et al., 1994). The second "M" is clearly "Mirror" in this context. However, even the main authors of the most cited overview paper Jansen et al. (2001) used "X-ray Multi-mirror Mission" in another paper (Lumb et al., 2012). Almost all people use "X-ray Multi-Mirror Mission" in fact, and this thesis also follows it.

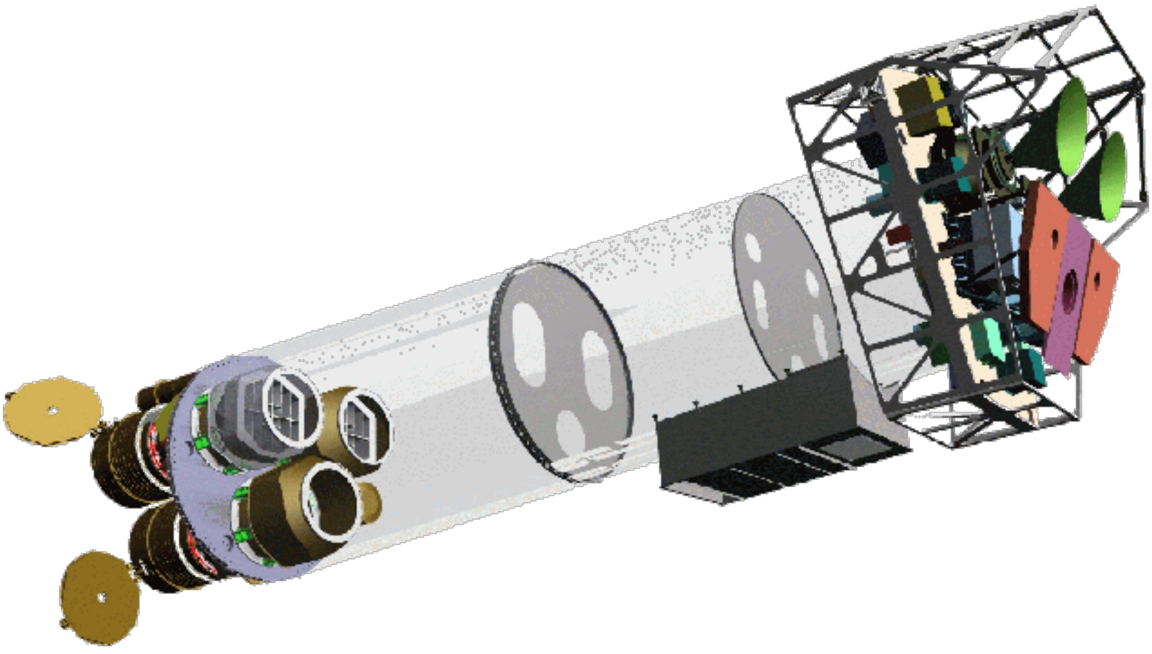

Figure 3.1: Overview of *XMM-Newton* observatory (XMM-Newton Users Handbook, Issue 2.19, 2021).

photon tracks by lenses, therefore the Wolter-1 X-ray mirror collects X-ray photons by reflecting it with the small critical angle. While this system needs long focal length, 7.5 m on *XMM-Newton* for example, it achieves large geometrical effective area ~1,500 cm^2 for each telescope on board this spacecraft. This mirror system also brings the good angular resolution, which is ~5 arcsec (FWHM) over all the energy band between 0.15 keV to 12 keV. This value is still fine comparing with other X-ray telescopes even in 2020s like ones for *Suzaku* (Mitsuda et al., 2007) and *NuSTAR* (Harrison et al., 2013), and effective enough to resolve extended X-ray sources as SNRs. Note that the Attitude & Orbit Control Subsystem (AOCS) of *XMM* determines its own attitude with the accuracy of <1 arcsec in every 2 seconds during observations by two star trackers and the information on the position of the Sun. This upper-limit of the pointing accuracy is enough smaller than its angular resolution.

3.1.3 CCD Detectors

The most widely used detector for cosmic X-ray observations is the Si-semiconductor type. The principle for detecting X-rays by such detectors is the following. When a cosmic X-ray photon incidents to the effective layer in a silicon detector, the electron-hole pairs are generated. The number of pairs N is calculated as $N = E/3.65$, where E is the incident photon energy in the unit of eV. The fluctuation of N is calculated as $\Delta N = \sqrt{F_{\mathrm{Si}} N}$, where $F_{\mathrm{Si}} = 0.12$ is the fano-factor of Si. Here, the limit of the energy resolution of CCD detector ΔE_0 is $\sim 3.65 \times \Delta N = 120$ eV at 5.9 keV and 50 eV at 1.0 keV in FWHM. This energy resolution is good enough for resolving characteristic X-ray lines above Si Heα, but not suitable for lines in the lower energy band. For Charge-Coupled Device (CCD), which is the main type of the existing detectors, the electrons composing each of the electron-hole pair are captured by the electrodes in each pixel of CCDs. These electrons are transferred to the next pixel sequentially by applying higher positive voltage to the next one, and read-out at the edge of the CCD chip finally. Here, we should define the read-out direction or transfer direction in a CCD chip.

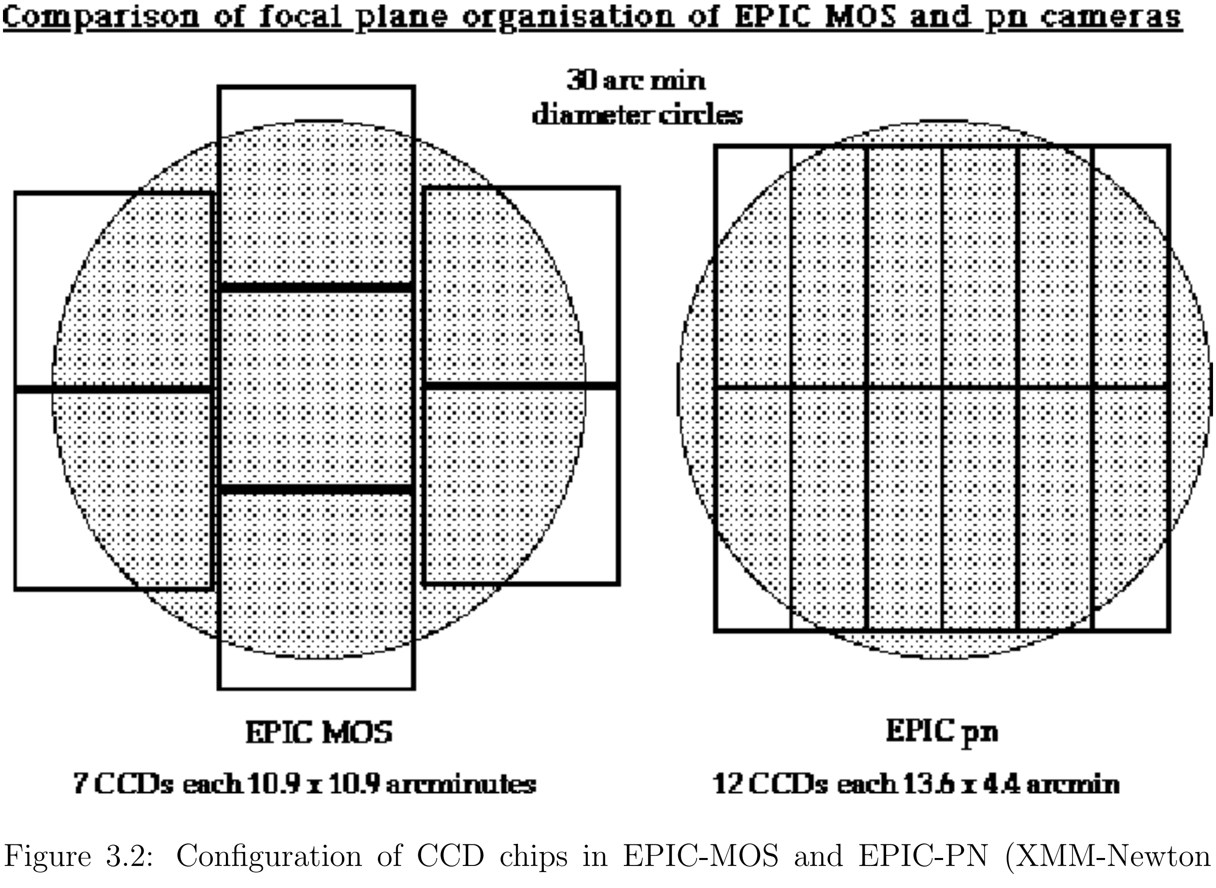

Figure 3.2: Configuration of CCD chips in EPIC-MOS and EPIC-PN (XMM-Newton Users Handbook, Issue 2.19, 2021).

XMM-Newton adopts CCD type detectors named European Photon Imaging Camera (EPIC). In all the three EPICs, two of them are Metal-Oxide Silicon (MOS) type CCDs (Short et al., 1998; Turner et al., 2001). Each MOS detector, named MOS1 and MOS2, contains 7 CCDs, whose size is ∼2.5 cm square. The central one is configured at the focal point of the telescope and the other 6 CCDs surround it following the focal plane (Figure 3.2). The size of Field-Of-View (FOV) of the central CCD is ∼10 arcmin square. All CCDs are front-illuminated type and it helps low background noises of MOS detectors. The energy resolution of MOS is ∼70 eV @ 1 keV and ∼150 eV at 6.4 keV (FWHM). The read-out direction of all CCDs in each detector is aligned, but the systematic error due to this direction can be canceled by summing observed data from both MOS detectors because MOS1 and MOS2 are configured orthogonally.

Another EPIC is PN type CCDs (Gatti & Rehak, 1984; Strüder et al., 1987, 2001). Each PN is the back-illuminated type and drifts electrons generated in the depletion layer by incident photons towards detecting pixels like gas chamber detectors. The read-out time of PN, ∼0.03 msec, is shorter than MOS by two orders of magnitude because each detector column is read-out parallelly for fast timing observations. The energy resolution, on the other hand, is worse than MOS, which is ∼80 eV @ 1 keV (FWHM) and this difference gets larger in the lower energy band. The size of PN CCD is 3×1 cm^2 with single silicon wafer for homogeneous quality, and totally 12 PN CCDs are equipped (Figure 3.2). The configuration of PN CCDs are at an degree of 45° to MOS. Therefore, the total FOV of EPICs are covered without gaps. Note that we only use the data observed by MOS detectors because EPIC-PN has worse energy resolution and more violent detector noises (Katayama et al., 2004; Nevalainen et al., 2005; Kuntz & Snowden, 2008).

3.1.4 Grating spectrometers

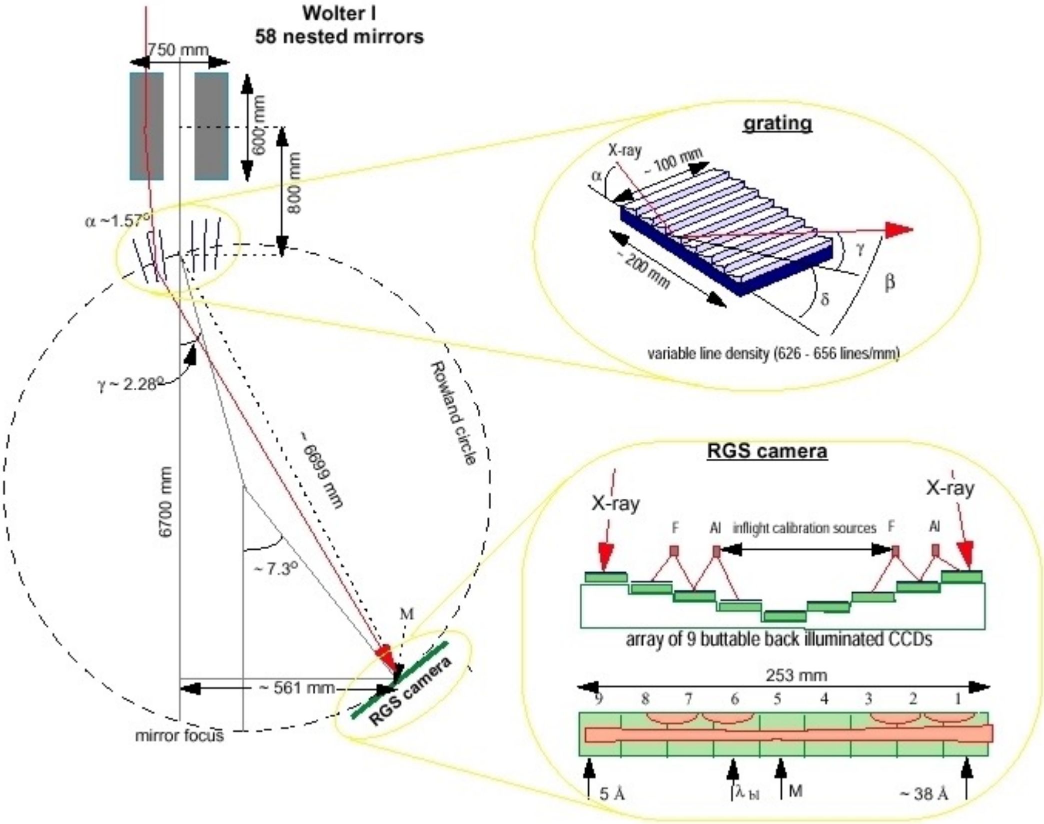

Figure 3.3: Overview of grating spectrometer system on board *XMM* (Brinkman et al., 1998).

Accompanying two MOS detectors, *XMM-Newton* also loads two grating spectrometer systems (Figure 3.3), Reflection Grating Spectrometer (RGS) (den Herder et al., 2001). At the front side of each MOS detector, the Reflection Grating Array (RGA) is directly attached to the mirror assembly. Although the half of photons entering RGA penetrates to the MOS plane, the other half is reflected and led to another CCD detecting system named RGS Focal plane Camera unit (RFC). It means, unlike the individual operation of grating spectrometers on board *Chandra*, *XMM-Newton* observes X-rays by RGS simultaneously with MOS.

The reflected angle β by RGA is dependent on the incident wave length λ and angle of photons following the dispersion direction α:

$$m\frac{\lambda}{d} = \cos\beta - \cos\alpha \ . \tag{3.1}$$

The groove density of RGA, $1/d$ is 645.6 mm^{-1}. Because β must be larger than α, which is 1.5762° for a source at the focal point, the order parameter m should be a negative integer.

The strong point of such a grating spectrometer is its great energy resolution in the lower energy band. Concerning RGS, it is ∼3.5 eV at 1 keV (FWHM) for the 1st order events and ∼1.5 eV for the 2nd order. This value is superior to that of CCD detectors, and it can resolve not only L-shell emission lines from iron but also the forbidden line and resonance line from O^{6+} (cf., Uchida et al., 2019).

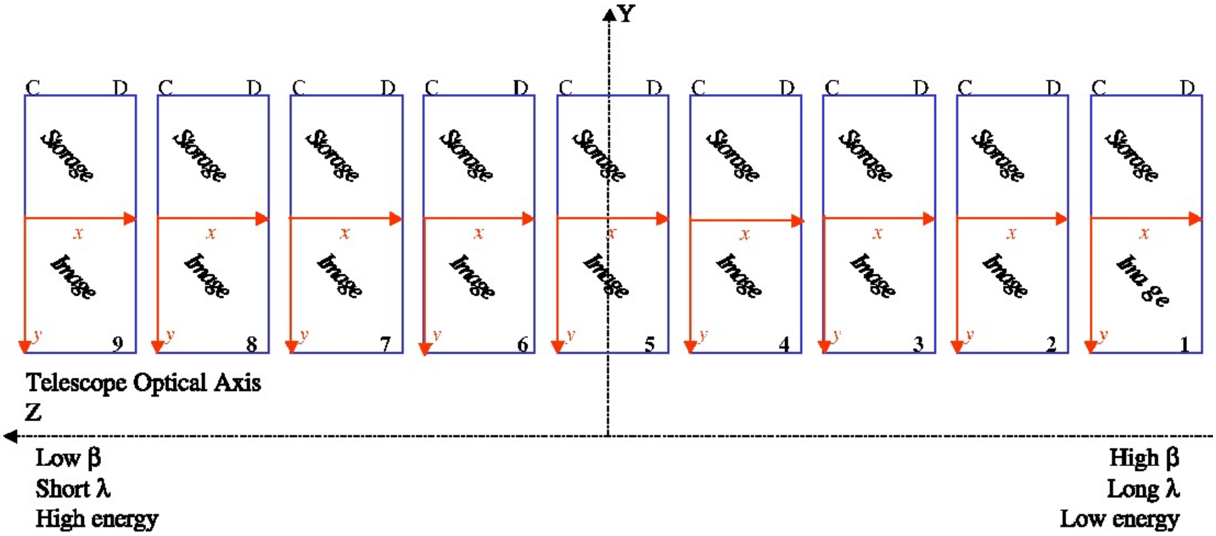

Figure 3.4: CCD chips in RFC configured following the dispersion angle of RGS (XMM-Newton Users Handbook, Issue 2.19, 2021).

RFC consists of 9 back-illuminated CCDs following the dispersion curvature of RGA, and we can estimate the angle β from the detected position in the dispersion direction (Figure 3.4). The effective energy band is limited to 0.35–2.5 keV due to the geometrical size of RFC. Such a grating spectrometer does not have the spatial resolution in the dispersion direction in principle. Because β is dependent on not only λ but also α, RGS observation is suitable for point-like or slightly extended sources, where the variance of α is regarded to be small. Otherwise, we should consider the emission shape into the process of converting the detected position to the incident wave length λ, as:

$$\Delta\lambda = \frac{0.138}{m}\theta \ , \tag{3.2}$$

in the unit of angstrom, where θ is the extent of the emission source in the unit of arcmin. Its coefficient of 0.138 comes from the geometry of the RGS system (XMM-Newton Users Handbook, Issue 2.19, 2021). On the other hand, RGS has the spatial resolution only in the cross dispersion direction of RFC, which is independent of λ. The one-dimensional FOV is ∼5 arcmin and we can resolve it with the angular resolution of ∼5 arcsec (FWHM).

3.2 *Chandra* observatory

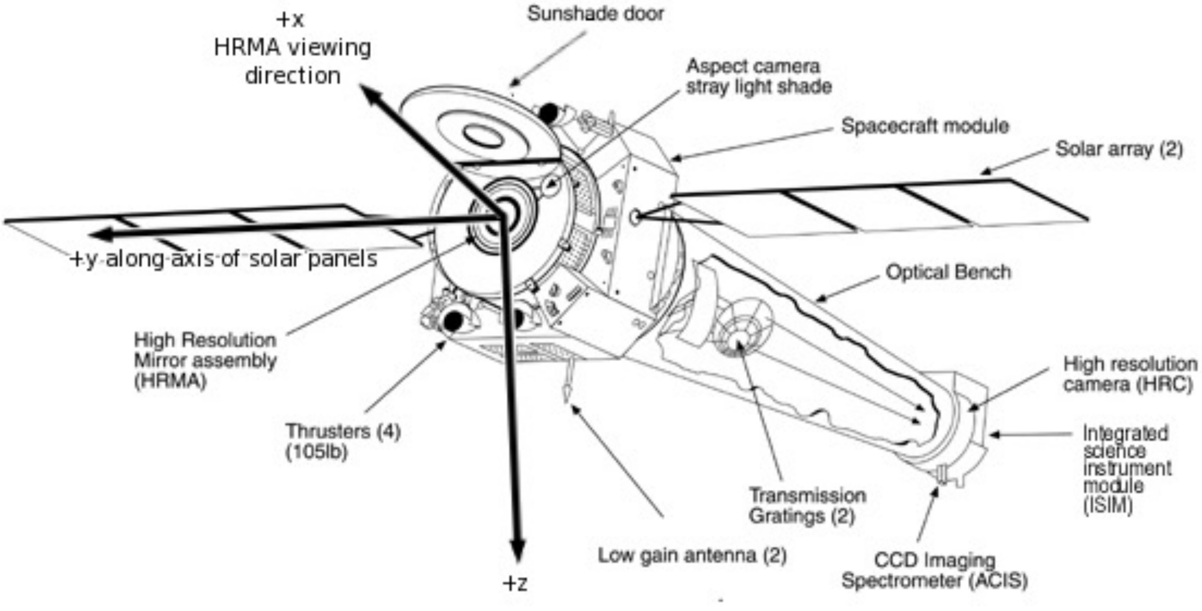

Figure 3.5: Overview of *Chandra* observatory (Chandra Proposers' Observatory Guide, Version 24.0, 2020).

The *Chandra* space observatory (Weisskopf et al., 2000) is the same age as *XMM-Newton*, launched on July 23, 1999, by National Aeronautics and Space Administration (NASA). Instead of its lower effective area compared with *XMM-Newton*, its High Resolution Mirror Assembly (HRMA) achieves the excellent spatial resolution ∼0.5 arcsec (FWHM). We do not have, and will not have so far, other comparable X-ray imagers in the space. Therefore, it has been used for spatially resolved analysis of extended sources like SNRs or gaining signal-to-noise ratio[2] for faint point-like sources.

---

[2] This study never abbreviates "Signal-to-Noise Ratio" as "SNR".

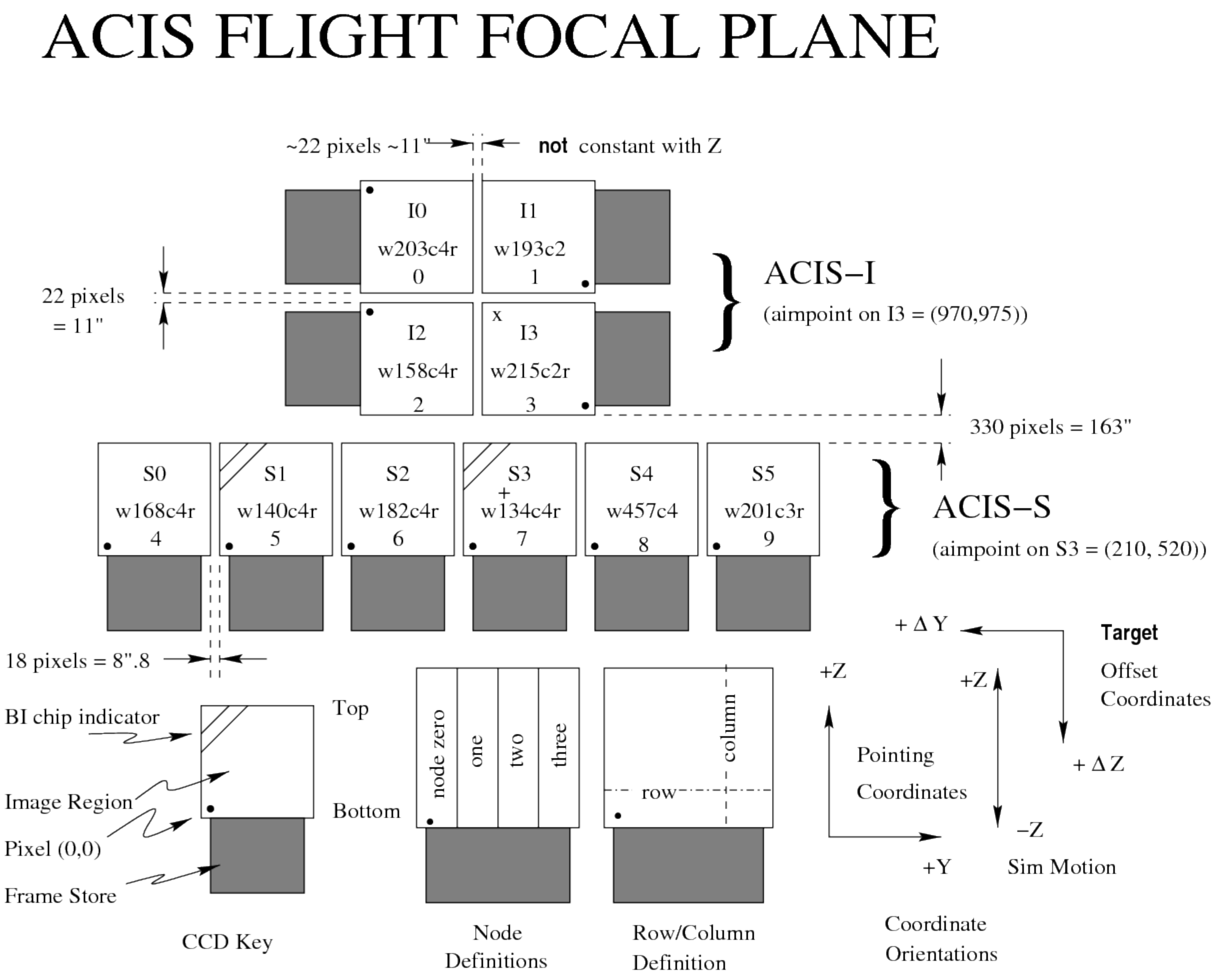

Figure 3.6: Configuration of ACIS detectors on board *Chandra* (Chandra Proposers' Observatory Guide, Version 24.0, 2020).

In this thesis, we only use the CCD detectors on board *Chandra* for our analysis, named as Advanced CCD Imaging Spectrometer (ACIS) (cf., Nousek et al., 1987). ACIS includes two different types of detectors, ACIS-S and ACIS-I (Figure 3.6). ACIS-S consists of six CCDs configured linearly. The "S" means "Spectroscopy" and ACIS-S is also used with grating analysis. The other four CCDs are equiped with ACIS-I, where "I" means "wide field Imaging". They are arranged in 2×2, which enable us to observe four times larger sources than that by ACIS-S. Note that the performance of each CCD in both ACIS-S and ACIS-I are same. Although their performance is also similar to that in EPIC-MOS, we avoid adopting the ACIS detectors for spectroscopy due to the sacrificial charge problem described in Chapter A. Thanks to its great spatial resolution, we only use them for creating exposure-corrected event images, which represent the photon flux of emission sources.

Chapter 4

Spatially resolved spectroscopy of Kepler's supernova remnant

At first, we measure the ejecta velocity structure in an SNR with dense CSM. As an optimal target, Kepler's SNR is the largest and brightest one among young type Ia SNRs accompanying CSM (Vink, 2017, for a review). Note that the time series of our Kepler analysis is inverse between the order in this thesis and the factual order. The first half (Chapter 4) is a reconfirmation analysis of Kasuga et al. (2018) for avoiding using *Chandra* ACIS-S detectors for spectral analysis, even though the problem we found is only confirmed in ACIS-I detectors (Chapter A). We refer the results in Kasuga et al. (2021), which is described in the following chapter (Chapter 5), in this chapter. These studies are independent and Kasuga et al. (2021) is really the "previous" work for the study in this chapter.

4.1 Observation history of Kepler's SNR

SNR G4.5+6.8 (or 3C 358), which is the remnant of SN 1604, is one of the brightest and youngest SNRs we have detected. Originating from the historical records that Johannes Kepler (1571–1630) found its supernova on October 9, 1604 (Kepler, 1606)[1], this remnant is called "Kepler's SNR" conventionally. This supernova is the latest one observed in our galaxy. Note that we definitely had missed observing the origin of SNRs Cassiopeia A and G1.9+0.3, which are younger remnant than Kepler's SNR.

Kepler's SNR is a major candidate of the SD scenario because of the existence of the nitrogen-rich dense CSM $\sim$100 cm^{-3} (Blair et al., 1991; Gerardy & Fesen, 2001). Minkowski (1959) found strong [N II] emission in the optical band. Katsuda et al. (2015) found, and Nagayoshi et al. (2021) reconfirmed by a more precise abundance model, strong

---

[1] To be exact, Johannes Kepler observed this supernova on October 17, and Lodovico delle Colombe was accurately the first observer on the supernova day (delle Colombe, 1606).

N Lyα emission also in the X-ray band. This nitrogen is thought to be produced by the CNO cycle in a massive star as a donor of the accretion (Bandiera, 1987). The neutral hydrogen density estimated by Hα line from the non-radiative shock is $\sim$10 cm^{-3} (Blair et al., 1991). This high density is also not explainable by the expected ISM where is about $594d_5$ pc above the galactic plane, where d_5 is the distance in the unit of 5 kpc. The dust observation by the infrared band shows the dust is associated with not ejecta but CSM, and this is consistent with the characteristics of type Ia SNe (Williams et al., 2012). For explaining the bar-like CSM structure around the center of the remnant, Burkey et al. (2013) proposed a torus-like CSM generated by the stellar wind in the SD scenario (Hachisu et al., 2008).

The rich amount of IGEs also supports the SD origin of this SNR (Kinugasa & Tsunemi, 1999; Cassam-Chenaï et al., 2004; Reynolds et al., 2007; Katsuda et al., 2015). Park et al. (2013) observed strong manganese emission suggesting super-solar metallicity of the progenitor star. Patnaude et al. (2012) and Katsuda et al. (2015) concluded the original SN is an over-luminous event like SN1991T for explaining the observing iron emissions. Sato et al. (2020) found an iron ejecting knot at the south-west rim and it is thought to be produced by the incomplete silicon burning during the explosion.

Despite these strong supporters for the SD scenario, some skeptical points still exist in fact. Kerzendorf et al. (2014) searched the donor star in its progenitor system of Kepler's SNR, but they were not able to find any candidates. In addition, the bulk velocity estimated to be $\sim$250 km sec^{-1} for the progenitor system (cf., Bandiera & van den Bergh, 1991) is too high to assure the necessary situation for explosion. Such contradictions, and the characteristic structure called "ears" at the north-west and south-east edge of the remnant, could be solved by another supernova scenario called core degenerate scenario (Ilkov & Soker, 2012; Tsebrenko & Soker, 2013). The core degenerate scenario is an intermediate style of the SD and DD scenarios because it is the merger between a WD and the core of an AGB star. Note that this scenario has not been widely accepted so far.

Sato & Hughes (2017a) and Millard et al. (2020) measured the line-of-sight kinematics at some bright knots using silicon and iron K-lines, respectively. Kasuga et al. (2018) also did it generally over the entire remnant, but it only focused on the Fe-K line. This study will systematically measure the Doppler velocity of the ejecta and CSM in the entire remnant, and discuss the relationship between them.

4.2 Observations

4.2.1 Source observations

Table 4.1: Observation list of Kepler's SNR and its background by *XMM-Newton*.

Observation ID	Start Date	Duration (sec)	GTI-1 (sec)	GTI-2 (sec)	Note
0084100101	2001.03.10	33508	-	-	not used in this study
0853790101	2020.03.11	38700	-	-	not used in this study
0842550101	2020.03.19	140500	109995	111321	
0801931901	2019.04.01	84000	80230	80250	as a background spectrum

GTI-n means the good time interval in MOSn for each observation.

XMM-Newton has observed Kepler's SNR only three times (Table 4.1). Observation ID `0084100101` is a much older one and we should care about the time variation of SNR evolution or detector condition if including this data for this analysis. The remaining ones are very recent observations but the duration time of `0853790101` is much shorter than `0842550101`. Avoiding uncertainties generated by mixing multi observational data, we use only the data of `0842550101` for this study. The diameter of this remnant is ~4 arcmin and fit into the central CCD chip of both MOS detectors.

We download the Observation Data Files (ODFs) and Current Calibration Files (CCFs) release number 384 from ESA. Because ODFs are raw files from the spacecraft, we should reprocess them with CCFs for accurate analysis by following commands in the software package for the *XMM-Newton*, `Scientific Analysis System 19.1.0 (SAS)` (Gabriel et al., 2004). `cifbuild` and `odfingest` extract necessary information from CCFs and housekeeping data of the satellite. After this preparation, `emchain` and `mos-filter`[2] reprocesses the ODFs with proper calibrations. Throughout these reprocessing, bad photon events mainly contaminated with solar flares are excluded from the row event list. After such filtering, the remaining effective observation period is called Good Time Interval (GTI). For `0842550101`, the total GTI of both MOS detectors is ~220 ksec.

4.2.2 Background observations

Even though Kepler's SNR is one of the brightest SNRs observed from the earth, we cannot ignore the background components especially in the higher energy band near the Fe-K lines. Such background includes the following components. In the FOV, X-ray sources

---

[2] The latest version `sas 19.1.0` fails generating `corn-image.fits`, which is necessary for creating spectral files in next process. In this study, only `mos-filter` command is executed in the package of `sas 16.0.0`.

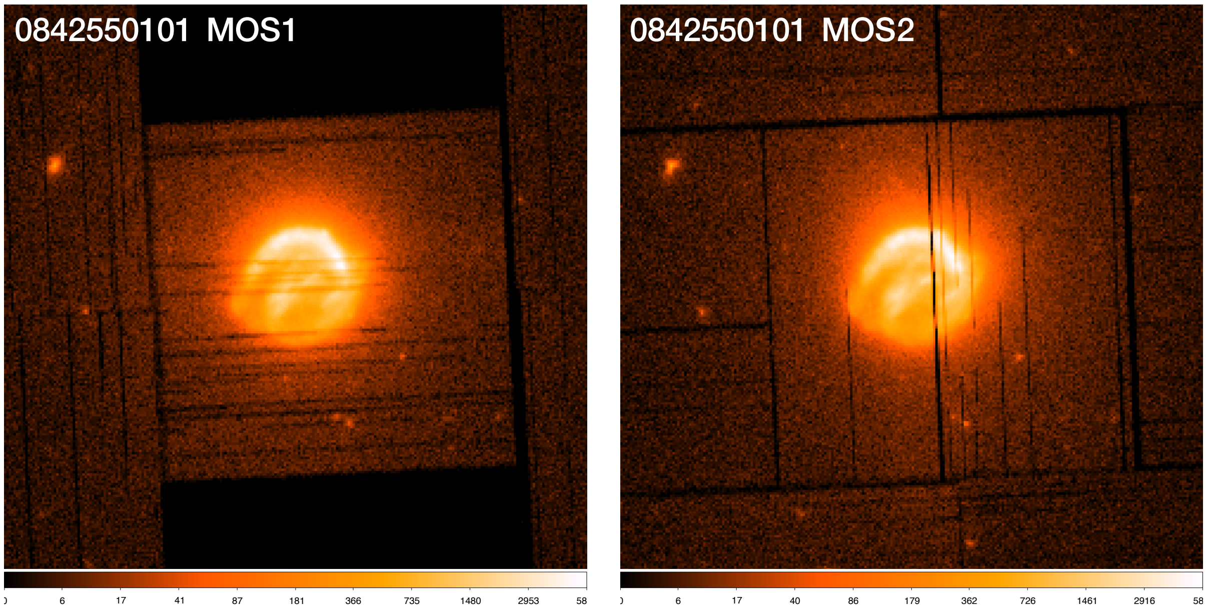

Figure 4.1: Event count maps of Kepler's SNR by both of the *XMM-Newton* MOS detectors on a logarithmic scale.

that are not necessary for the study could be contaminated. Other than easily resolvable sources, Cosmic X-ray Background (CXB) is distributed over the sky. Nevertheless CXB is revealed as distant point-like sources like black-holes or Active Galactic Nuclei (AGN) (cf., Comastri et al., 1995; Marconi et al., 2004), *XMM-Newton* cannot resolve them spatially. Another background source is the detector backgrounds like Non X-ray Background (NXB). NXB consists of solar soft protons, mainly in the solar flare, and the fluorescence lines from instrumental elements like aluminium and silicon radiated by induced cosmic rays (Carter & Read, 2007). Note that the period directly exposed by the solar flare can be excluded by the `sas` reprocessing process.

The simplest way to estimate these background is executing `mos_back` command in `sas`, which uses the information on the outer pixels than the source-radiated region in the same MOS detector (see Figure 3.2). Although the observation date is completely the same and the time dependence of CXB and NXB is resolved, the NXB could be over- or under-estimated because the pixel dependence of NXB still exists. Moreover, the outer pixels during the observation of such bright source like Kepler could contaminate the source photons. It makes the background level over-estimated. We adopt another way by using blank-sky or point-source observations, whose focal point and observation period is near that of `0842550101`. Using the data at the same detector pixels as Kepler was observed, we can solve almost all problems remaining in the background estimation by `mos_back`. The referenced background observation is `0801931901`, which observed Jupiter, by excluding point-like sources (Table 4.1).

4.3 Extracting spectra

We generate the spectra and the detector response files in both MOS detectors in each observation by `mos_spectra` in `SAS`. The spectral files include the information on each photon event, which helps us to make a histogram of incident energy and counts. The detector response files consist of two types. One is Auxiliary Response Files (ARFs), which includes the information on the effective size of the detector area and the quantum efficiency of detecting for each energy. The other is Response Matrix Files (RMFs), which consider the energy resolution of the detector. For combining them from each observation, we adopt `mathpha`, `addarf`, and `addrmf` in the software package of `High Energy Astrophysics Software (HEASoft) 6.28` (Blackburn, 1995), respectively. Figure 4.2 is the background-subtracted spectrum from the entire remnant as a product of such processes. We can see outstanding emission lines from the ejecta including silicon, sulfur, argon, calcium, and iron. We also plot the background spectrum in the same figure, whose strength is ∼1 % in almost all the energy band. The background level reaches the source level in the higher edge because the NXB increases there.

To study the spatial characteristics of this extended object in detail, we need to divide it into some fine structures. Recent studies of SNRs often adopt adaptive binning algorithms like Voronoi binning (Cappellari & Copin, 2003; Diehl & Statler, 2006) or the contour binning method (Sanders, 2006). Such methods aim to equal the signal-to-noise ratio or the surface brightness at each divided region. Although such methods are more effective to dark extended sources, Kepler's SNR has enough photon statistics everywhere for spectral fitting. We think it is desirable for bright sources to divide the source by a non-biased method, which means dividing simply by orthogonal grids. Such simple methods can reduce the uncertainty of the division process and emphasize spatial variability. We divide Kepler's SNR into grids whose size is 15 arcsec square, making 16×14 sky pixels to consider the angular resolution of the telescopes (∼5 arcsec in FWHM, see §3.1.2). Figures 4.3 show all of the sky pixels on the flux image in each energy band observed by *Chandra*. Note that these flux images are generated by correcting the exposure time at each detector position by `flux_obs` in the software package of `Chandra Interactive Analysis of Observations (CIAO)` (Fruscione et al., 2006).

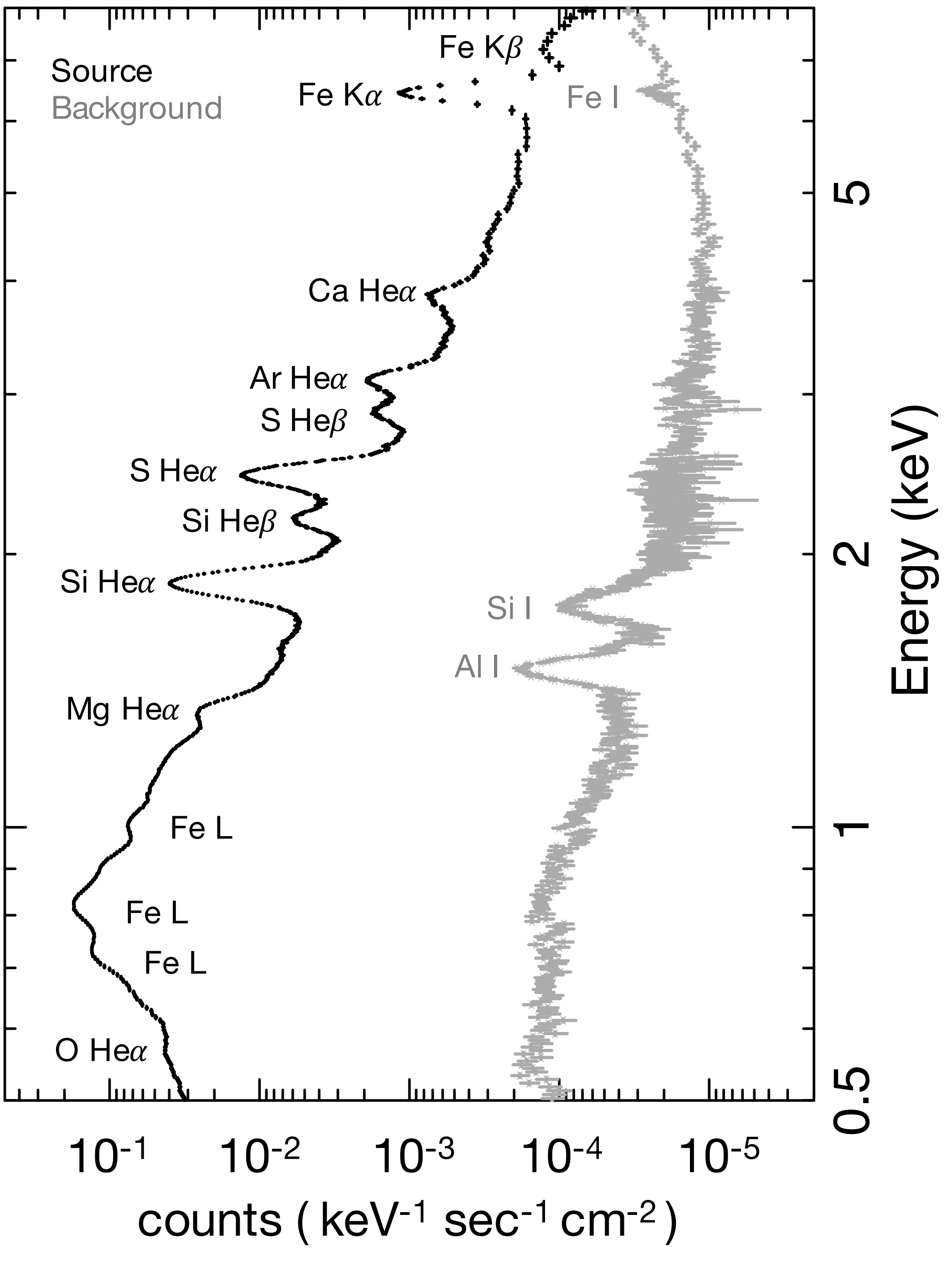

Figure 4.2: X-ray spectrum from the whole of Kepler's SNR (black) and its background (grey). Some outstanding emission lines are identified.

Full band (0.5–8.0 keV)

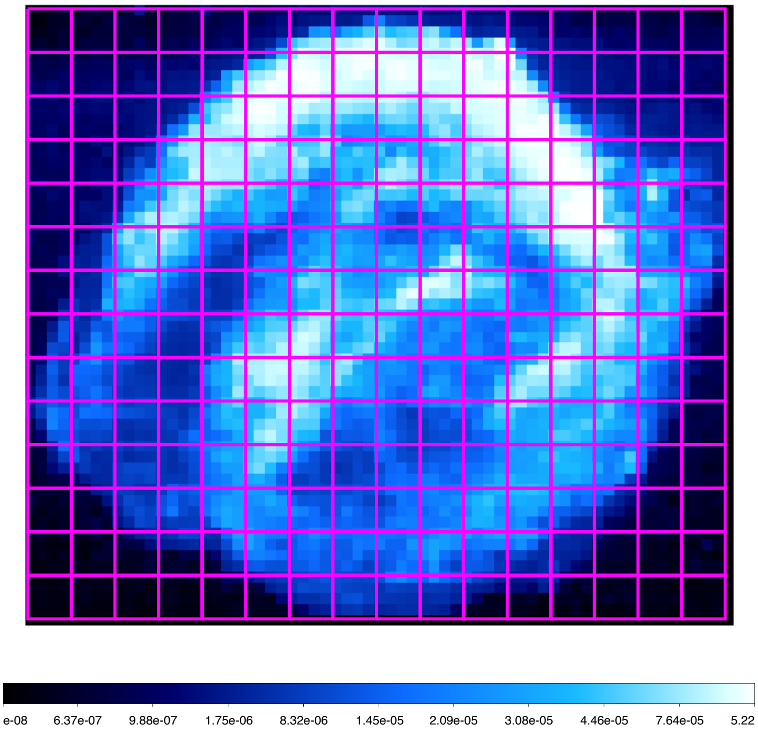

Continuum (4.1–6.1 keV)

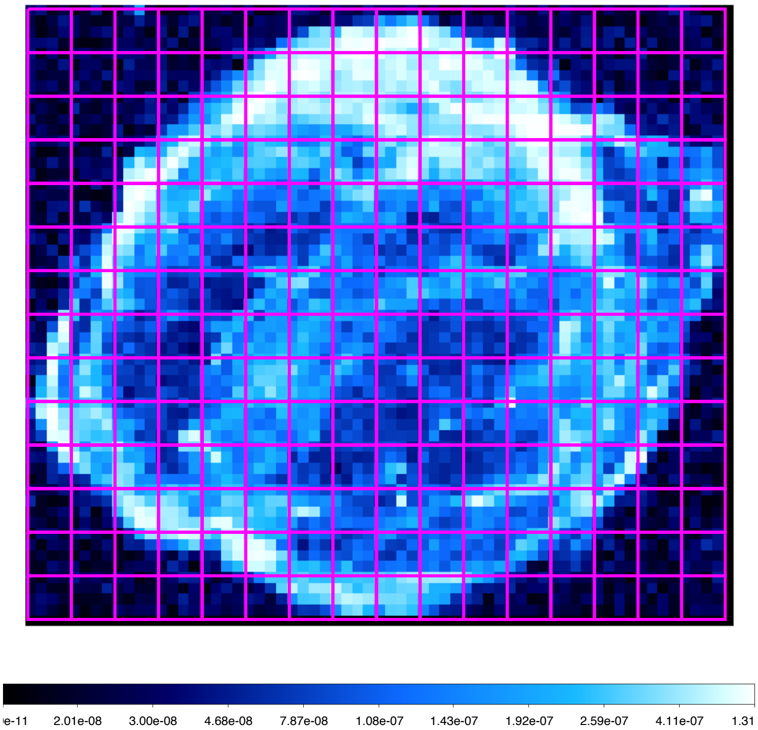

Figure 4.3: Flux images in each energy band of Kepler's SNR by *Chandra* on a histogram-equalized scale in the unit of counts $\sec^{-1}$ cm^{-2}. The grid on the images represents each sky pixel we extract. The coordinate of each sky pixel is represented as (x, y).

O VII (0.5–0.6 keV)

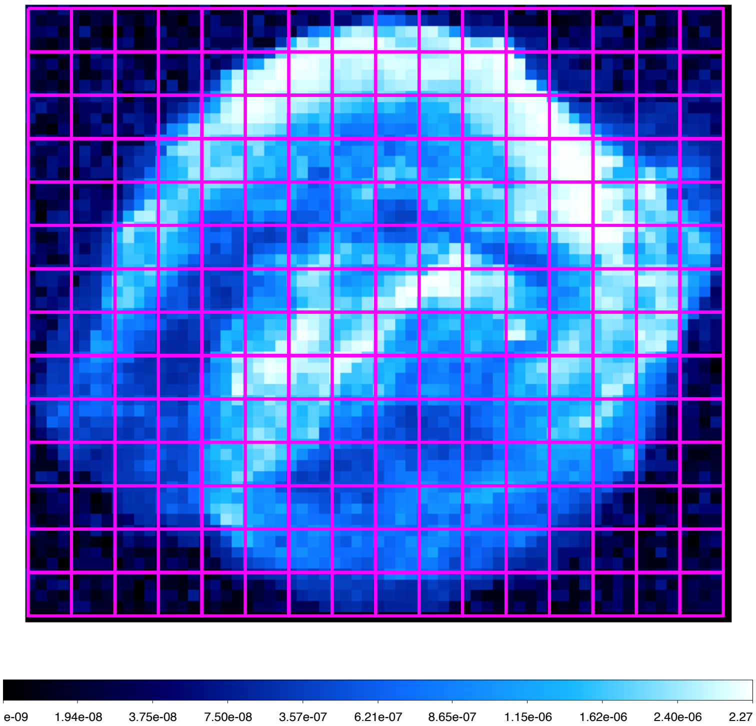

Fe-L (0.8–1.25 keV)

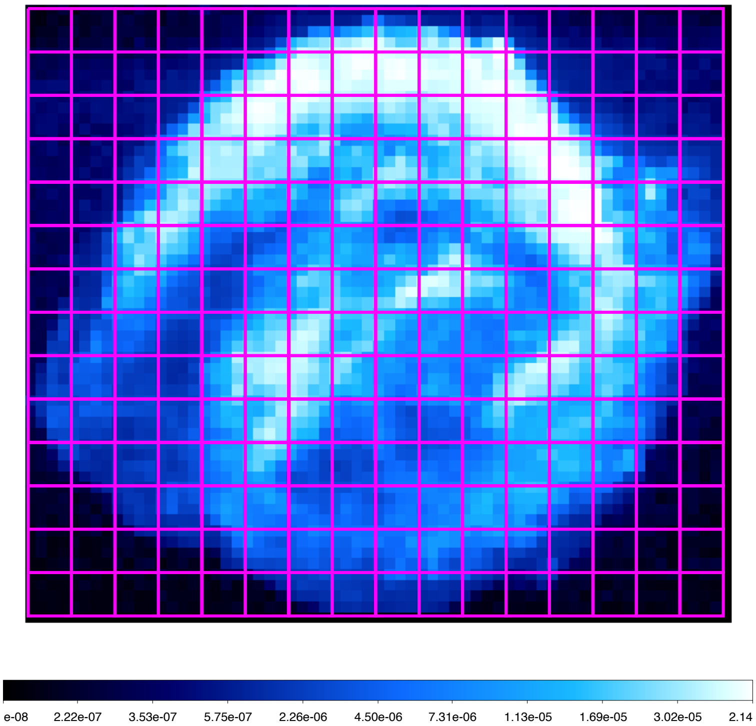

Figure 4.3: `(continued)`

Mg XI (1.27–1.39 keV)

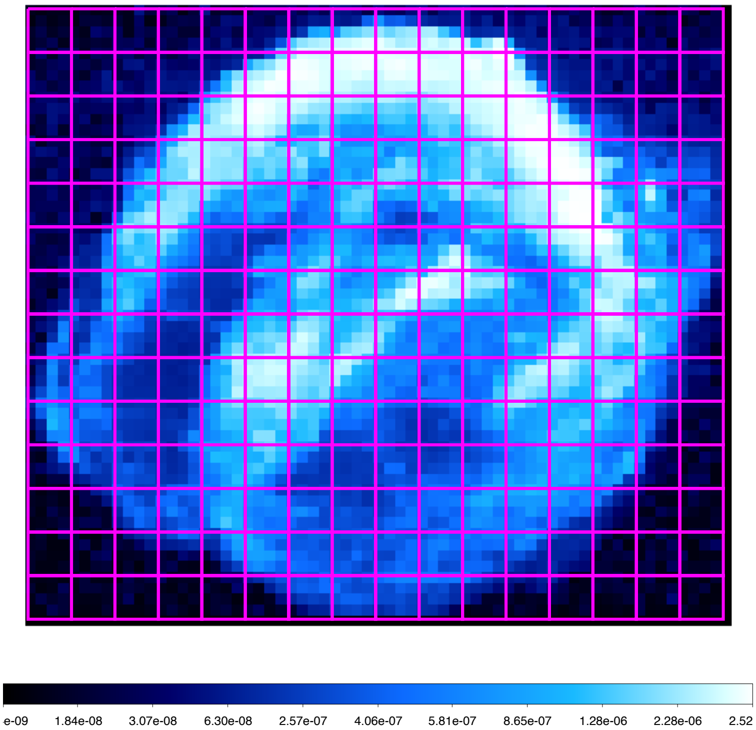

Si XIII (1.8–1.92 keV)

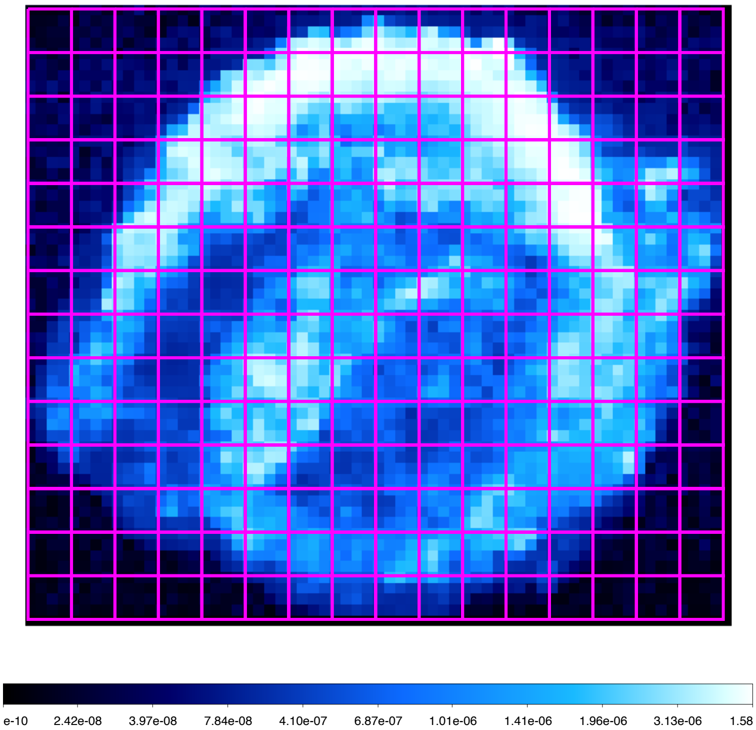

Figure 4.3: `(continued)`

S XV (2.4–2.52 keV)

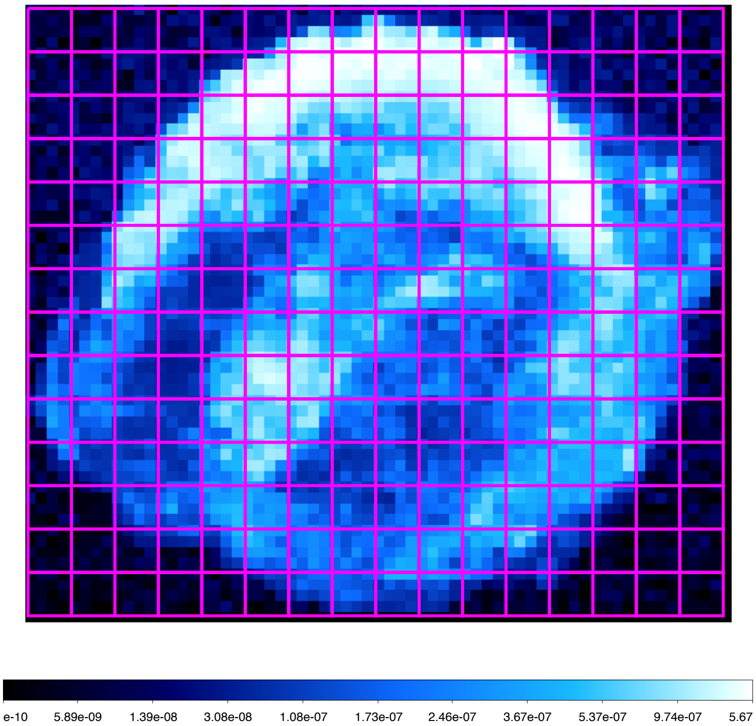

Ar XVII (3.07–3.18 keV)

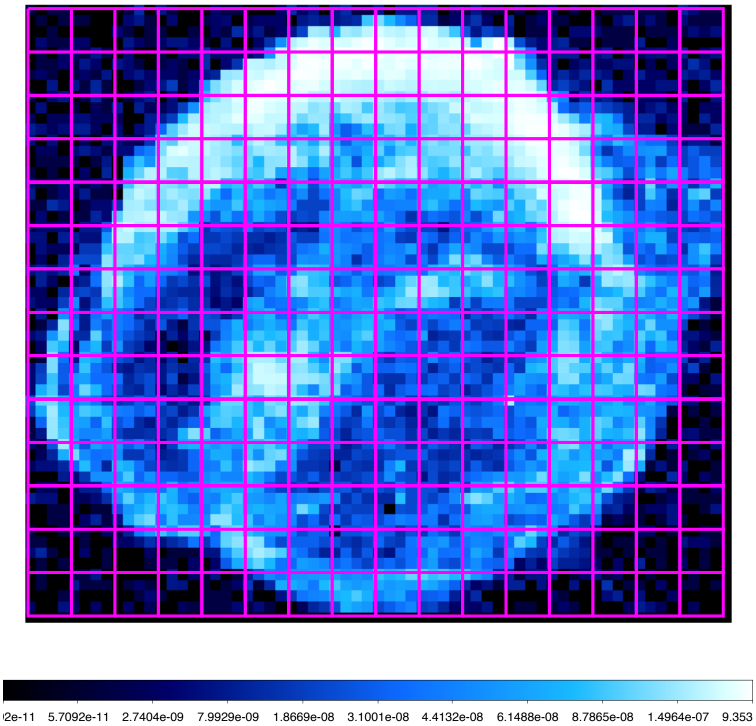

Figure 4.3: `(continued)`

Ca XIX (3.83–3.95 keV)

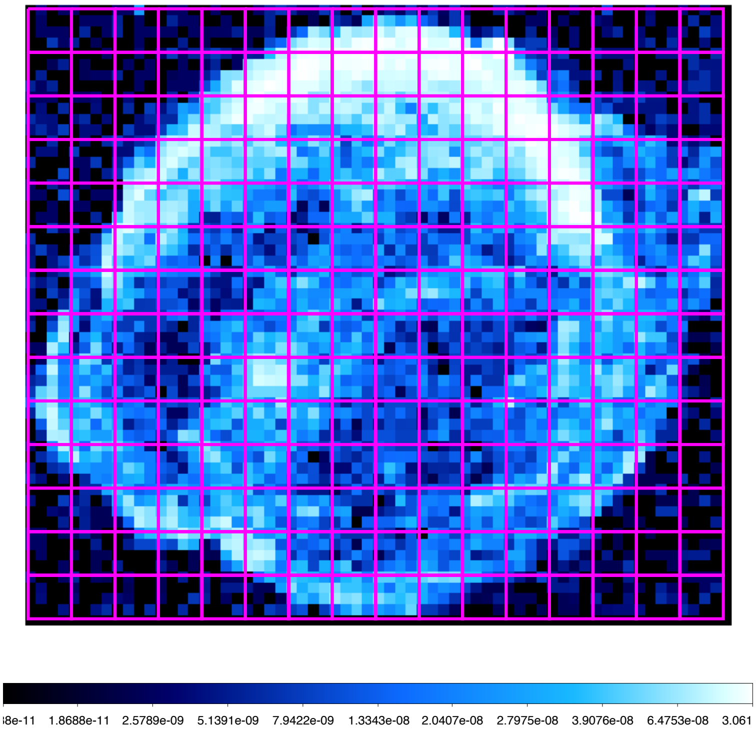

Fe-K (6.35–6.6 keV)

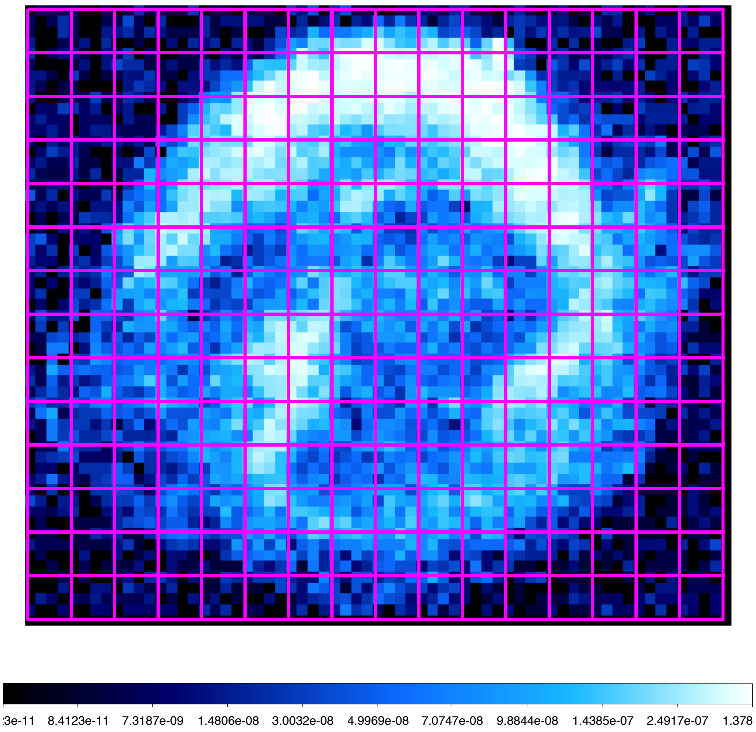

Figure 4.3: `(continued)`

4.4 Spectral fitting

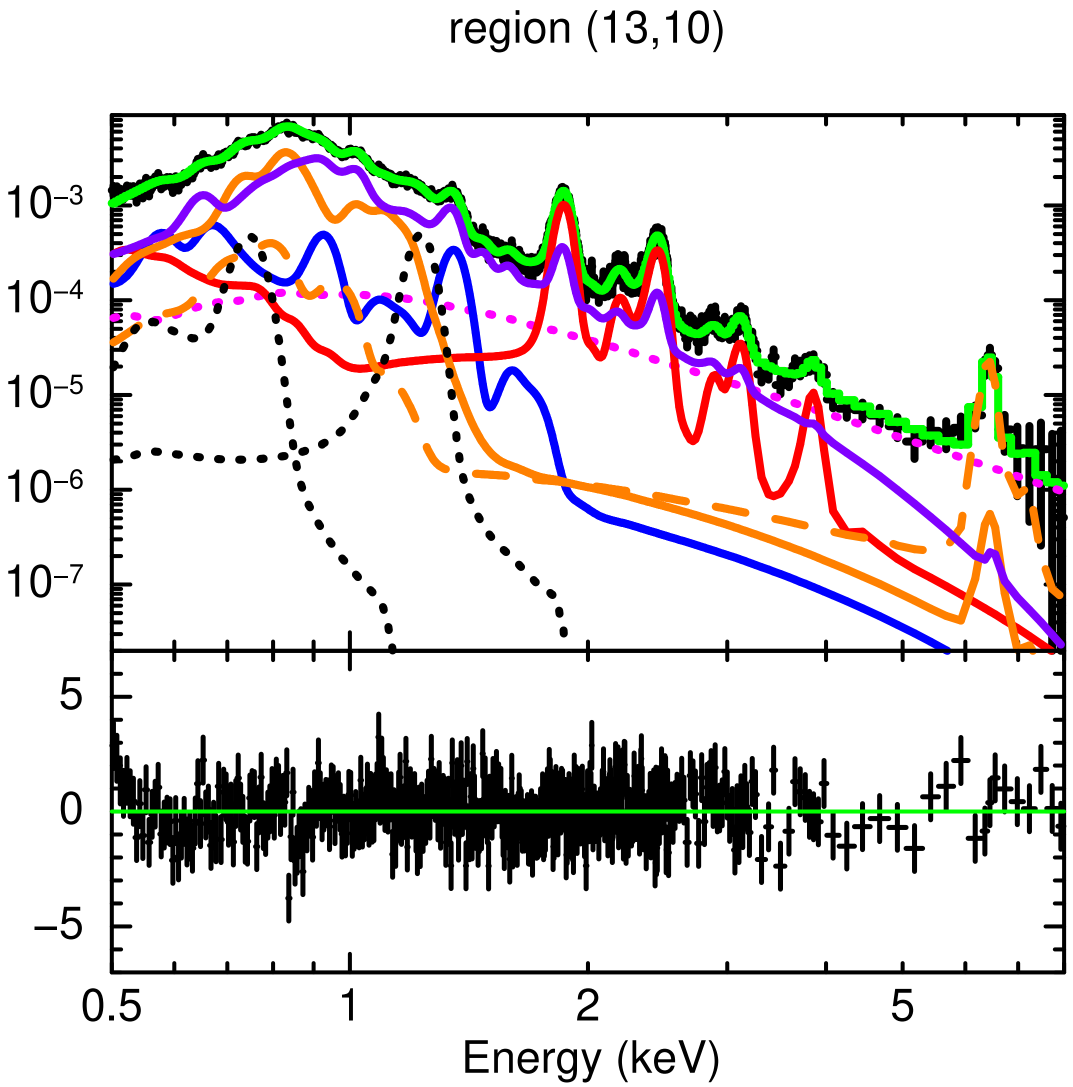

Figure 4.4: Example of the wide-band spectral fitting. *top*: Blue, red, and orange lines represent ONeMg, IME, and two IGE ejecta components, respectively, where those with solid line has the same electron temperature. The violet line represents the CSM component. Dotted black lines are two additional Gaussians and a dotted magenta line is a power-law component. *bottom*: The residual of fitting, showing `(data-model)/error`.

We extract the spectra from the wide X-ray band between 0.5 and 8.0 keV from each sky pixel. The energy band lower than 0.5 keV has a large uncertainty due to the small effective area or the absorption edges of instrumental elements. That higher than 8.0 keV includes little photons in the unit of a 15 arcsec square grid. In the chosen energy band, we can observe K-shell emission lines from oxygen to iron and L-shell emission lines from

IGEs (see Figure 4.2 and Table 2.1). We assume these elements are composed of the ejecta and CSM emissions. The ejecta include four groups of NEI plasma which follows the stellar evolution, whose abundance of heavy elements is extremely larger than those in the solar system. One includes relatively lighter elements: oxygen, neon, and magnesium (ONeMg). Another does Intermediate Mass Elements (IMEs), which means silicon, sulfur, argon, and calcium, with odd-Z elements including aluminium, phosphorus, and chlorine. For IGEs, we especially assume two components with different ionization timescales τ (see Equation 2.12). The Fe-Kα line from type Ia SNRs tends to be emitted from middle-ionized iron ejecta from Fe^{9+} (Ar-like) to Fe^{16+} (Ne-like) (cf., Yamaguchi et al., 2014a,b). On the other hand, the strong Fe-L lines come from a little higher ionized iron elements (Table 2.1). Therefore, Fe-K and Fe-L emission lines could come from differently ionized iron sources in young remnants. The CSM component is also assumed to be NEI plasma, but the abundance of heavy elements in CSM is near the solar abundance.

We adopt the `X-ray SPECtral fitting package (XSPEC) 12.11.1` (Arnaud, 1996) for spectral fitting with the `Atomic DataBase (AtomDB) 3.0.9` (Foster, 2015) as a dictionary of emissions of each line. `XSPEC` contains a lot of emission models. Representing the components described above, we use four `vvnei` models for the ejecta, which is the most flexible one in the NEI models in `XSPEC`. The `vvnei` model requires the electron temperature kT_e, the ionization timescale $n_\mathrm{e}t$, and the abundance parameters of each element compared to the solar abundance (Wilms et al., 2000). Although the 2-dimensional sky region in fact has its thickness in the line-of-sight direction, we assume the electron temperature of ONeMg, IME, and one IGE component are equal for simplicity. The ionization timescale of all four components are free each other.

Concerning the abundance parameter, we assume a pure-metal plasma whose abundance ratio of each element to the hydrogen is $\sim 10^5$ to ignore the contribution of hydrogen because of the characteristics of type Ia SN. In the ONeMg component, the abundance parameter of oxygen is fixed to 10^5 and those of neon and magnesium are free. In the IME component, the abundance parameter of silicon is fixed to 10^5 and those of sulfur, argon, and calcium are free. Because the emission lines from odd-Z elements tend not to be resolvable by CCD detectors, we link their abundance parameters and treat as only single parameter. In the two IGE components, we link the abundance of same elements with assuming that of iron is fixed to 10^5. Titanium abundance is a free parameter, which is linked to those of chromium and manganese. Because Ni-K emission line is out of the range of our energy band, the nickel abundance is fixed to 10^4 for not affecting our analysis. Notice that we add two more Gaussian components around 0.7 keV and 1.2 keV to represent missing or under-estimating Fe-L lines (cf., Katsuda et al., 2015).

For measuring the ejecta kinematics, we introduce two multiple models including `vmshift` for representing the Doppler shift and `gsmooth` for all of the line broadening effects. The `vmshift` shifts the emission model as $-Ev/c$, where E is the energy at the static state, v is the red-shifted velocity. The `gsmooth` represents a smoothing effect with the sigma as $\sigma(E/6)^{\alpha}$, where σ is the line width at 6 keV. We assume the linearity of σ over the entire energy band, thus α is set to be 1. These two parameters for the two IGE components are linked. Note that many previous works regards the red-shift parameter z of the `vvnei` model as an index of the line-of-sight velocity. However, we avoid using this parameter because it is accurately a "cosmological" red-shift, not a "kinematical" red-shift. The "cosmological" red-shift strictly affect the emission normalization by a factor of $(1+z)^{-2}$ even though such small $z \leq 0.01$ assuming the motion with <3,000 km sec^{-1} is ignorable.

In addition to the ejecta emission models, we also include another `vvnei` model for representing the CSM emission. For simplicity, the element abundance of the CSM model is fixed to the solar abundance (Wilms et al., 2000). Thermal parameters of it are fixed to the following values according to the results of Kasuga et al. (2021) (see Table 5.1): the electron temperature is 0.9 keV; the ionization timescale is 1.0×10^{11} cm^{-3} sec; the Doppler shift is -230 km sec^{-1}.

Other than thermal emission models, we also add one Power-Law model (`PL`) for the continuum components like the synchrotron radiation from high energy electrons accelerated on the shock front (cf., Bamba et al., 2005; Lopez et al., 2015). Finally, we consider the interstellar absorption effect by the Tuebingen-Boulder ISM absorption model (`tbabs`) (Wilms et al., 2000), whose value we fix to 5.7×10^{21} cm^{-2} in all sky pixels (Kasuga et al., 2021).

The spectral fitting process of `XSPEC` aims to maximize the likelihood. For the Poisson distributed data like the X-ray astronomy, this process is based on the C-statistics (Cash, 1979). The likelihood L for the N bin data is calculated as:

$$L = \prod_{i=1}^{N} \frac{(t_{\mathrm{s}} m_i)^{S_i} \mathrm{e}^{-t_{\mathrm{s}} m_i}}{S_i!} \ , \tag{4.1}$$

where S_i and m_i are the observed and model counts in each bin, and t_{s} is the exposure time. Then the C-stat value is:

$$C = 2 \sum_{i=1}^{N} [(t_{\mathrm{s}} m_i) - S_i \ln(t_{\mathrm{s}} m_i) + \ln(S_i!)] \ . \tag{4.2}$$

When we consider a background observation B_i with the exposure time t_{b} like our study, we adopt the W-statistics instead (Kaastra, 2017). We aim to minimize the W-stat value as:

$$\frac{W}{2} = \sum_{i=1}^{N} [(t_{\mathrm{s}} m_i) + (t_{\mathrm{s}} + t_{\mathrm{b}}) f_i - S_i \ln(t_{\mathrm{s}} m_i + (t_{\mathrm{s}} f_i)) - B_i \ln(t_{\mathrm{b}} f_i) - S_i(1 - \ln S_i) - B_i(1 - \ln B_i)] \ , \tag{4.3}$$

where

$$f_i = \frac{S_i + B_i - (t_\mathrm{s} + t_\mathrm{b}) + \sqrt{[(t_\mathrm{s} + t_\mathrm{b})m_i - S_i - B_i]^2 + 4(t_\mathrm{s} + t_\mathrm{b})B_i m_i}}{2(t_\mathrm{s} + t_\mathrm{b})} . \tag{4.4}$$

Because the limit of large numbers of counts of the Poisson distribution reaches the Gaussian distribution, W reaches the χ^2 with $(N - M)$ degrees of freedom, where M is the number of free parameters of the model.

4.5 Results

As a result of the spectral analysis in all sky pixels, the distribution of the W values is fit to the range from the half value to the twice value of the Degree Of Freedom (DOF: 1470) of each fitting (Figure 4.5). Although the W value (and also C value) has no exact method of test, this result can be interpreted that we generally succeed the spectral fitting with considering the characteristics of the chi-square method. Figure 4.6 shows spectral fitting results in the all sky pixels in Kepler's SNR. We succeed phenomenologically representing the observed spectrum in all pixels with almost no strong residuals remaining there.

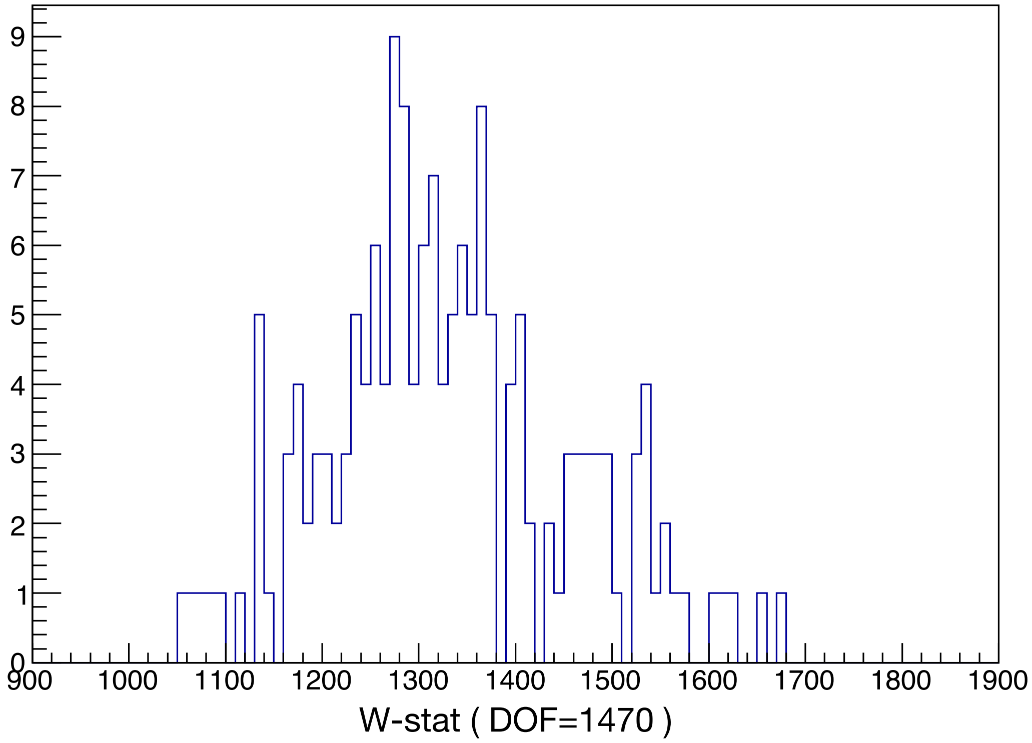

Figure 4.5: Histogram of W-stat values W of the fitting result in Figure 4.6.

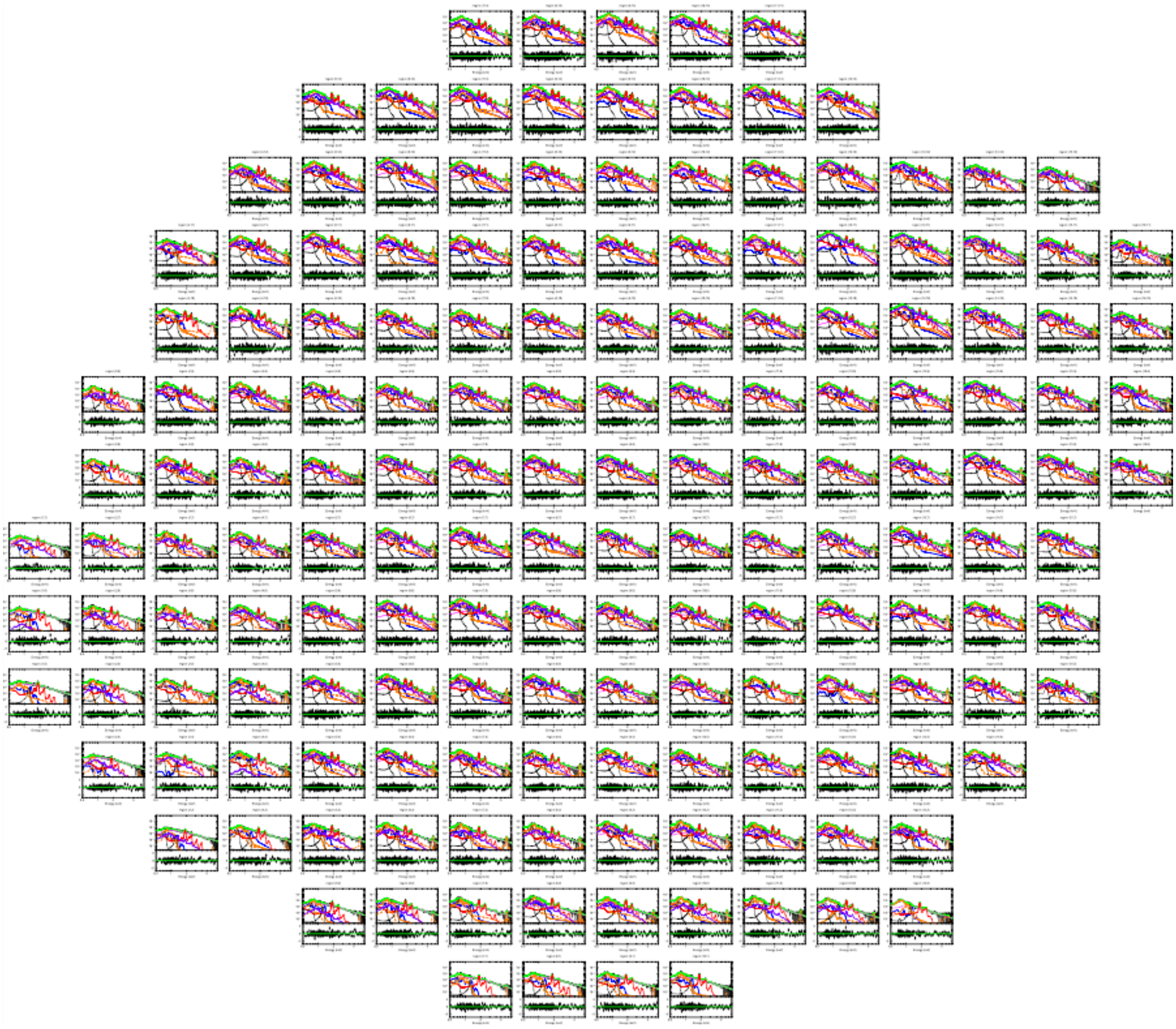

Figure 4.6: Spectral fitting results of Kepler's SNR. Full resolution data is available as electronic media.

4.5.1 Doppler shift

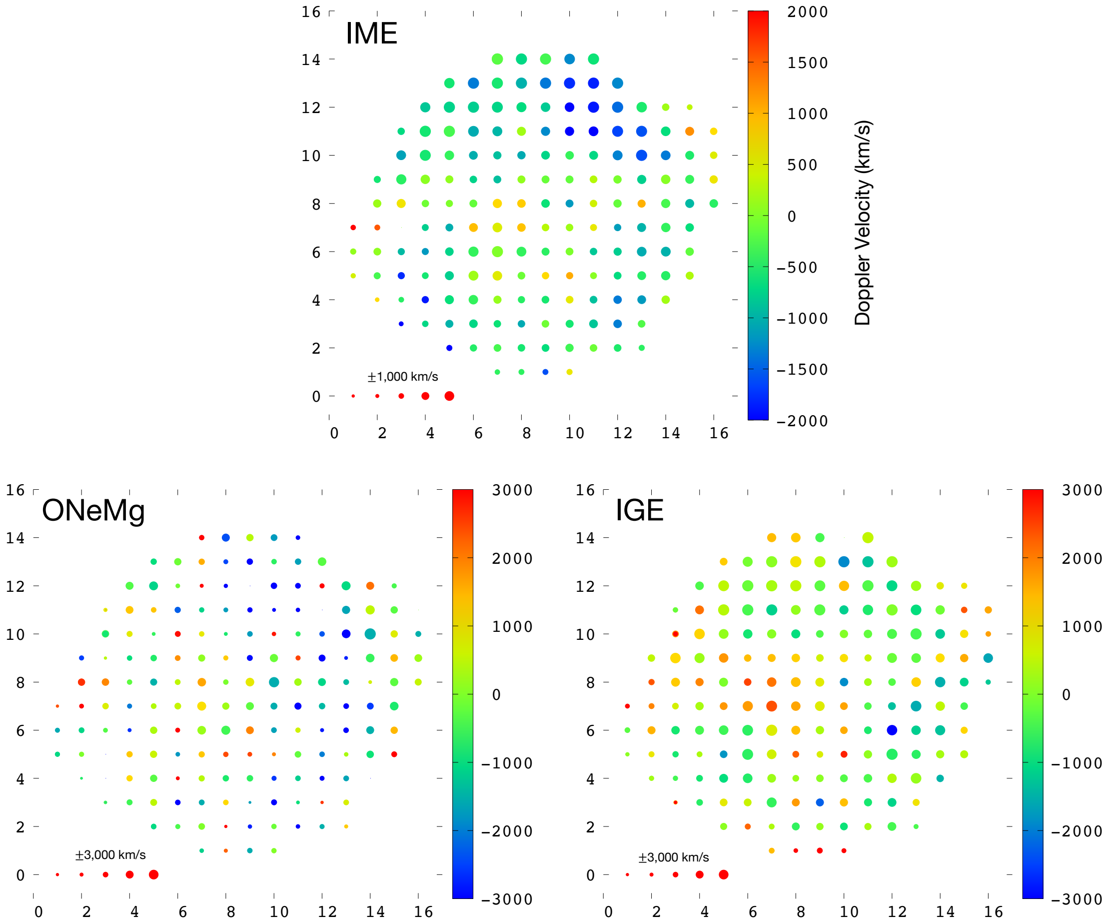

Figure 4.7: Doppler shift maps of Kepler's SNR. Numbers around these plots are the x and y coordinates corresponding with each (x,y) in Figure 4.6. The color scale represents the best-fit value of the line-of-sight velocity, where positive values mean red-shifted. The circle size represents the fitting error (1σ). The legends of the error scale are shown at the lower left corner. In five circles in the legend, the central one is the criterion, which represents the error value written above, and the ratio of the circle size (area) of each data point to the criterion is the reciprocal of the ratio of the fitting error. As examples, the other four circles in the legends represents ×3, ×2, ×1/2, and ×1/3 values comparing with the criterion, respectively.

Figure 4.7 shows the Doppler shift parameter maps of each ejecta component using the `vmshift` model. The size of each data point represents the estimated confidence region of the parameter fitting, which the `error` command in `XSPEC` calculates by searching the limit with varying all free parameters until the best statistic value is fit within the 1σ confidence level. For the IME component, the north-west rim shows blue-shifted feature and the central region does a little red-shifted velocity. The fitting error of the ONeMg component is too large to discuss the best-fit results, because we cannot resolve their emission lines clearly due to the worse energy resolution of CCD detectors. This situation also causes the uncertainties for Fe-L lines. Although the IME lines and ONeMg lines includes both ejecta component and CSM component and it makes uncertainties due to the assumption of the model parameters of the CSM component, the Fe-K line is purely from the ejecta. The Doppler velocity of the IGE component shows clearly red-shift result 2,000±1,000 km sec^{-1} around the center of the remnant. Kasuga et al. (2018), who analyzed another observation by *Chandra* ACIS-S detector, measured the Fe-K centroid there and found it shows lower than 6.4 keV, which is the centroid energy of Fe I. Our result reconfirm the red-shift structure there, and measure the velocity with considering the ionization state of the iron ion for the first time.

4.5.2 Line width

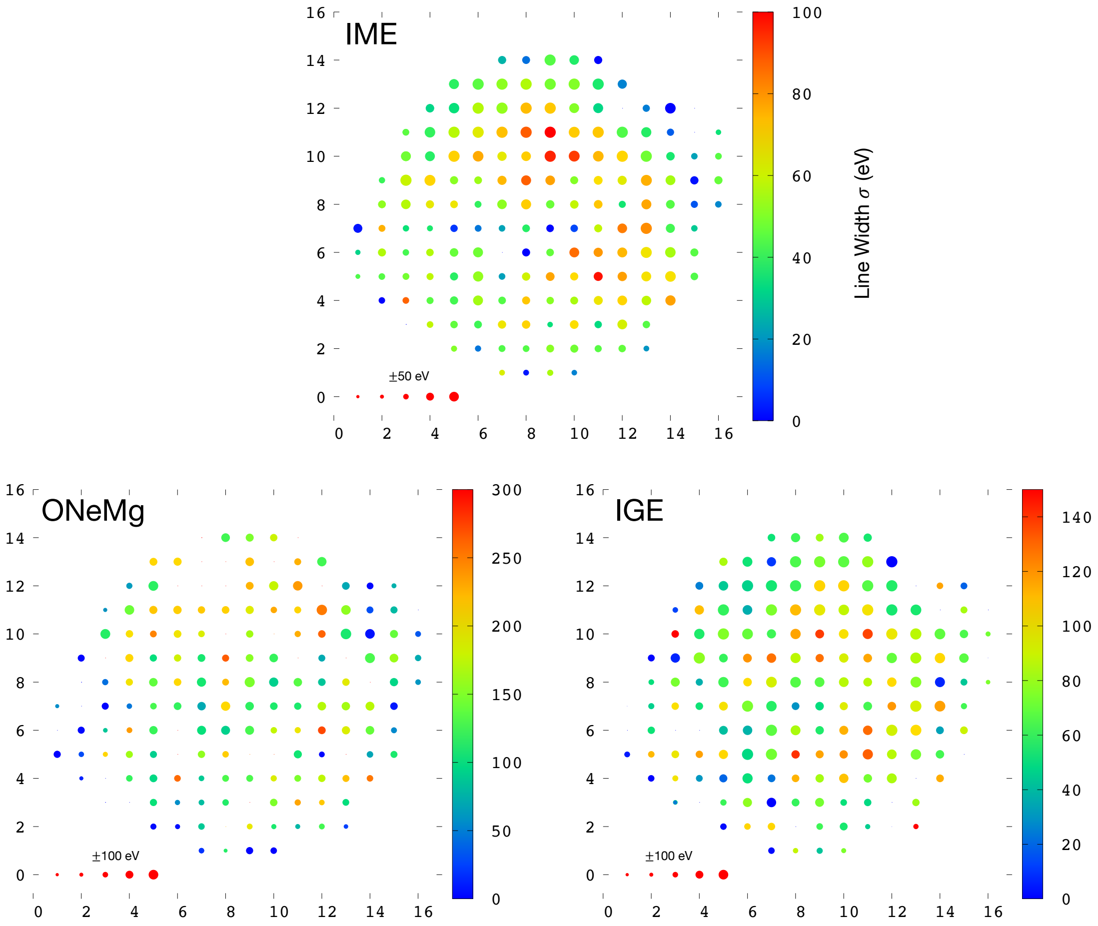

Figure 4.8: Same as Figure 4.7 but those of the line width. These values are linearly converted to those at 6 keV.

Figure 4.8 shows the line width parameter maps using the `gsmooth` model. These values are linearly converted from the line width at each line centroid energy to the value at 6 keV for simple comparison. While the line width of the ONeMg component is still not reliable due to the weak ejecta contribution, those of the IME and IGE around the center of the remnant show narrower values than those in the outer regions. Kasuga et al. (2018) suggested such a feature for the Fe-K line by calculating the standard deviation of incident photon energy detected there. We reconfirm it more precisely by measuring the line width directly. For confirming this narrow line width quantitatively, Figure 4.9 shows radial profiles of the line width of the IME emission lines. We can see the characteristic trend that the peak of the line width is located at a little outer from the center. This trend cannot be explained by a simple spherical expansion model surrounded by a uniform ISM, and the impact of dense CSM could be expected there.

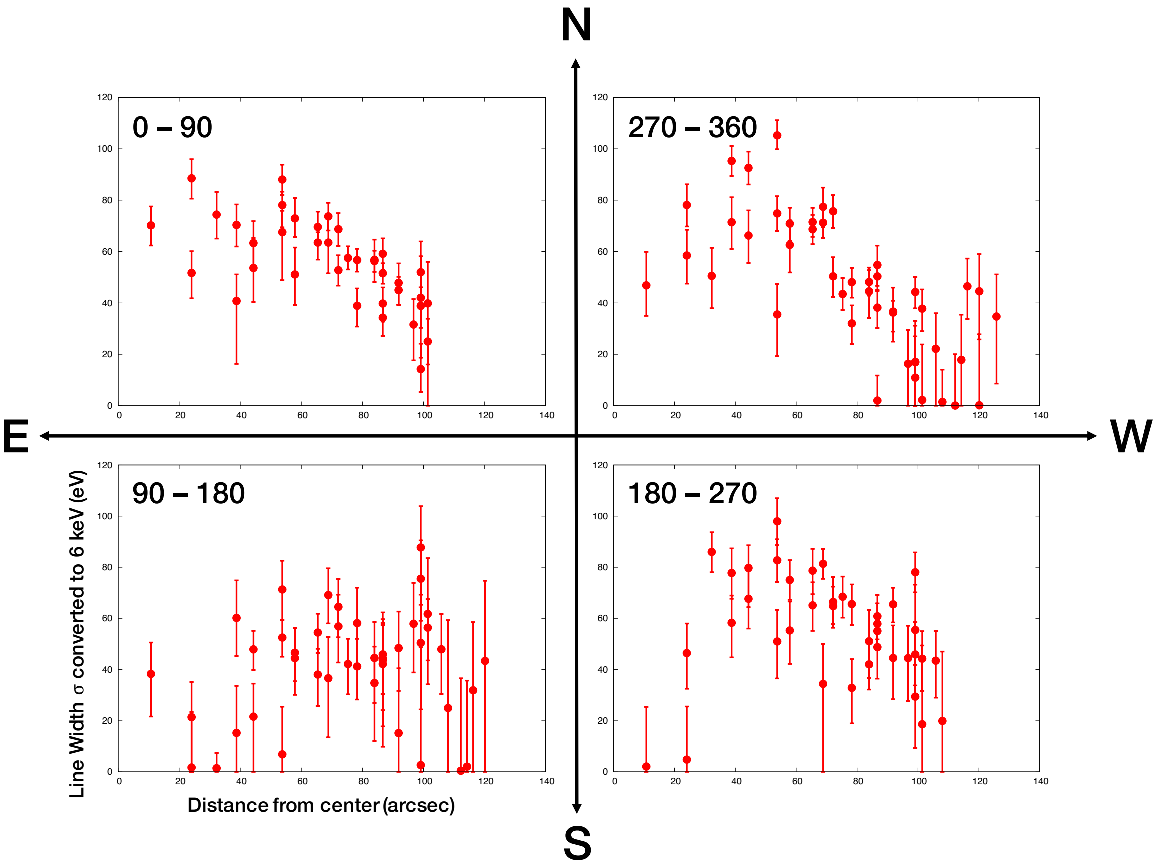

Figure 4.9: Radial profiles of the line width of IMEs. Numbers at the top left corner correspond to the range of the angle (degree) which is counter-clockwise from the north. Each error bar of red points is in the 1σ confidential range. Note that we exclude some pixels whose best-fit value is 0 eV and we cannot determine their upper limits due to their large fluctuations.

Chapter 5

High resolution spectroscopy of Kepler's supernova remnant

As described so far, the analysis of ONeMg-K and Fe-L lines is uncertain as long as using CCD detectors. This weak point is fatal for studying the relationship between the ejecta and CSM. In this section, we adopt grating spectrometers on board *XMM-Newton*, RGS, for resolving these emission lines in detail.

5.1 Extracting spectra

As described in §3.1.4, RGS is a 1-dimensional detector in the cross-dispersion direction. Green lines in Figure 5.1 are parallel to the dispersion direction of the RFC detectors, whose observation roll angle is 92.67 degree for this observation `0842550101`. We can divide this remnant following these lines into six strips. Except for the strips NN & S, the CSM distribution in the dispersion direction can be regarded as a point-like structure in the other four strips. These strips are suitable for the analysis of the RGS spectrum. Figure 5.2 shows the raw event count maps on both RFC detectors. The spatial distribution in the cross-dispersion direction is detected in all the energy band. Because the focal points of both RGS detectors are shifted in ∼5 arcsec in the cross-dispersion direction (see Figure 5.1) and this scale is comparable with the strip width, we can clearly find that the detected raw image is shifted on the RFC. We consider these shifts when we extract spectra properly.

In the same way as MOS analysis, the reprocessing and extracting process of RGS data is done by `rgsproc`, `rgsrmfgen`, `rgscombine` in the software package of `SAS`. Note that the original software for making response files `rgsrmfgen` is used only for point-like sources based on Equation 3.1. For considering the extent of the emission sources in the dispersion direction (Equation 3.2), we additionally use `rgsrmfsmooth` in the software package of `HEASoft`. Original response shape for single emission line assuming the delta-function generated by `rgsrmfgen` looks Gaussian-like. `rgsrmfsmooth` smooths it by using the distribution of the emission sources in the dispersion direction, where we use *Chandra* images for each strip.

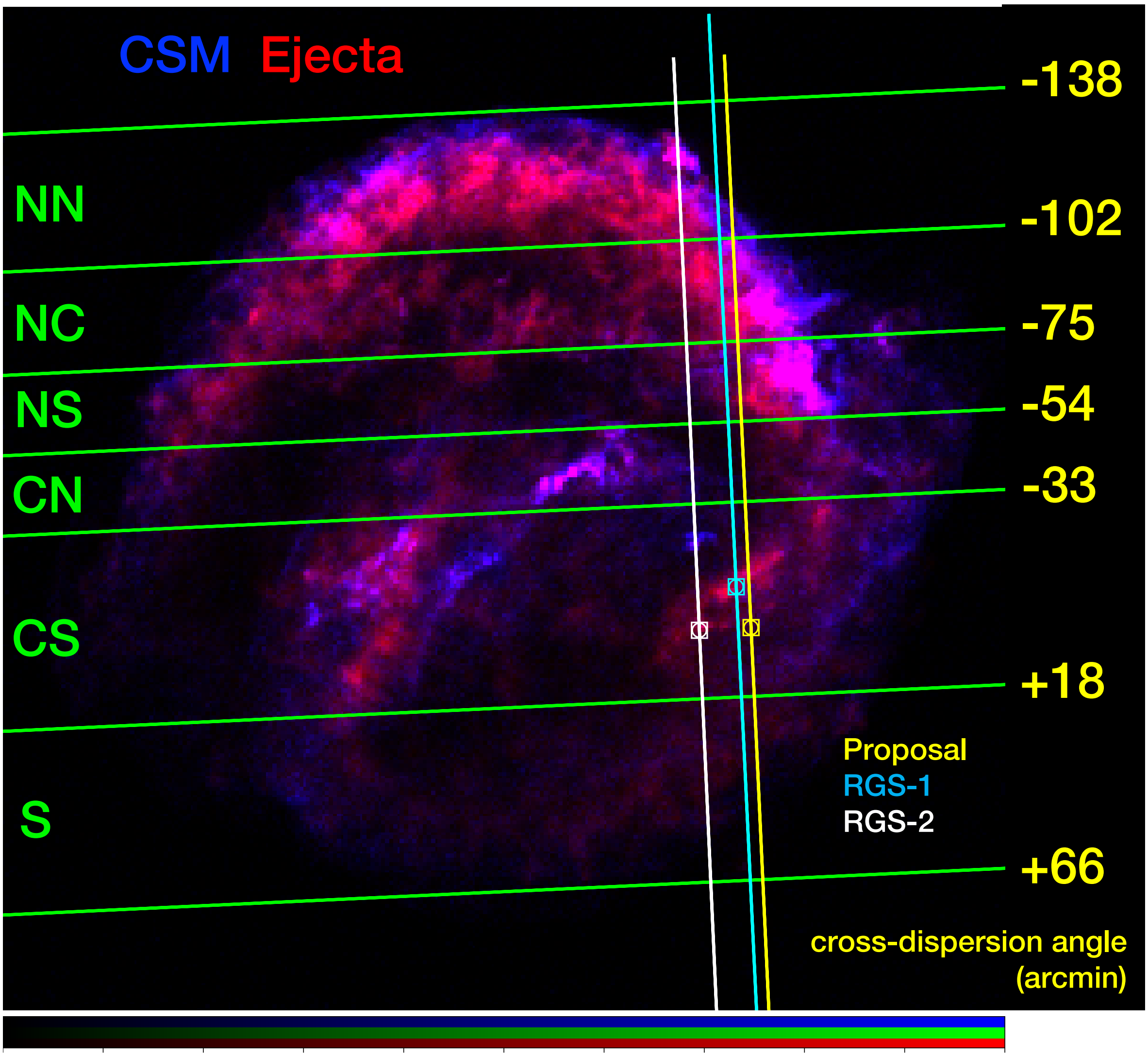

Figure 5.1: Analysis strips on the *Chandra* ACIS-S image of Kepler's SNR on a linear scale. The blue and red maps represent the CSM band (470–600 eV) and the ejecta (Fe-L: 700–860 eV), respectively. Note that the O Lyα line is not included in both of them. The yellow, cyan, and white color mean the distinction of the proposal value and the actual value of both RGS systems. The squares and vertical lines represent their focal point and cross-dispersion axes, respectively. The green horizontal lines represent the dividing positions of each strip, and the yellow values are the cross-dispersion angle of them normalized to the proposal focal point.

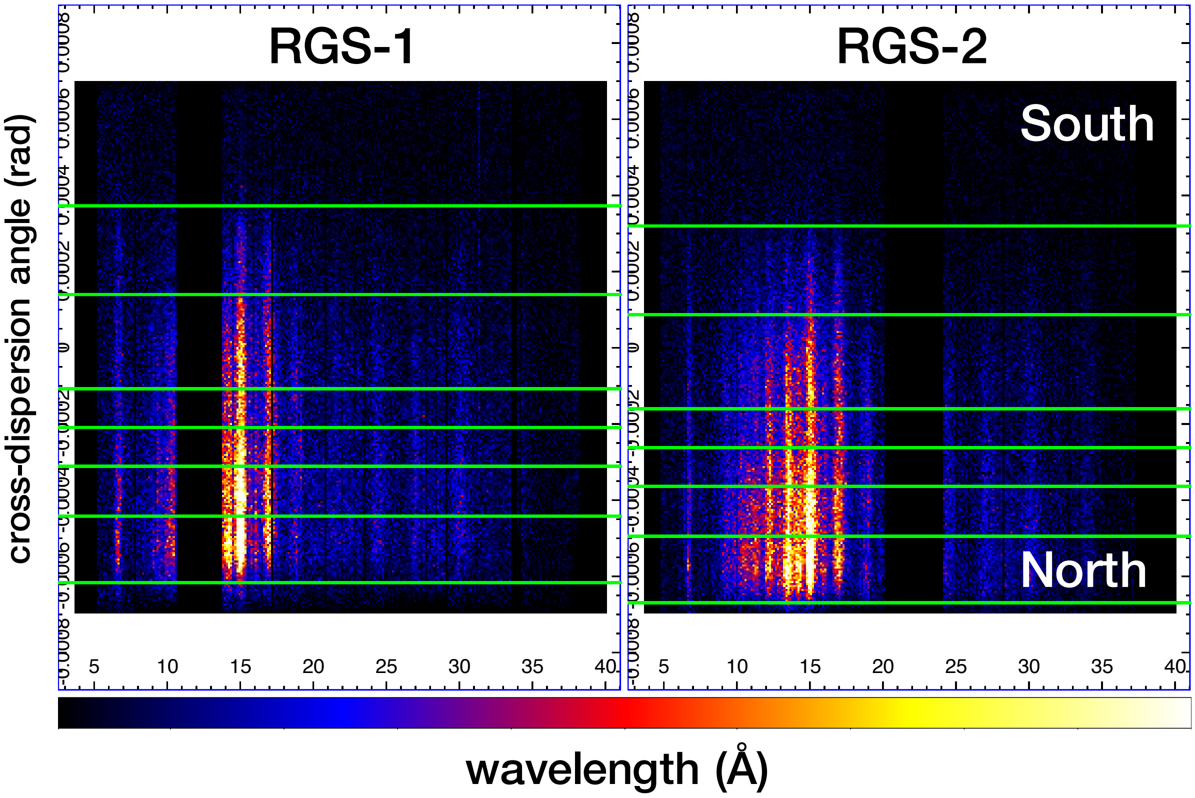

Figure 5.2: Raw event count maps of both RFC detectors in the RGS system with the region strips. The scales are linear to emphasize the spatial distribution of the brightness. We can see gaps due to the broken CCDs in each RFC detector.

5.2 Spectral fitting

For concentrating on the emission lines from nitrogen and oxygen, which are the main indicators of the CSM component, we choose the energy band only between 470–860 eV. In this narrow energy band, we assume only two NEI components, where one represents the CSM emission lines and the other does Fe-L ejecta lines. Following the previous study (Katsuda et al., 2015), we adopt `vpshock` model for the CSM component, which assumes that a plane-parallel shock heats elements. The NEI component of the Fe-L lines is still a `vvnei` model similarly to the MOS analysis. For considering different distribution of emission sources in each component, the detector response of the former component is smoothed by the CSM band image (470–600 eV, see the blue map in Figure 5.1) and that of the latter is by the Fe-L band image (700-860 eV, the red map). We also adopt a power-law component using `PL` model to represent all of the other weak emissions. We admit this `PL` model is completely phenomenological and the parameter of it may have no meanings for astrophysics, but it does not affect the Doppler parameters of emission lines dramatically. The fitting results are shown in Figure 5.3.

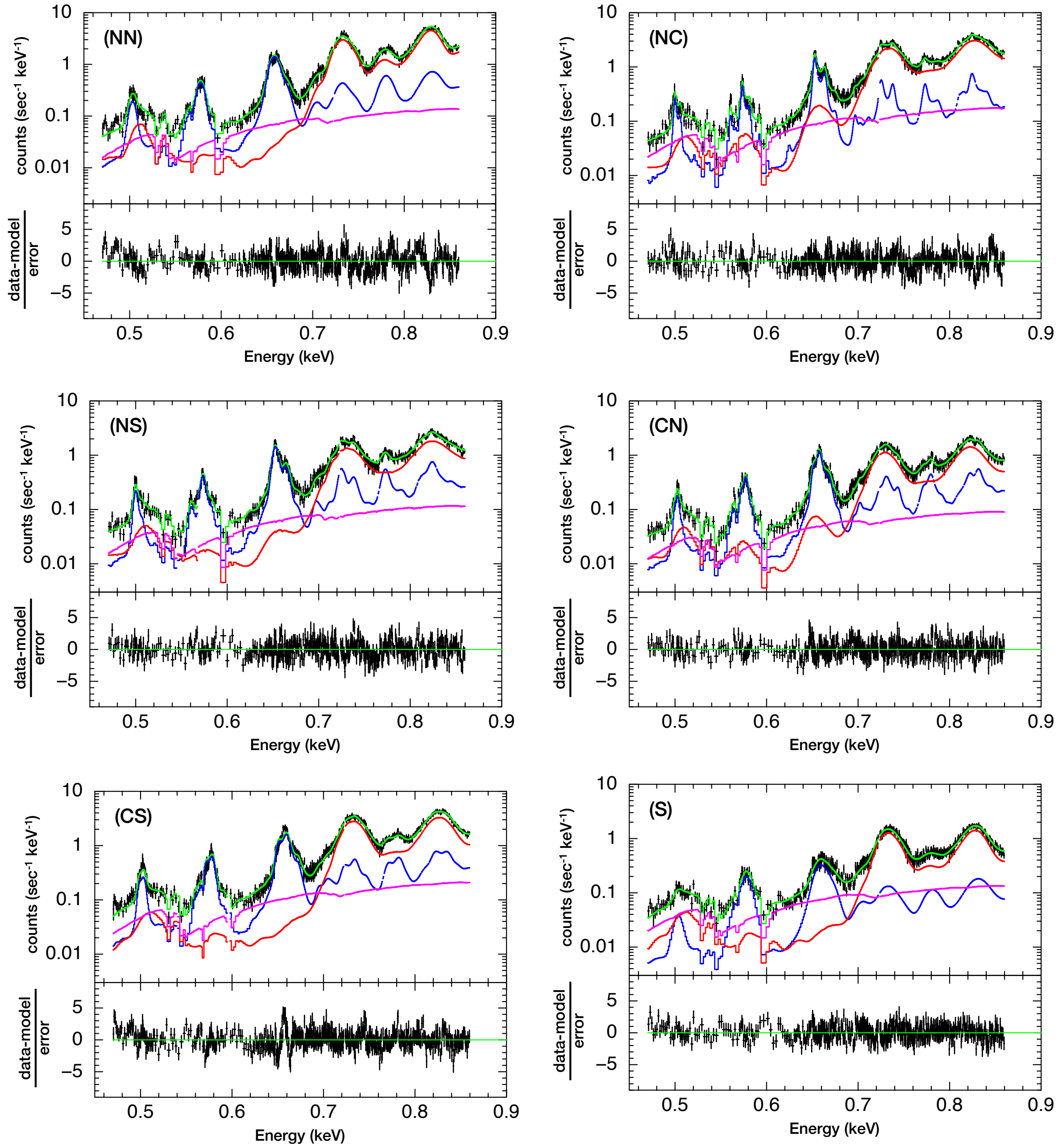

Figure 5.3: Fitting results in each strip. Blue lines are `vpshock` components representing the CSM emission lines, and red lines are `vnei` of the ejecta. Magenta lines are the `PL` component.

Before discussing Figure 5.3, we should pay attention to the residual around the O Lyα line at the strip CS. Nevertheless, we succeed in representing all the other spectral shapes including other strips, we only fail to reproduce this line feature. The analyzing method so far is valid when we can regard that each strip consists of only one point-like emission structure, and it is reasonable for the strip NC, NS, and CN, thanks to its biased emission (see Figure 5.1). The strip NN and S cannot be treated as a point-like but a continuous structure. However, only the strip CS consists of two independent emission structures. As shown in Figure 5.4, the component at the west half of the strip CS looks connecting the bright edge of the northern structure, whereas the other component is located at the central bar structure. It is more natural to assume that the velocity structure of these components are different. For this point, we virtually treat this 1-dimensional detector as a 2-dimensional one. By introducing the half-masked image to smooth the response files, we introduce the west and east half components for each two NEI models (cf., Katsuda et al., 2013). The updated fitting result is shown in Figure 5.5. This four-component model succeed in cancelling the outstanding residual in Figure 5.3 (CS).

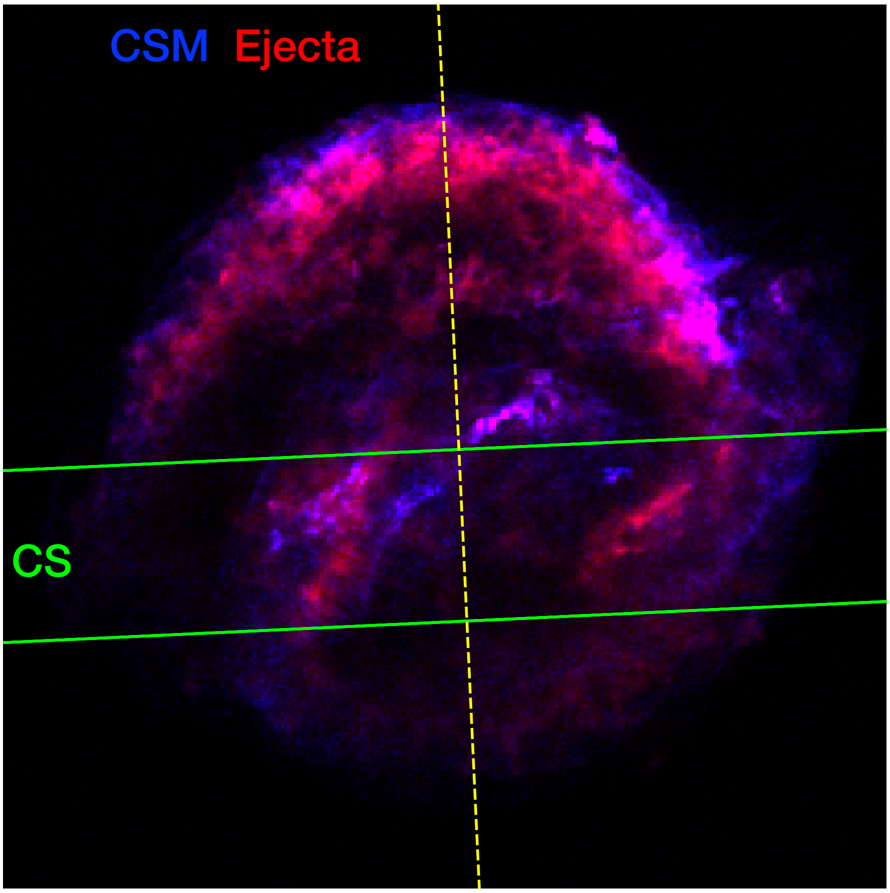

Figure 5.4: Same as Figure 5.1 but only showing the strip CS. The yellow dashed line is the dividing position of two halves, which is parallel to the cross-dispersion direction.

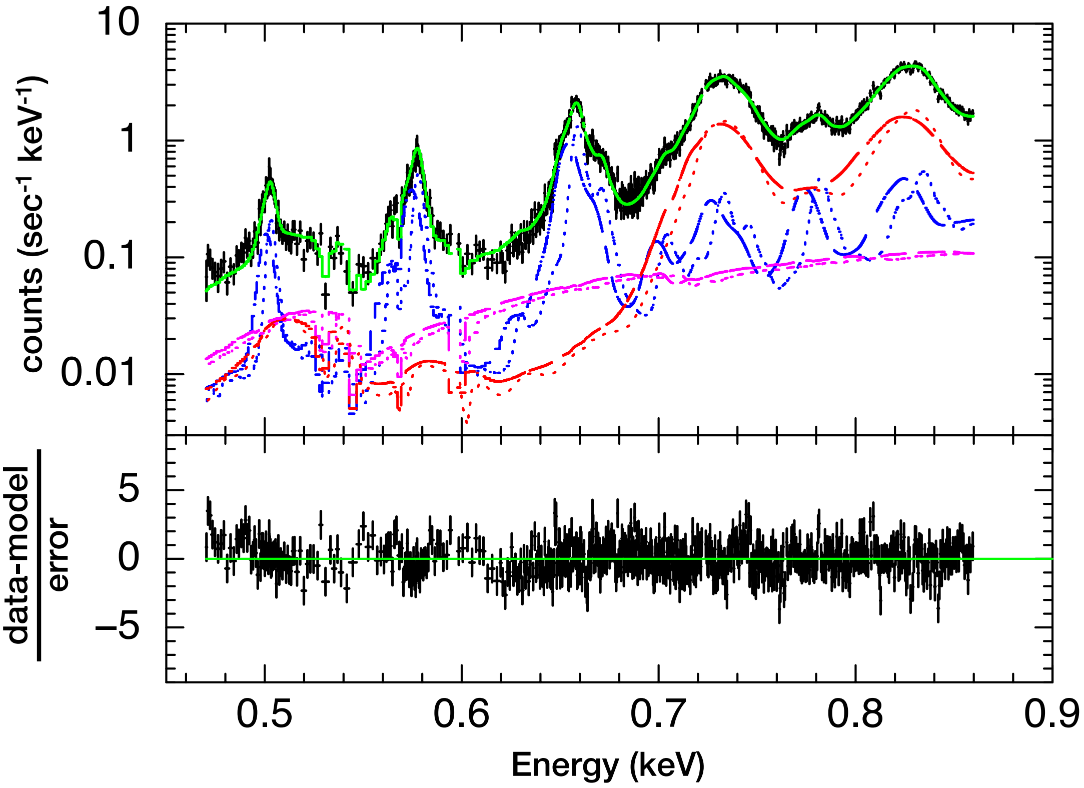

Figure 5.5: Same as Figure 5.3 (CS) but using improved models considering different velocity structures of the west and east halves. Dashed lines represent the components from the west-half and dots do the east.

5.3 Results

Table 5.1 shows the results of fitting parameters in this analysis. Figure 5.6 picks up parameters concerning the Doppler kinematics configured along the cross-dispersion direction. The strip CN and the east half of the strip CS, which can be regarded as being located at the central bar, shows relatively red-shifted result in the Fe-L component. Their line width looks not so wide in spite of their location. It is consistent result with what we derived in Chapter 4. In addition to this, the CSM component in the east half of the strip CS also shows highly red-shifted. On the other hand, the ejecta shows generally red-shifted trend, whereas the CSM shows blue-shifted. Based on these results, we discuss the general dynamics of Kepler's SNR in the next chapter.

Table 5.1: Best-fit NEI parameters.

Strip	NN	NC	NS	CN	CS-E	CS-W	S
Region	Edge	Edge	Edge	Center	Center	Edge	Edge
CSM							
velocity (km s^{-1})	-136^{+44}_{-109}	-192^{+29}_{-29}	-419^{+38}_{-41}	-562^{+36}_{-56}	738^{+75}_{-60}	-539^{+280}_{-290}	-86^{+135}_{-160}
line width σ (eV @ 1 keV)	$6.3^{+0.1}_{-0.4}$	$1.4^{+0.2}_{-0.2}$	$3.6^{+0.2}_{-0.2}$	$2.1^{+0.3}_{-0.2}$	$2.3^{+0.3}_{-0.3}$	$5.2^{+0.6}_{-0.6}$	$7.9^{+0.7}_{-0.6}$
kT_e (keV)	$0.85^{+0.10}_{-0.09}$	$0.51^{+0.07}_{-0.05}$	$0.58^{+0.06}_{-0.04}$	$0.66^{+0.10}_{-0.04}$	$0.90^{+0.11}_{-0.22}$		$0.91^{+0.28}_{-0.17}$
$n_\mathrm{e}t$ (10^{10} cm^{-3} s)	$5.5^{+1.0}_{-0.8}$	$12.9^{+2.5}_{-2.8}$	$11.2^{+1.7}_{-2.0}$	$7.8^{+1.7}_{-1.5}$	$3.9^{+0.8}_{-0.4}$		$2.5^{+0.7}_{-0.5}$
N (solar)	$1.51^{+0.18}_{-0.11}$	$2.04^{+0.19}_{-0.19}$	$1.77^{+0.16}_{-0.16}$	$1.41^{+0.14}_{-0.14}$	$1.54^{+0.11}_{-0.10}$		$0.77^{+0.23}_{-0.23}$
other elements (solar)	1	1	1	1	1		1
Ejecta							
velocity (km s^{-1})	702^{+33}_{-34}	532^{+53}_{-47}	578^{+75}_{-38}	1805^{+104}_{-63}	2531^{+280}_{-289}	-321^{+361}_{-323}	615^{+61}_{-59}
line width σ (eV @ 1 keV)	$9.6^{+0.1}_{-0.1}$	$13.9^{+0.3}_{-0.2}$	$14.8^{+0.4}_{-0.4}$	$12.1^{+0.4}_{-0.4}$	$10.6^{+0.7}_{-0.6}$	$15.6^{+1.0}_{-1.3}$	$10.1^{+0.3}_{-0.2}$
kT_e (keV)	$0.74^{+0.05}_{-0.03}$	$0.66^{+0.04}_{-0.02}$	$0.65^{+0.06}_{-0.04}$	$0.56^{+0.04}_{-0.04}$	$0.43^{+0.01}_{-0.00}$		$0.43^{+0.01}_{-0.00}$
$n_\mathrm{e}t$ (10^{10} cm^{-3} s)	$2.4^{+0.1}_{-0.1}$	$2.6^{+0.3}_{-0.2}$	$2.5^{+0.4}_{-0.3}$	$3.1^{+0.8}_{-0.4}$	$18.3^{+5.6}_{-5.0}$		$18.4^{+6.3}_{-3.3}$
H,He,C (solar)	1	1	1	1	1		1
N (solar)	0	0	0	0	0		0
O,Ne,Mg (10^3 solar)	< 1.8	$3.9^{+0.7}_{-0.4}$	< 1.3	$1.5^{+0.5}_{-0.6}$	< 0.3		< 0.3
Si,S,Ar,Ca (10^3 solar)	100	100	100	100	100		100
Fe,Ni (10^3 solar)	117^{+42}_{-8}	128^{+25}_{-25}	77^{+21}_{-15}	66^{+17}_{-11}	68^{+19}_{-21}		44^{13}_{-5}
Total							
n_H (10^{21} cm^{-2})	$5.7^{+0.2}_{-0.2}$	$5.6^{+0.2}_{-0.2}$	$5.5^{+0.2}_{-0.3}$	$5.4^{+0.2}_{-0.3}$	$5.8^{+0.2}_{-0.1}$		$5.3^{+0.1}_{-0.2}$
W-stat	1681.47	1602.46	1584.98	1410.52	1323.61		1233.72
DOF	1131	1131	1131	1131	1127		1131

Errors are shown in 1σ confidential level.

(a) velocity (km s^{-1})

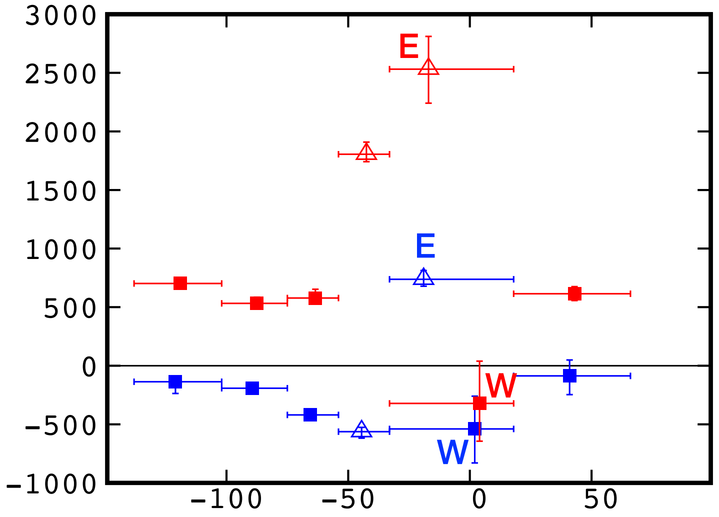

(b) line width σ (eV @1 keV)

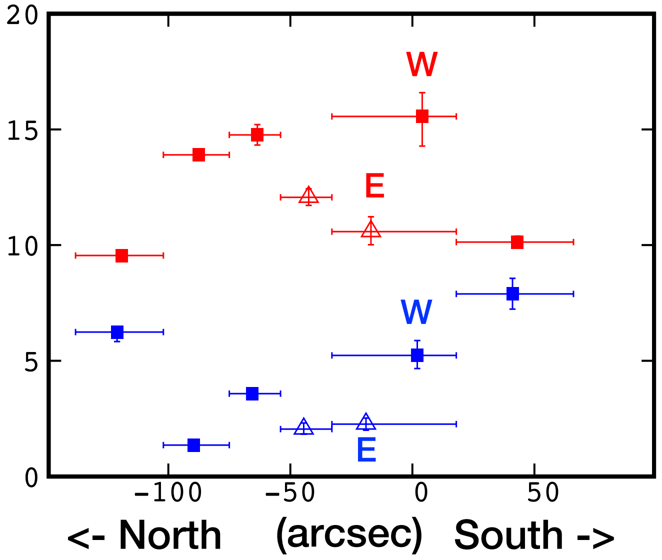

Figure 5.6: Results of the free parameters of our fitting with 1σ confidence level. The horizontal axis is the cross-dispersion angle in the unit of arcsec, which is shown in Figure 5.1. (a) Line-of-sight velocity. The positive values mean red-shifted, i.e., moving away from us. The blue points show CSM parameters and the red shows ejecta ones. The filled square points represent components in the outer rim and outlined triangle points do in the central bar. The black solid line means 0 km sec^{-1}. For the strip CS, we distinguish the plots from the west and east halves. (b) Same but line width σ converted at 1 keV.

Chapter 6

Dynamics of Kepler's supernova remnant

6.1 Asymmetric kinematics of CSM

According to the RGS analysis (Figure 5.6), the CSM around this remnant shows generally blue-shifted kinematics. Its velocity is distributed in the range of 0–500 km sec^{-1}. This velocity is quantitatively consistent with the bulk motion of this remnant $\sim$230±50 km sec^{-1}, which is estimated from some bright optical knots (Minkowski, 1959). Combining with studies of proper motions, Bandiera & van den Bergh (1991) measured its 3-dimensional velocity as 278±12 km sec^{-1} moving toward north-west and us. Previous studies claimed that such bulk motion is originated from a "runaway" AGB star of its progenitor system (Bandiera, 1987; Borkowski et al., 1992). Indeed, such "runaway" massive stars are still found even 600 pc above the galactic plane like Kepler's position (Martin, 2006). For example of Mira's binary, its velocity is $\sim$100 km sec^{-1} and it has a bow-shock in the infrared and ultraviolet energy band (Martin et al., 2007).

The central bar structure, which is located at the strip CN and the east half of CS, seems to have a different velocity structure. The RGS analysis shows the north half of the bar is blue-shifted and the south half is red-shifted. Hα observation, which is an indicator of the heated CSM, by Blair et al. (1991) reported consistent results. They measured the line centroid difference of broad Hα between the east half of CS and other region as $\sim$20 Å for 6562.8 Å, and it is converted to $\sim$1,000 km sec^{-1} difference in the line-of-sight direction (see Table 3 in Blair et al., 1991). Burkey et al. (2013) proposed a dense torus-like CSM for the central structure. The progenitor wind from WD in the SD scenario could generate such torus-like shape (Hachisu et al., 2008), and some other examples have been found like SN2012dn (Nagao et al., 2017) and SNR N103B (Yamaguchi et al., 2021). Our result of the red-shifted and narrow line feature of the CSM lines there is explainable by such a torus-like structure, if the torus leans toward north-west and us.

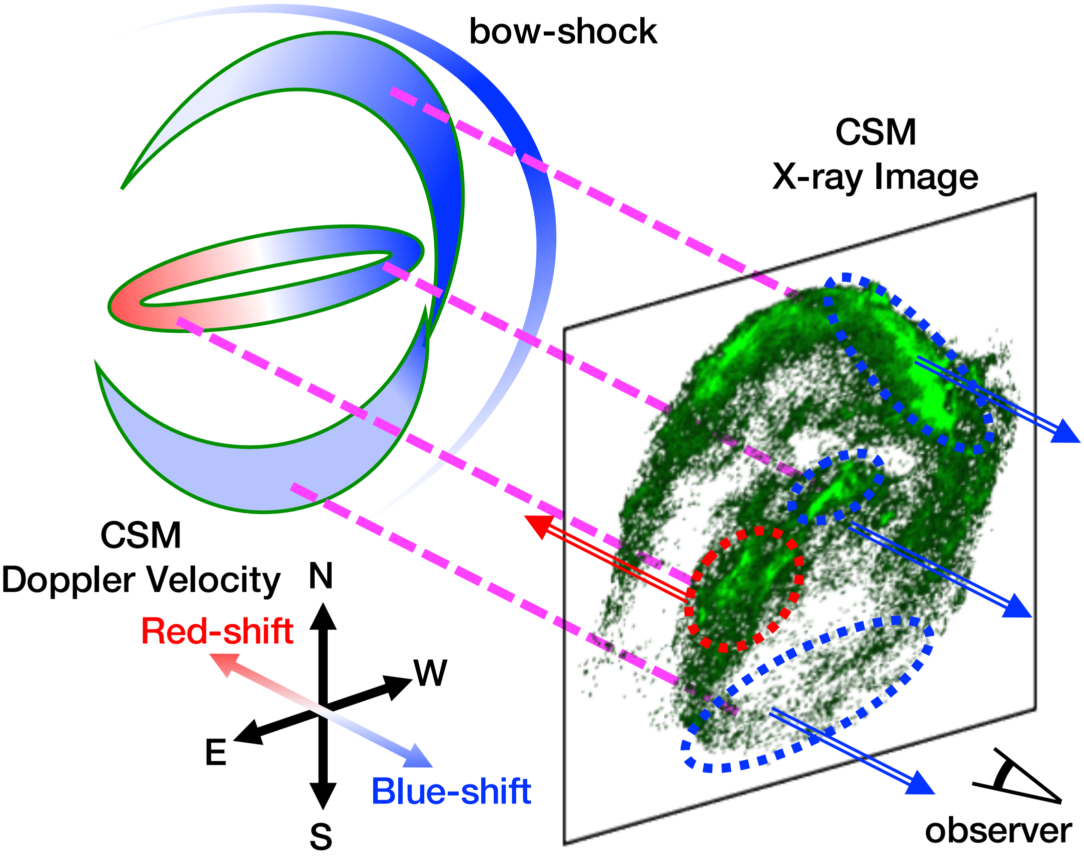

Figure 6.1: A schematic view of the kinematics of the CSM in Kepler's SNR from diagonally above. The blue or red color surrounded by green lines represents the Doppler-shifted direction of CSM. Darker color represents a larger shifted component. We also add a bow-shock generated by the "runaway" AGB star. The green image is the X-ray image of CSM (same as Figure 5.1) and colored arrows also represent the Doppler shifted direction at each position.

Figure 6.1 summarizes our view of the CSM kinematics discussed above. The original shape of CSM is bipolar-like with a dense torus at the center (Burkey et al., 2013). The entire system is pulled along the bulk motion of its progenitor system moving toward the north-west and our direction (Bandiera & van den Bergh, 1991). We also add a bow-shock image generated by such kinematics (Borkowski et al., 1992). Previous 2-dimensional simulations also supported this kinematics. A "runaway" AGB star picture was assumed in some works with an isotropic CSM structure (Borkowski et al., 1992; Velázquez et al., 2006; Chiotellis et al., 2012). Burkey et al. (2013) also did with a torus-like CSM structure in a static system. These simulations succeeded in generating the characteristic structures of Kepler's SNR. Toledo-Roy et al. (2014) combined both assumptions and generated general X-ray emission structure in a 3-dimensional simulation.

6.2 Asymmetric kinematics of ejecta

The line width of the ejecta component by our RGS analysis (Figure 5.6) is the quantitative reconfirmation of our MOS analysis that the line width gets narrower at the central bar of Kepler's SNR. This result can be interpreted as a small velocity difference of $(v_\mathrm{r} - v_\mathrm{b})$. Our RGS result also shows the line width of CSM there is narrower than almost other strips. These results shows that the dense torus-like CSM there inhibit the ejecta expansion. The observed Doppler shift of the ejecta reflects the difference of the timing of heating by the reverse shock between our side and the other side in the line-of-sight direction.

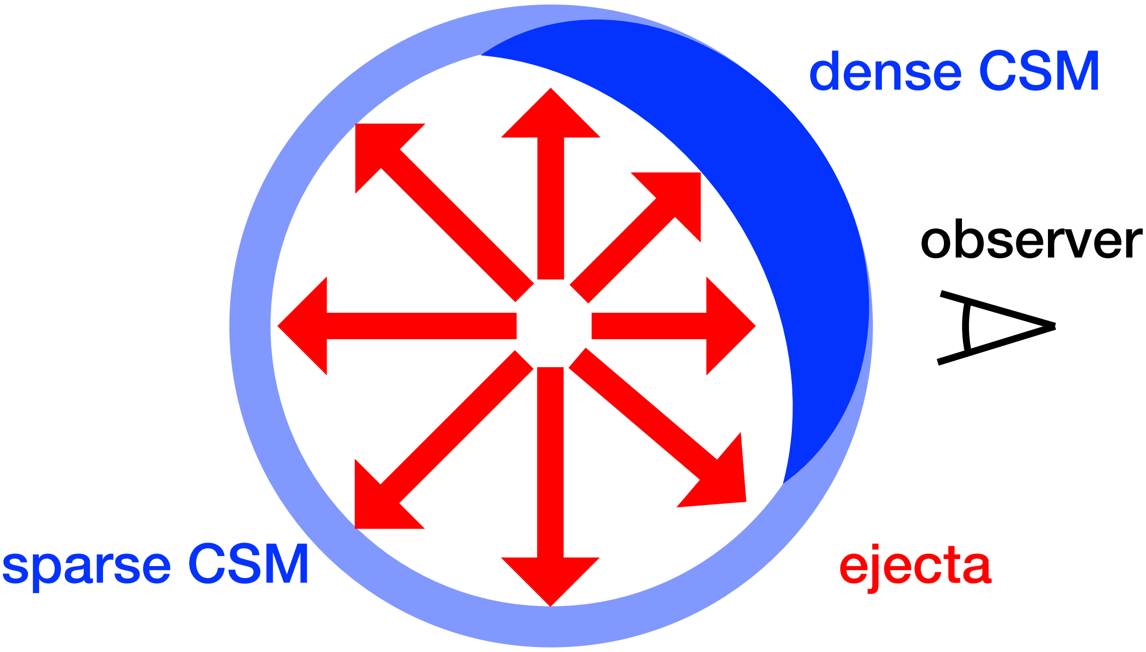

Figure 6.2: A schematic view of the kinematics of the ejecta in Kepler's SNR.

We treat the ejecta kinematics in the outer region independently to the central structure. Our RGS result shows the ejecta generally shows red-shifted results in contrast to the CSM and the bulk motion (Figure 5.6). We interpret this CSM result that the CSM in Kepler's SNR is mainly distributed on our side (Figure 6.1). Figure 6.2 shows this situation again but in terms of the orthogonal direction to the line-of-sight. When surrounded by this distribution of CSM, the kinematics of the ejecta moving towards us is decelerated by the dense CSM and not inhibited in the other side. If that deceleration is $\sim$1,000 km sec^{-1}, the integrated line-of-sight velocity is totally red-shifted with $\sim$1,000 km sec^{-1}. Therefore, combining with the result at the central structure, our results show the evidence of the obstruction of the ejecta kinematics by the dense CSM.

6.3 Comparison with forward shock observations

The angular motion of the forward shock at the outer edge has already been measured in detail. Katsuda et al. (2008) analyzed the *Chandra* ACIS images of Kepler's SNR, which are observed in 2000 and 2006, and found the angular velocity of the shock front at the north half is $\sim$1,000 km sec^{-1} slower than that at the south half. They interpreted that it reflects the higher density of the CSM around the north rim. Coffin et al. (2021) studied this point again with newer observations in 2014, which help us to measure the time variation of the angular velocity. This new study reconfirmed the trend what Katsuda et al. (2008) found, and also found the velocity is not changed in this $\sim$10 years. They discussed that the deceleration at the north half has already been finished. It means we observe the old interaction between the CSM and the remnant in the angular direction. Although our study in the line-of-sight direction is difficult to discuss the historical timing of the interaction, all of the results shows the clear evidence of the interaction between the SNR evolution and its dense CSM.

Chapter 7

Spatially resolved spectroscopy of Tycho's supernova remnant

Next, we measure the ejecta velocity structure in an SNR without any detected CSM. Tycho's SNR is the best target for this study because it is one of the brightest and youngest type Ia SNRs that we have detected and its thermal emission is only observed from the ejecta (Decourchelle, 2017, for a review). Note that the general structure of the line-of-sight velocity of the ejecta has already been studied. Furuzawa et al. (2009) and Hayato et al. (2010) measured the entire Doppler velocity structure of the ejecta including silicon, sulfur, argon, and calcium by *Suzaku*, but it had difficulties due to the poor spatial resolution of *Suzaku*. Sato & Hughes (2017b) and Williams et al. (2017) also did it for the silicon ejecta in the entire remnant and outstanding bright knots more precisely by the excellent spatial resolution of *Chandra*. Although it looks reliable in terms of the method, we found a critical trouble in the ACIS-I detector on board *Chandra* they used (see Chapter A). We adopt another observatory *XMM-Newton*, and will measure the ejecta velocity over the whole of the remnant by a systematic method again.

7.1 Observation history of Tycho's SNR

Thirty-two years on the earth before the supernova of the progenitor system of Kepler's SNR, another bright supernova had occurred on November 11, 1572, also in our galaxy. The remnant of this explosion is named G120.1+1.4 (or 3C 10), but also called "Tycho's SNR" because of the contribution to the historical record by Tycho Brahe (1546–1601) (Brahe & Kepler, 1602). Before the detection of the remnant (Hanbury Brown & Hazard, 1952), this SN had been known as type Ia (Baade, 1945), and multi wavelength observations of this SNR reconfirmed it.

The radio observations between the 1980s and 1990s measured the expansion ratio of the synchrotron rim and suggested this remnant is still in the ejecta dominant phase

(Reynoso et al., 1997), as is natural for such young SNRs. Although this is consistent with the results of the X-ray observations that we have detected mainly emissions from the ejecta (e.g., Hwang & Gotthelf, 1997; Decourchelle et al., 2001; Hwang et al., 2002), it is a little mysterious that we have not detected any X-ray emissions from the heated environment including CSM and ISM so far. Dust emission observed in the infrared energy band revealed the shocked ambient media around the north-east quarter (Douvion et al., 2001), and strong correlation with Hα emission suggests efficient cosmic-ray acceleration occurs there (Lee et al., 2010). In contrast to such interactions with the environment, Williams et al. (2013) estimates the ISM density $\sim$0.1–0.2 cm^{-3} with concluding the consistency of such low density with no X-ray emissions from them. This low density value is also supported by other observations (Cassam-Chenaï et al., 2007; Katsuda et al., 2010). These results, with no existence of candidates for the counterpart of the progenitor system (Kerzendorf et al., 2013), have supported the DD-like origin of Tycho's SNR without any dense CSM.

7.2 Observations and analysis

Table 7.1: Observation list of Tycho's SNR by *XMM-Newton*.

Observation ID	Start Date	Duration (sec)	GTI-1 (sec)	GTI-2 (sec)	Note
0310590101	2005.07.03	33406	23437	24057	
0310590201	2005.08.05	31882	20112	21615	
0412380101	2006.07.28	31883	23008	21408	
0412380201	2007.08.21	36911	31544	31857	
0511180101	2007.12.30	29117	16680	17335	
0511180201	2008.01.01	51907	42117	32469	not used in this study
0511180301	2008.01.03	26917	0	0	not used in this study
0412380301	2008.08.08	46540	38264	39055	
0412380401	2009.08.14	34312	32814	32812	
total		322875	373998		only effective observations

From 2005 to 2009, *XMM-Newton* observed Tycho's SNR nine times for the aim of calibration (Table 7.1 and Figure 7.1). EPIC-MOS can observe the entire remnant by only single CCD chip, which can be confirmed in the event count maps (Figure 7.1). Although Tycho's SNR is so young that we can observe the yearly expansion by *Chandra*'s great angular resolution (cf., 0.14 arcsec yr^{-1} in Katsuda et al., 2010), its variation is almost ignorable in four years for *XMM*'s images. In these nine observations, two of them are not used in this analysis. Three observations entering the new year of 2008 (`0511180101`–`0511180301`) are for non-routine calibration and done in a special way. Although the observation `0511180101` is in the same condition as other ones, `0511180201` includes strong emission lines from energy calibration sources equipped with MOS, 5.9 keV from ^{55}Fe for example. `0511180301` did not include any photon events from Tycho's SNR, on the ohter hand. After excluding them, the total duration time is ∼323 ksec. After reprocess in the similar way to Kepler analysis, the total GTI is ∼374 ksec. The background observations are also listed in Table 7.2.

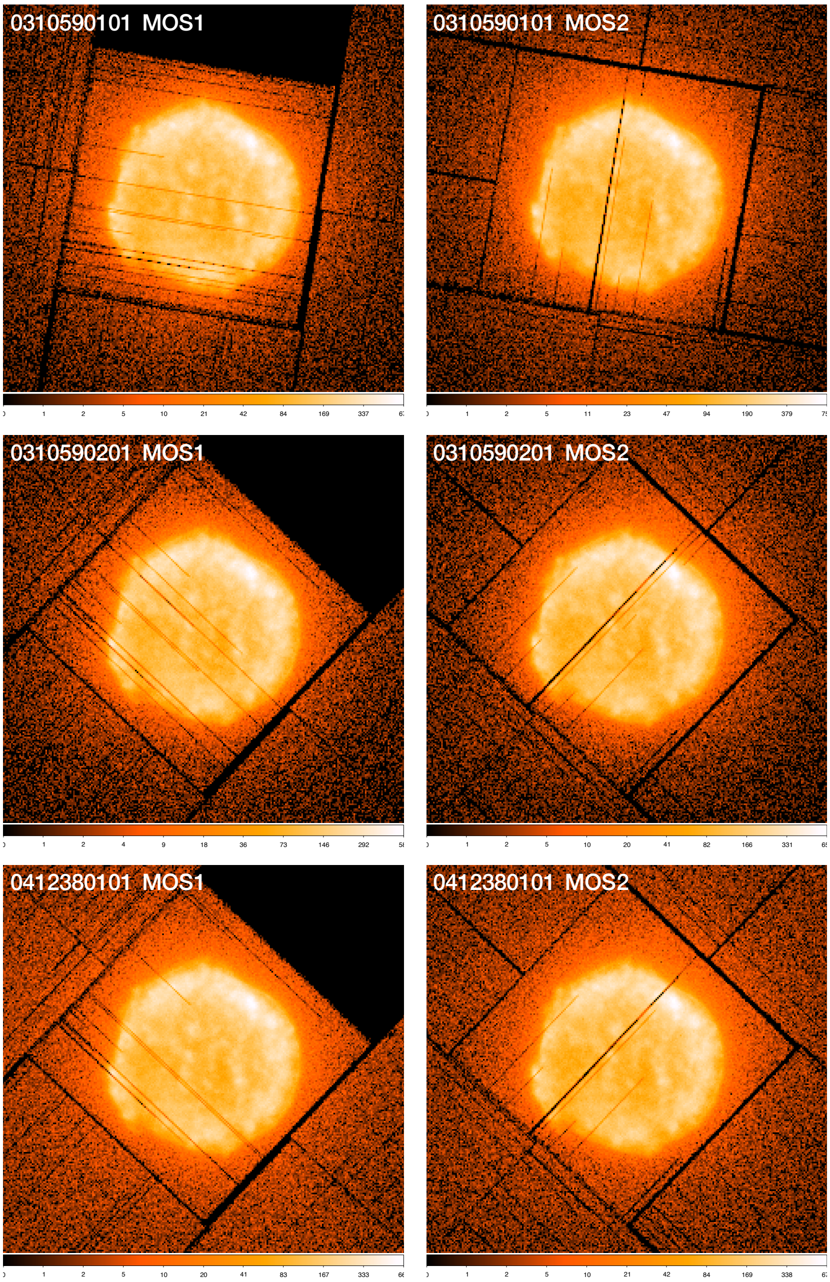

Figure 7.1: Same as Figure 4.1 but for Tycho's SNR.

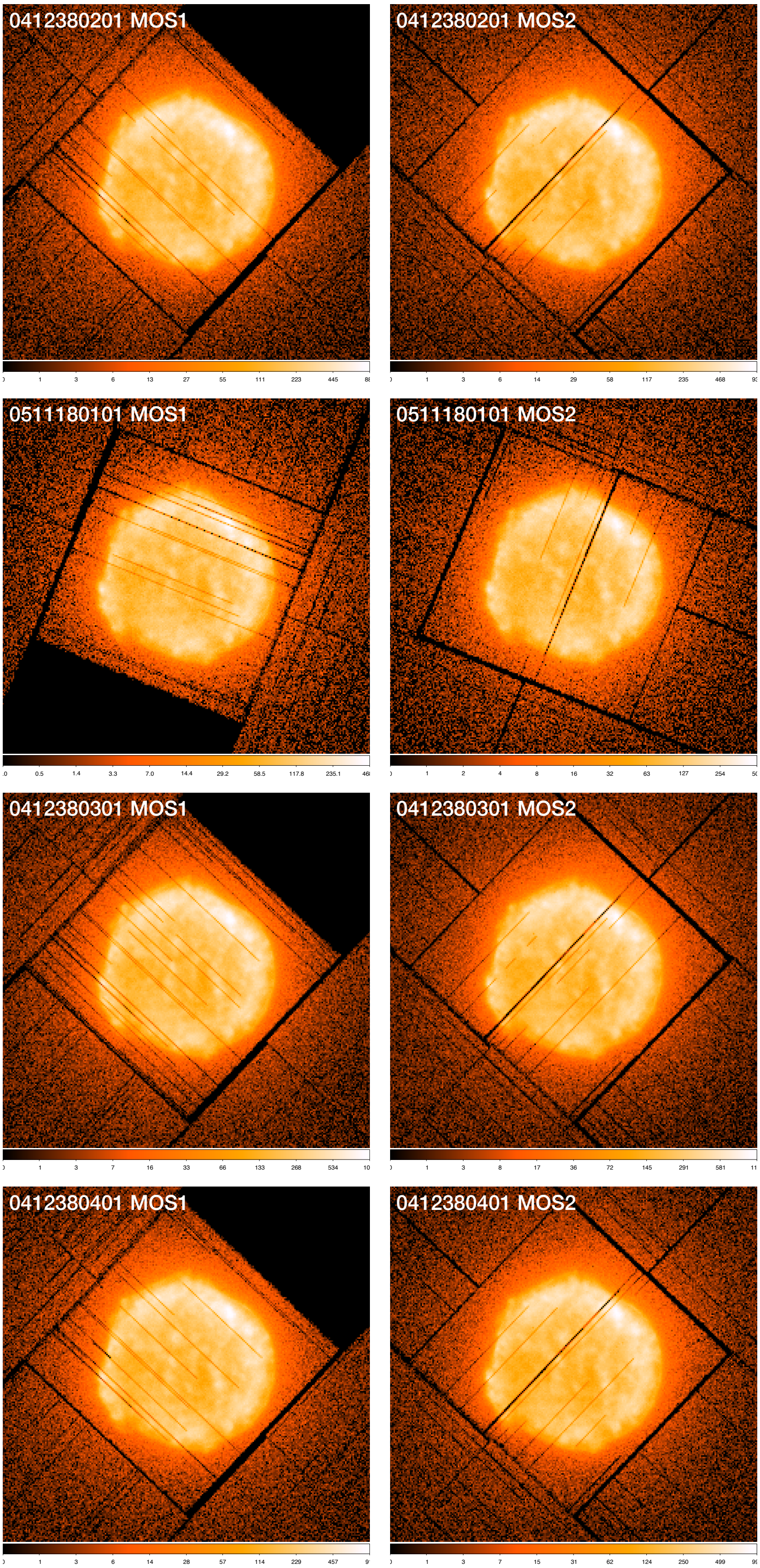

Figure 7.1: (continued)

Table 7.2: Background observation list of Tycho's SNR by *XMM-Newton*.

Target	Observation ID	Start Date	Duration (sec)	GTI-1 (sec)	GTI-2 (sec)
SWCX-1	0402530201	2006.06.04	96610	83846	85437
IGR00234+6141	0501230201	2007.07.10	26856	24105	24266
4U0115+63	0505280101	2007.07.21	31512	13680	14460
4U0241+61	0503690101	2008.02.28	118370	34557	35220
WD 0127+581	0555880101	2008.09.03	30916	24527	25620
total			365466	365718	

Figure 7.2 is the spectrum from the entire remnant as a product of such processes. We can see outstanding emission lines from the ejecta including silicon, sulfur, argon, calcium, and iron. Note that the emissions from oxygen, neon, and magnesium are also thought to come from the ejecta. We also plot the background spectrum in the same figure, whose strength is ~1 % in almost all the energy band.

We divide Tycho's SNR into grids whose size is 15 arcsec, making 34×34 sky pixels. Figures 7.3 shows all sky pixels on the flux images in each energy band observed by *Chandra* (the observation list is shown in Table A.1). The emission models are almost same as the analysis of Kepler's SNR, but only the CSM component is excluded due to the absence of evidence of its emission. The ISM absorption parameter is fixed to 7.5×10^{21} cm^{-2} in all regions. This value is derived from the average of previous works specialized small regions (Yamaguchi et al., 2017; Okuno et al., 2020).

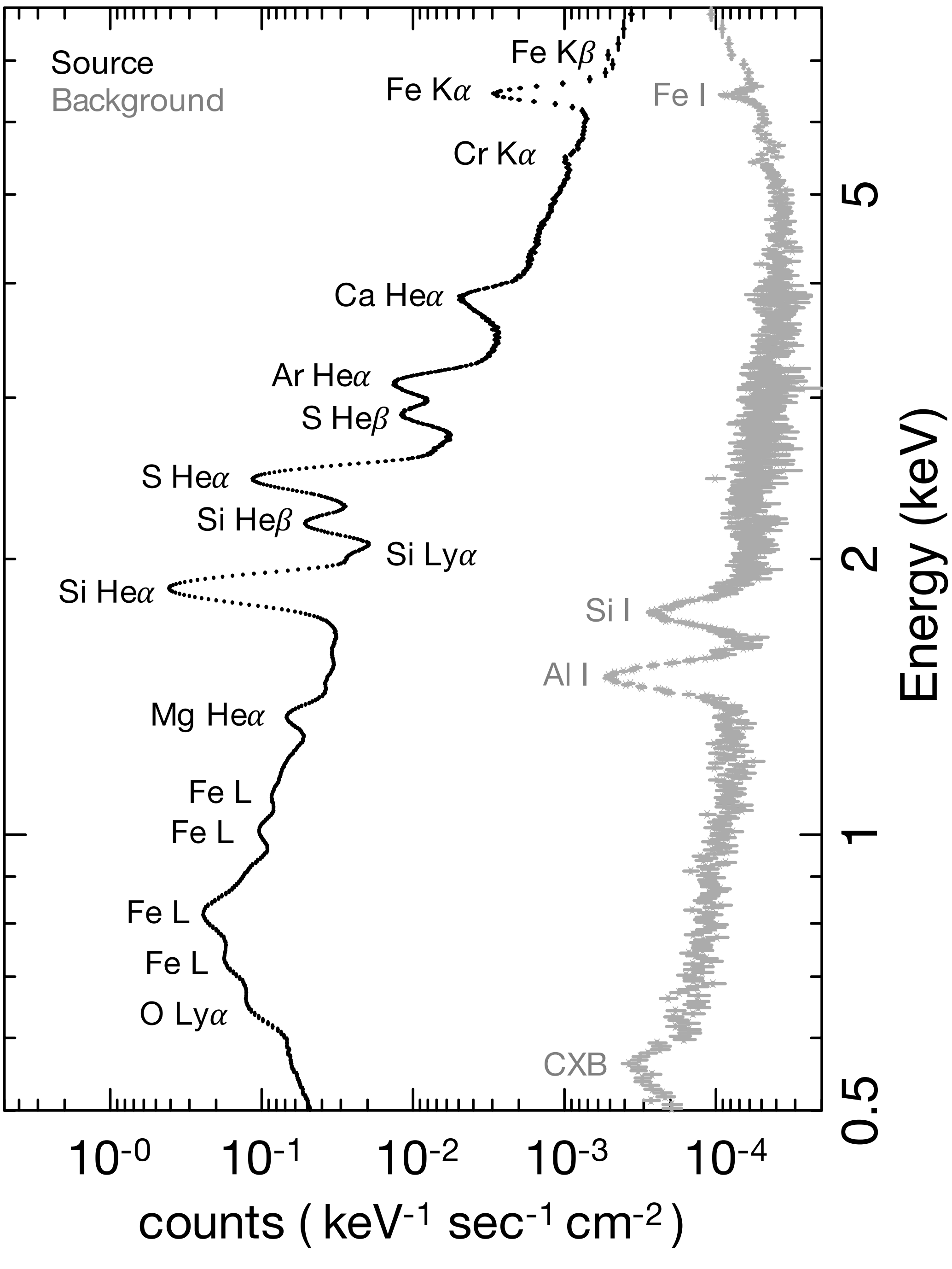

Figure 7.2: Same as Figure 4.2 but for Tycho's SNR.

Full band (0.5–8.0 keV)

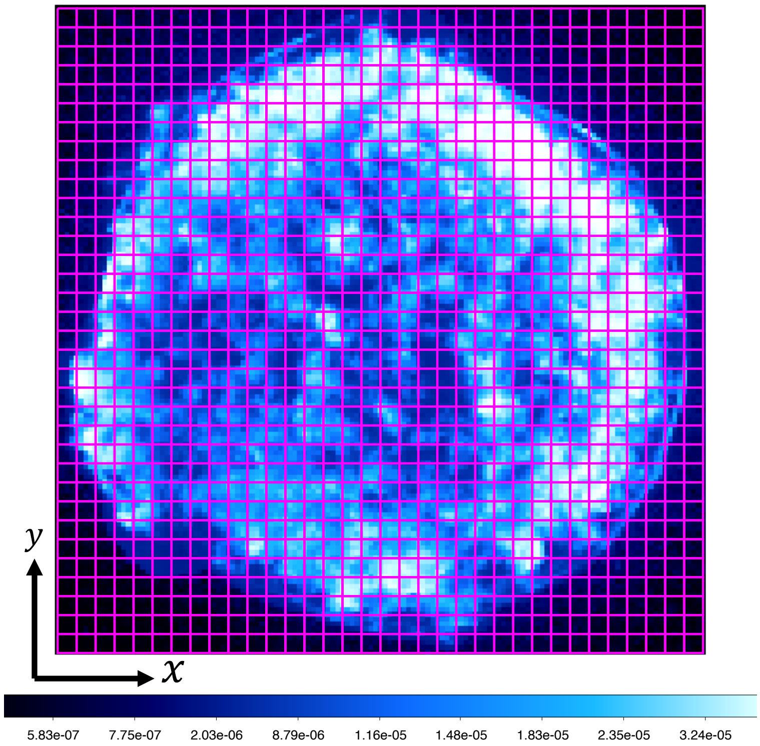

Continuum (4.1–6.1 keV)

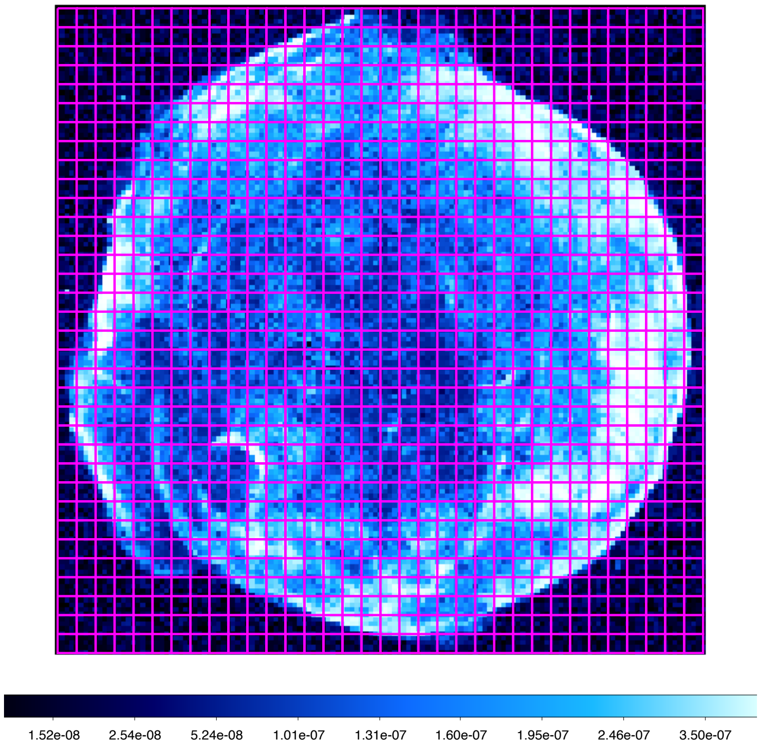

Figure 7.3: Same as Figure 4.3 but for Tycho's SNR.

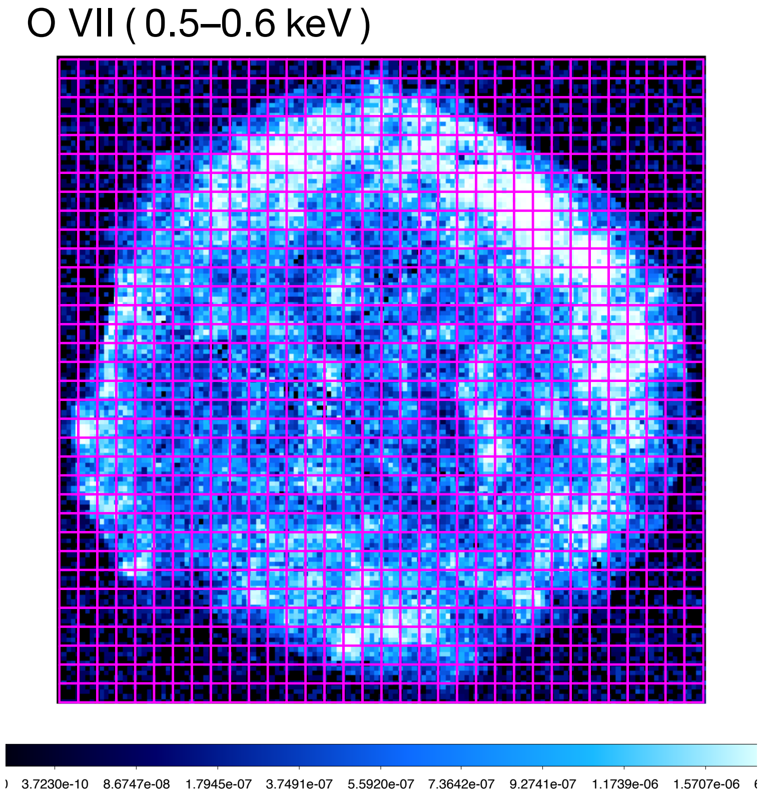

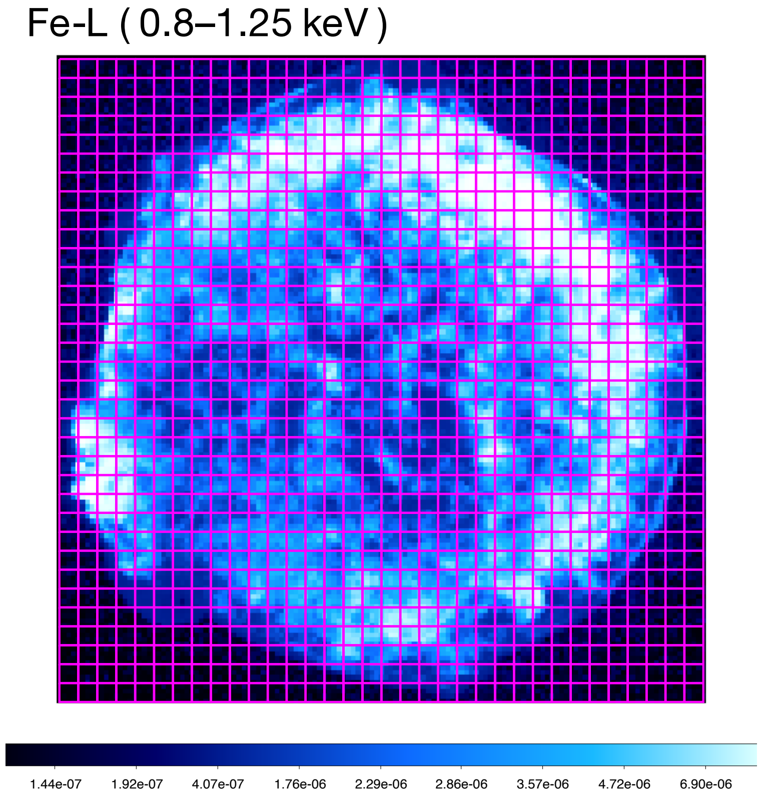

Figure 7.3: `(continued)`

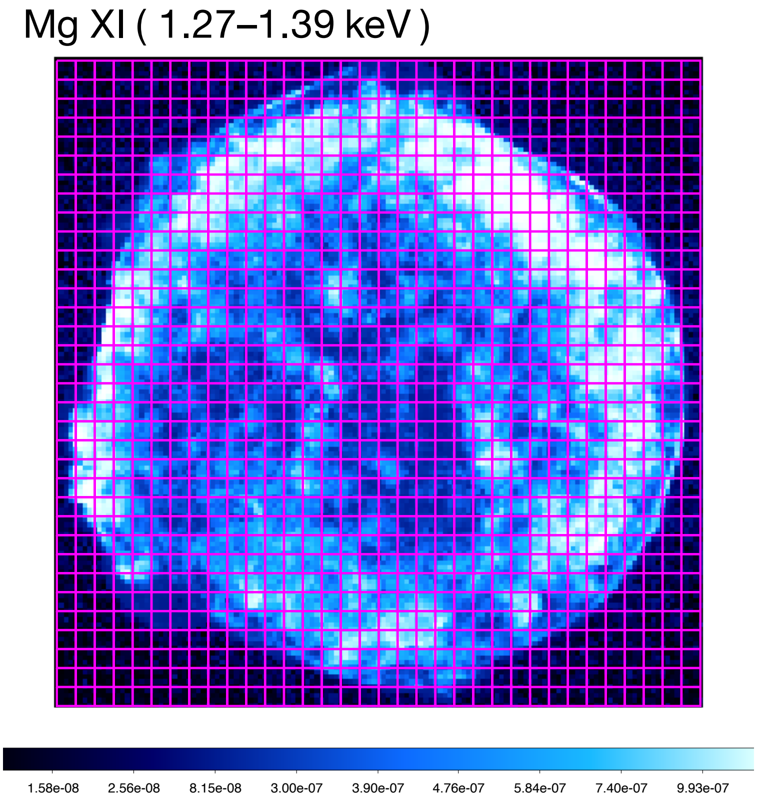
Mg XI (1.27–1.39 keV)

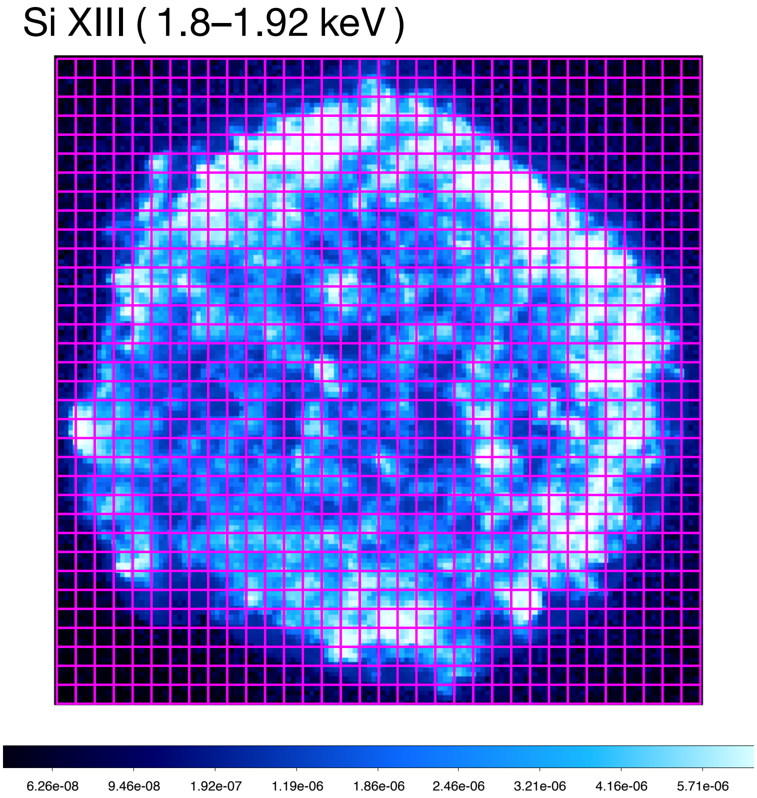
Si XIII (1.8–1.92 keV)

Figure 7.3: `(continued)`

S XV (2.4–2.52 keV)

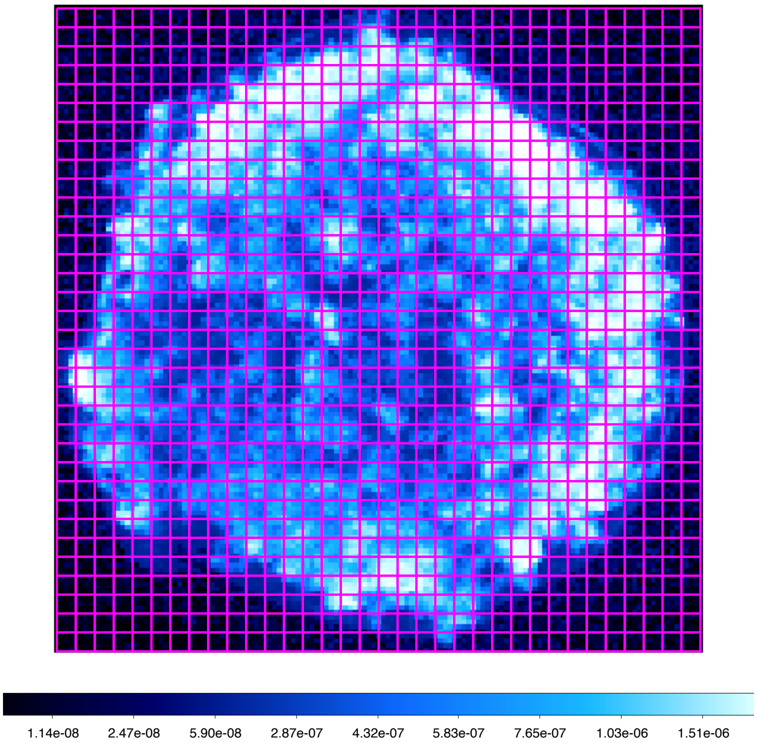

Ar XVII (3.07–3.18 keV)

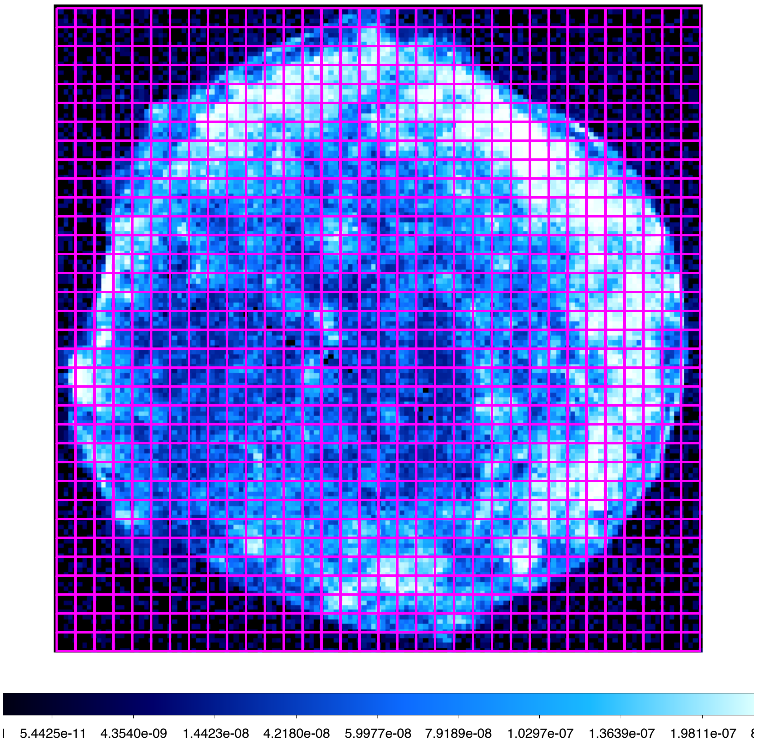

Figure 7.3: `(continued)`

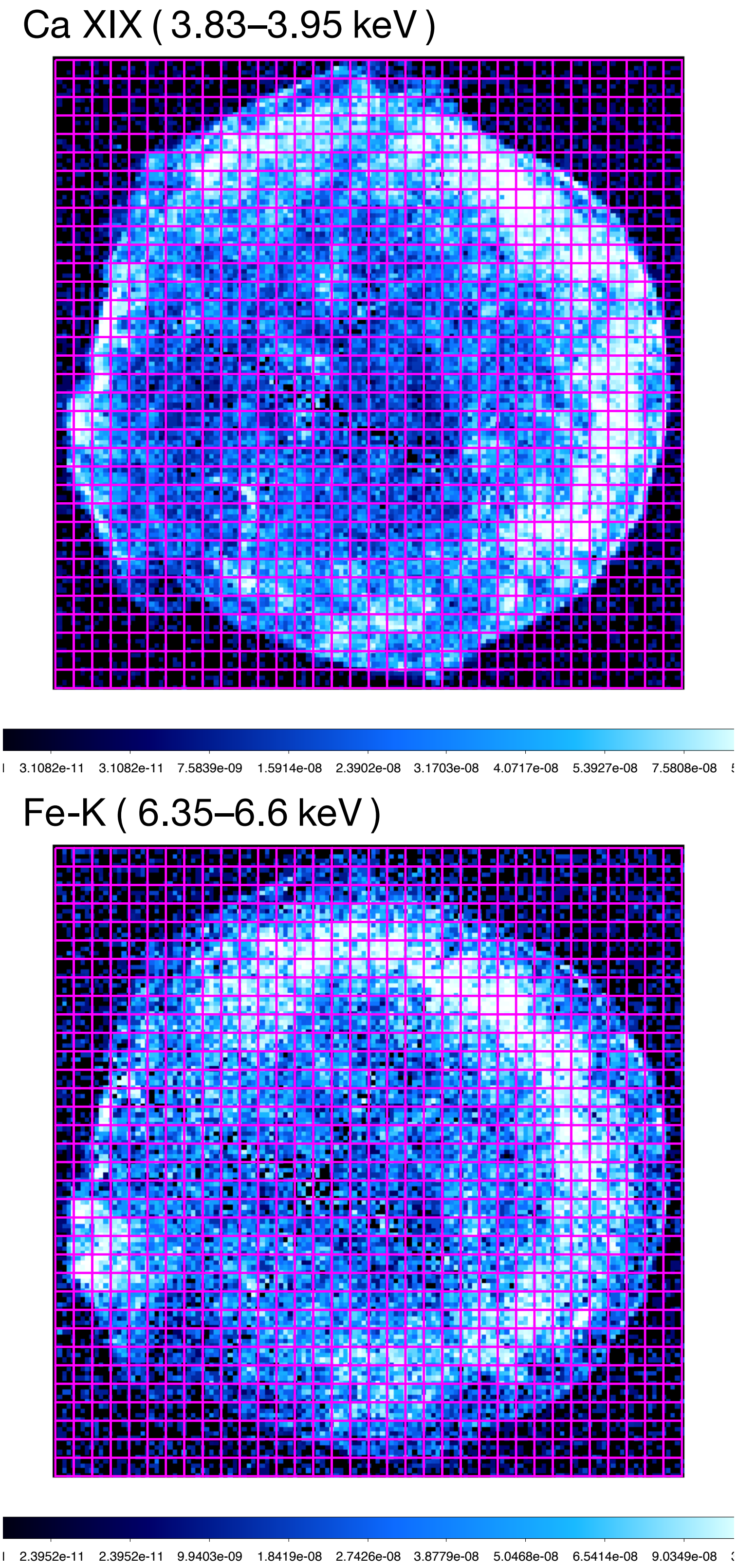

Figure 7.3: `(continued)`

7.3 Results

During all of the spectral analysis, the distribution of the W-stat is generally converged to the DOF value, 1471, of each fitting (Figure 7.4). Figure 7.5 shows spectral fitting results in all sky pixels in Tycho's SNR. We again succeed phenomenologically in representing the observed spectrum in all pixels with almost no strong residuals remaining there.

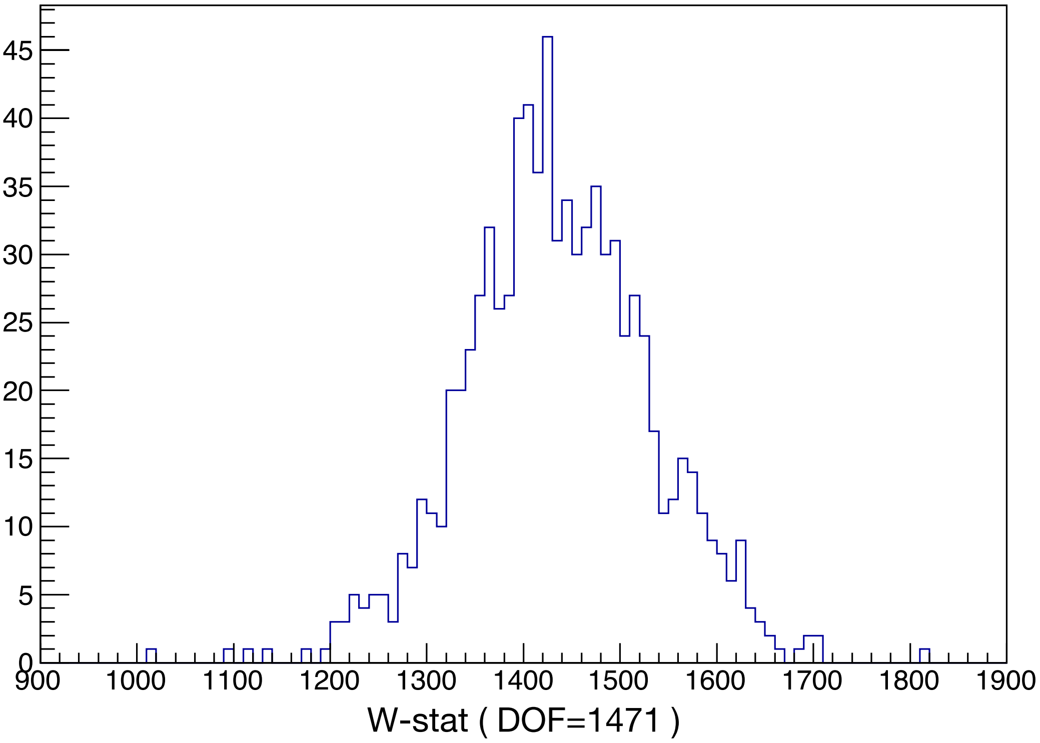

Figure 7.4: Same as Figure 4.5 but for Figure 7.5.

In our Kepler analysis, we show Doppler parameter maps with their estimated errors. Here we show again the similar maps for Doppler parameters in this Tycho analysis. In addition to them, because all thermal emissions come from the ejecta in Tycho's SNR, we can trust other thermal fitting parameters more without the uncertainties of the fixed parameters of the CSM component in the previous Kepler analysis. We show them in the form of the best-fit value maps for such other fitting parameters in the following subsections.

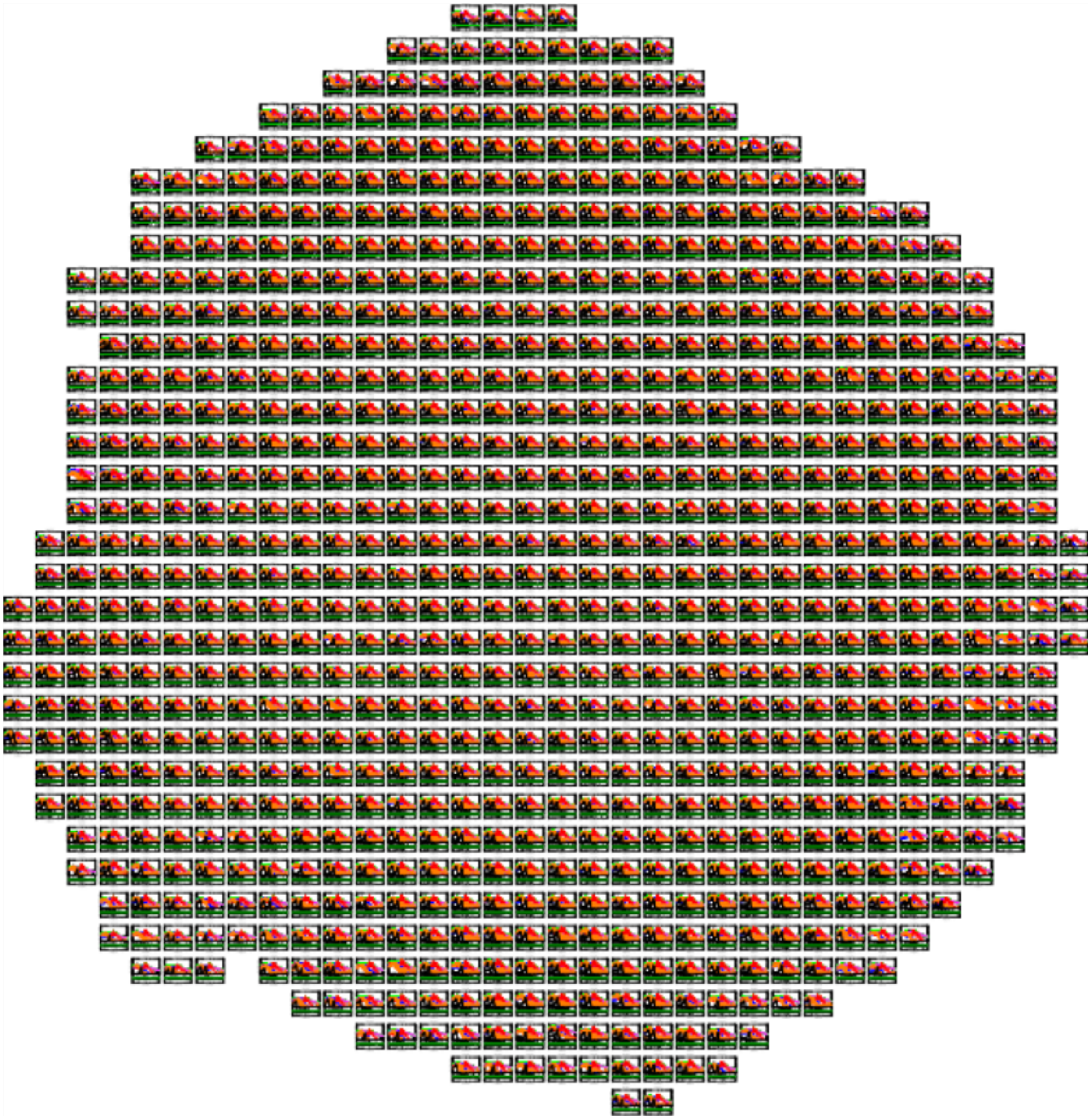

Figure 7.5: Spectral fitting results of Tycho's SNR. Full resolution data is available as electronic media.

7.3.1 Photon index of power-law component

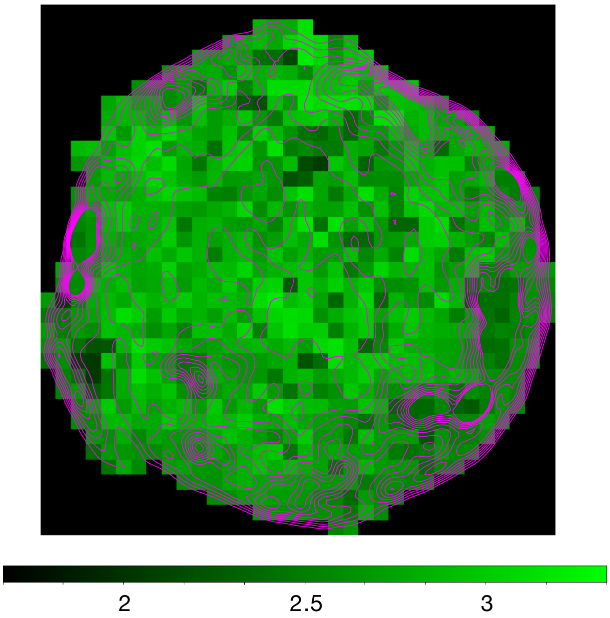

Figure 7.6: Photon index map of Tycho's SNR on a linear scale. Contour represents the flux of the non-thermal emission in Figure 7.3.

First, we verify the photon index Γ of the `PL` component, which is represented as $\propto E^{-\Gamma}$. This value is ~2 for the synchrotron emission and gets larger for thermalized emissions. As we can see in Figures 7.3 and 7.5, the entire region of Tycho's SNR is dominated by the thermal emissions. However, we can read photon index values near 2 in regions where strong non-thermal emission is observed, for example in the south-west edge in Figure 7.6. We regard that this result ensures the validity of our analysis. In other regions, Γ gets close to or over 3, which means the thermal emissions are dominant there.

7.3.2 Electron temperature

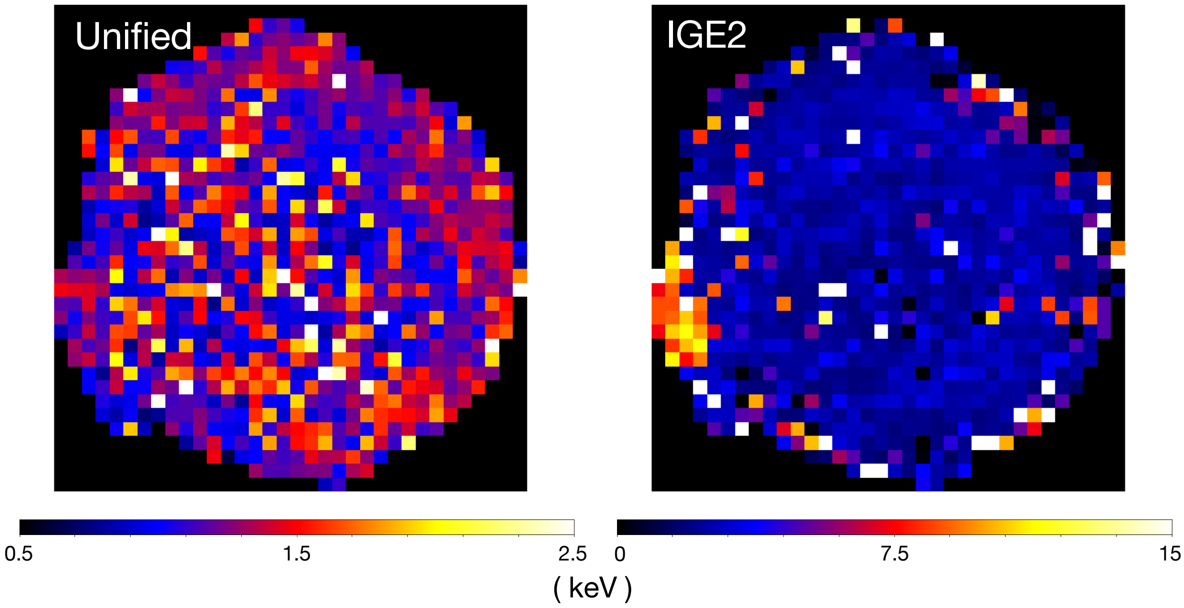

Figure 7.7: Electron temperature maps of Tycho's SNR on a linear scale.

The electron temperature is assumed as same in all of the components except for the second IGE component, which mainly represents Fe-K emission. Its unified temperature results between 0.5 to 2.5 keV (the left map in Figure 7.7). We will discuss these results in §8.4.3 in detail.

Here, we refer to the high electron temperature of the second IGE component at the south-east edge, which is called the Fe-knot (Yamaguchi et al., 2017). The electron temperature here is >7.5 keV and it is three times higher than the averaged value of the entire region ∼2.5 keV. In terms of the spectral fitting results, this difference is originated from the contribution of two IGE components. Results around there in Figure 7.5 show the all emission lines from the iron are explainable by single IGE component. In addition, they tell us that such an IGE component needs higher electron temperature, whereas the first IGE component, whose temperature is unified to other components like IME, cannot play that role. This result shows the origin of the iron there is different from that in the other regions. Yamaguchi et al. (2017) indicated that the origin there is synthesized under the incomplete Si burning or the α-rich freeze-out with a relatively low neutron excess. In contrast to normal location of the synthesis of IGEs, such mechanisms suggest they are originated from the distant position from the core of the WD. Our results indicate such difference as the fractions of the contribution of two different IGE components. Indeed, the fitting results in Yamaguchi et al. (2017) at the Fe-knot explained the entire spectrum by single and highly heated IGE component, whose electron temperature is ∼8 keV.

7.3.3 Ionization timescale

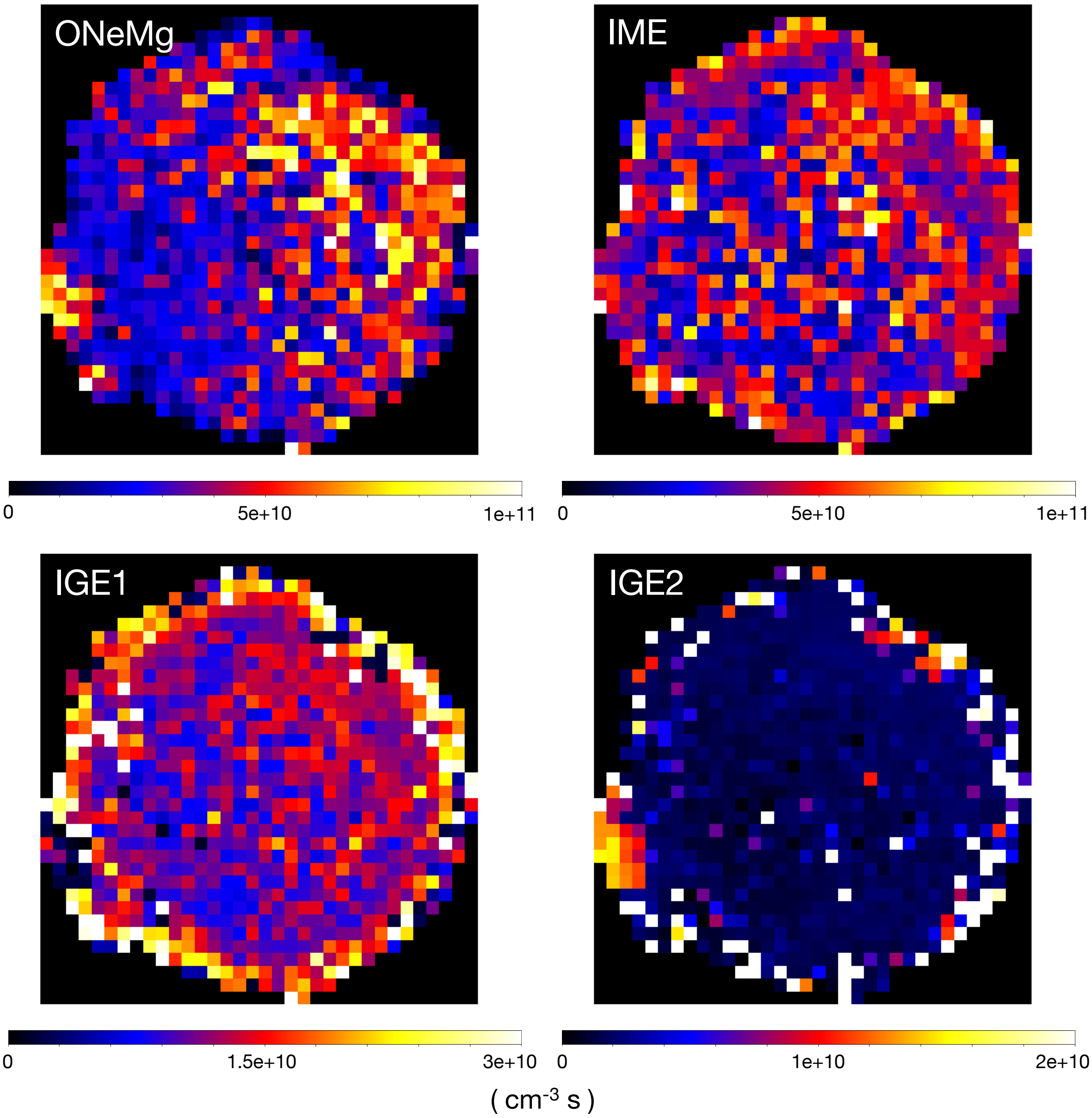

Figure 7.8: Ionization timescale maps of Tycho's SNR on a linear scale.

The ionization timescale is the product of the electron density by the elapsed time after being shocked. The upper limit of the time parameter can be estimated as the comparable value of the SNR age $\sim 1.4 \times 10^{10}$ sec. Our results are fitted in the range of ±1 order from $\sim 1.4 \times 10^{10}$ cm^{-3} sec, except for the results of the second IGE component at the edge, where the Fe-K emission is weak and could easily mis-estimate the true value. This is reasonable assuming that the electron density is a little larger than the typical value in ISM ~0.1–1 cm^{-3}. For IGE components, these values are smaller than the other elements because the reverse shock has shocked them more recently. Detailed discussions are skipped to §8.4.3.

Here similarly, the result of the second IGE component at the south-east edge represents that of the entire IGE component of the Fe-knot spectrum. Our result $\sim 1 \times 10^{10}$ cm^{-3} sec is consistent with the previous result in Yamaguchi et al. (2017). This value is more than twice larger than that in the other regions, but close to that of the first IGE component. These results indicate that the ionization timescale of Fe-L is generally $> 1 \times 10^{10}$ cm^{-3} sec and the Fe-K emission is more highly ionized than Ne-like only at the Fe-knot.

7.3.4 Abundance ratio

Figure 7.9 shows the abundance ratio of S/Si, Ar/Si, Ca/Si, and Ti/Fe derived from the `vvnei` models. For the IME elements, the ratio maps seem uniform generally. However, S/Si and Ar/Si around the south-east edge, i.e. the Fe-knot, is a little higher than those in the other regions. Even though the origin of iron here is different from that in other regions, the mass of sulfur and argon gets close to that of silicon at the boundary between the iron and silicon layer (cf., Iwamoto et al., 1999). This effect will result in such high abundance ratio there. Note that the mass ratio Ca/Si would also be higher for the same reason. Such tendency is weak in our result. It may be because the difficulty of estimating the calcium abundance due to the coupling of the absorption parameter and the emissivity of Ca-L lines located between 0.5–0.6 keV. In this energy band, the emission lines of O VII, Fe-L, Ca-L, and the silicon-escaped component of S-K emissions, which are the artifact lines due to the detector response, are contaminated, although the energy resolution of CCD detectors cannot resolve any line feature clearly there. We regard the Ca/Si ratio as less reliable than the other IME components.

Concerning the remaining result, the titanium abundance is linked to those of chromium and manganese. Because these emission lines are faint, the result of Ti/Fe is less reliable than those of IMEs. It seems the ratio is higher around the center of the remnant. Note that the ratio at Fe-knot seems small or covered by fluctuations, where Yamaguchi et al. (2017) found no strong emission from chromium, manganese, and nickel.

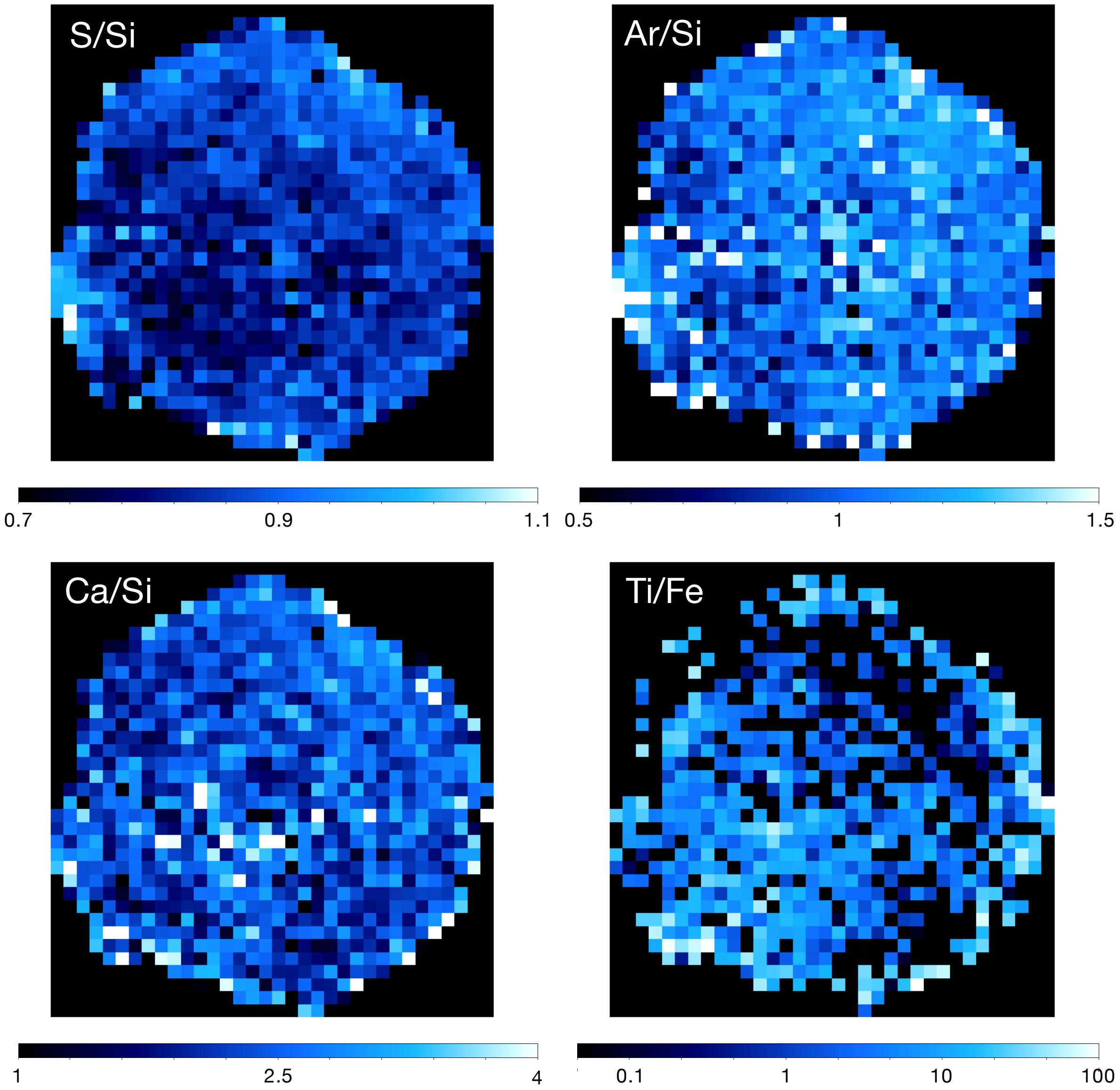

Figure 7.9: Abundance ratio maps of Tycho's SNR. Only the Ti/Fe ratio is shown on a logarithmic scale, while the others are on a linear scale.

7.3.5 Doppler shift

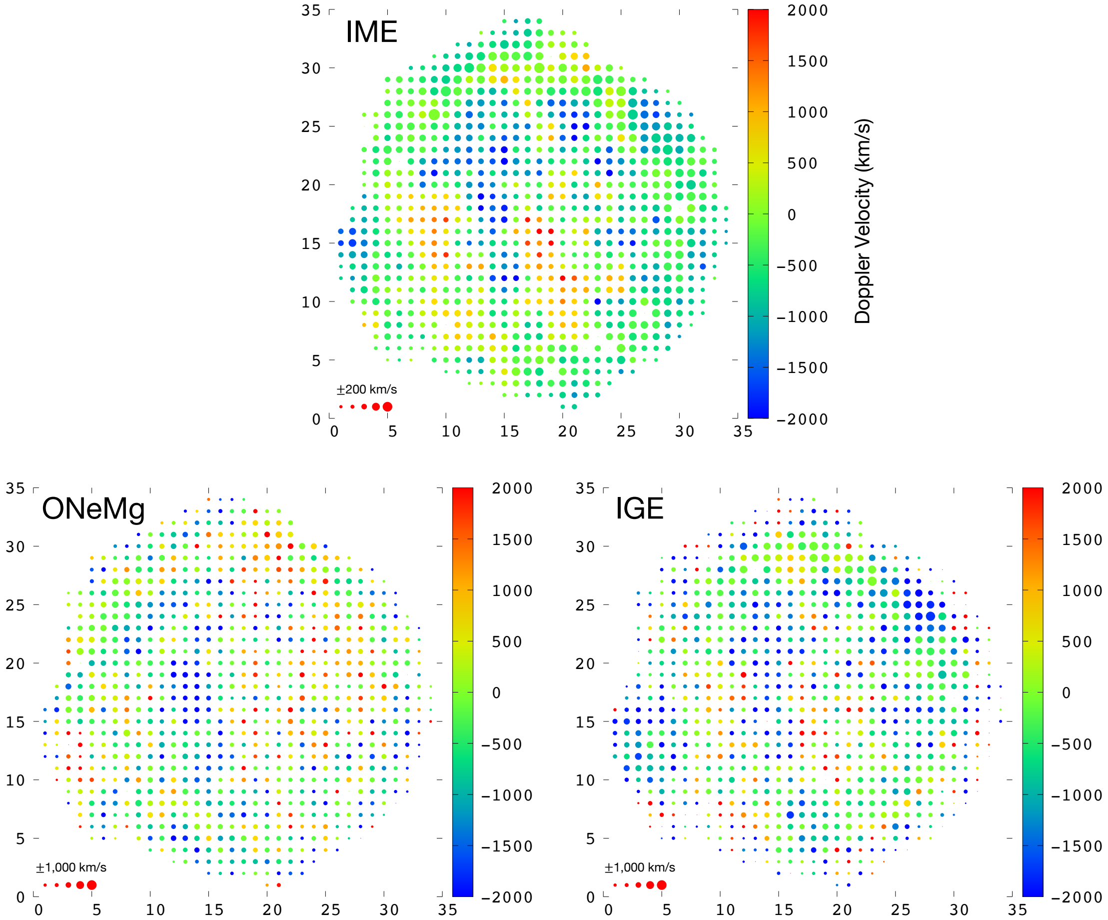

Figure 7.10: Same as Figure 4.7 but for Tycho.

Figure 7.10 shows the Doppler shift parameter maps of each ejecta component using the `vmshift` model. The shift map of IMEs is compared with the mean photon energy map of Si Heα (Figure 4 in Sato & Hughes (2017b)). Sato & Hughes (2017b) plotted the mean value of the incident photon energy of detected events in the Si-Kα band at each detector pixel of *Chandra*. We can regard this mean value as the line centroid of Si-Kα because the Si emission is so strong that the emission shape looks like a simple Gaussian. Considering almost all elements except for IGEs are ionized to the He-like state even in young SNRs, we can also estimate the line centroid at the static state. Combining these general facts, it is reasonable to understand the trend of the Doppler shift of the silicon ejecta by using the mean photon energy map. Calculating from the map in Sato & Hughes (2017b) and the emission energy of Si Heα 1.865 keV (Table 2.1), the distribution of the Doppler shift of the silicon ejecta is ± 1 % in the light speed. This range is consistent with our result of IMEs in Figure 7.10. They also showed a spatial trend that the mean photon energies in the north half is higher than those in the south. Although their result could be miss-estimate the Doppler velocity because it is not necessary for the all silicon ejecta to be ionized to the He-like state, our analysis considering its ionization state also shows the similar trend. This trend gets to be supported more.

Concerning ONeMg and IGEs, these are the first plots of the Doppler shift maps for these ejecta elements, although their reliability is inferior to that of IMEs. For the ONeMg component, emission lines from them are not well resolved due to the worse energy resolution of CCD detectors or the contamination by Fe-L lines. For two IGE components, in addition to the similar situation for Fe-L lines, the uncertainty of the ionization state of the Fe-K line also affects the estimation of the Doppler shift. Considering them, the reliable points of these results is that both ejecta components also show the same trend to be blue-shifted in the north and red-shifted in the south at the center of the remnant.

7.3.6 Line width

Parameter maps of each ejecta

The width of the emission lines is the main indicator of the kinematics of the ejecta in our study. Figure 7.11 shows its results of each ejecta component using the `gsmooth` model. We can compare these line width maps with previous radial profiles by Hayato et al. (2010) and Sato & Hughes (2017b). Hayato et al. (2010), which is an advanced study of Furuzawa et al. (2009), analyzed the *Suzaku* spectrum between Si-Kα to Fe-Kα by dividing the remnant into four tori. They found the line width estimated by Gaussians representing emission lines gets narrower from the center to the edge in Tycho's SNR for all elements, while the line centroid keeps constant except for calcium. Sato & Hughes (2017b) analyzed *Chandra* spectrum in the same way and confirmed this result with a finer pitch. Note that both works excluded the south-east edge of the remnant.

While our result plays a role in the reconfirmation of them by another representative observatory *XMM-Newton*, its strong point is investigating it in 2-dimensions. Ignoring the fluctuations in the outer rims, the line width maps of IMEs and IGEs show the same trend as previous works. In addition to them, we also measure the line width of ONeMg, which is difficult to analyze by a Gaussian fitting method. While only ONeMg shows a large line width at the south-east edge due to missing outstanding lines from them, our results show the same trend that the line width gets narrower from the center to the edge is applicable to all elements.

Note that Sato & Hughes (2017b) showed the line width gets wider out of the radius at $\sim$3.4 arcmin (see Figure 2 in their paper). Even though they did not divide the azimuth angle, their result would depend on the north-west rim because the photon statistics there is dominant in all the energy bands. However, the line width tends to be larger than the real value there observed by *Chandra* ACIS-I as described in Chapter A. We trust our results by *XMM-Newton*, which indicates narrow line width even at the north-west rim.

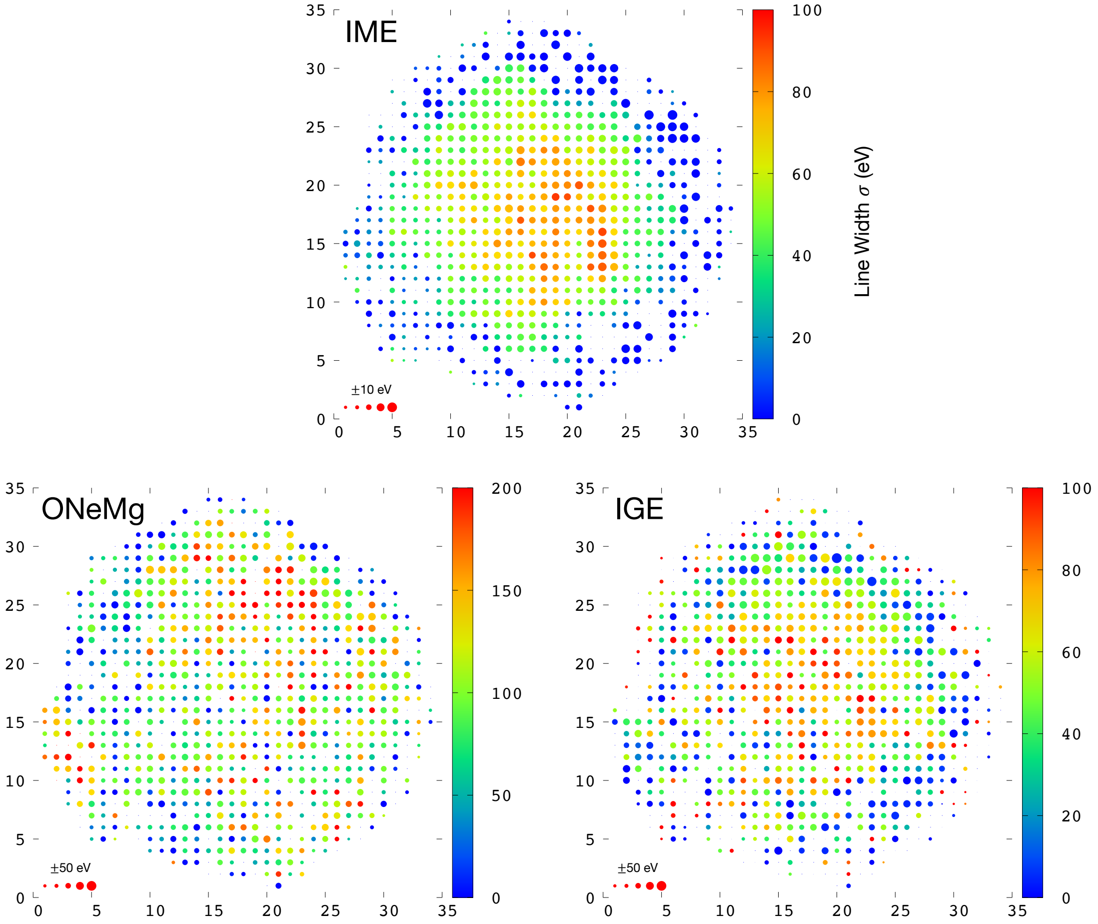

Figure 7.11: Same as Figure 4.8 but for Tycho.

Radial profiles of IME ejecta

Among three components of ONeMg, IMEs, and IGEs, the result of IME emission lines is the most reliable, because the line profile is clear and the ionization state can be assumed as He-like in all sky pixels. Hereafter, we focus only on the IME elements for a while.

Figure 7.12 is the radial profiles of the IME line width with dividing the remnant into 8 circular sectors. The azimuth angle is defined in the counter clock-wise direction from the north. Note that the sector whose angle is between 90–135 degrees include the Fe-knot located at the south-east edge. We find that the line width gets narrower from the center, and drop to ∼0 eV around the radius of ∼200 arcsec in almost all sectors. Then the line width keeps ∼0 eV to the edge of the remnant. This is an interesting result, because the line width should be decreased monotonically to the edge if the ejecta expands uniformly and isotropically. We need to investigate this in more detail.

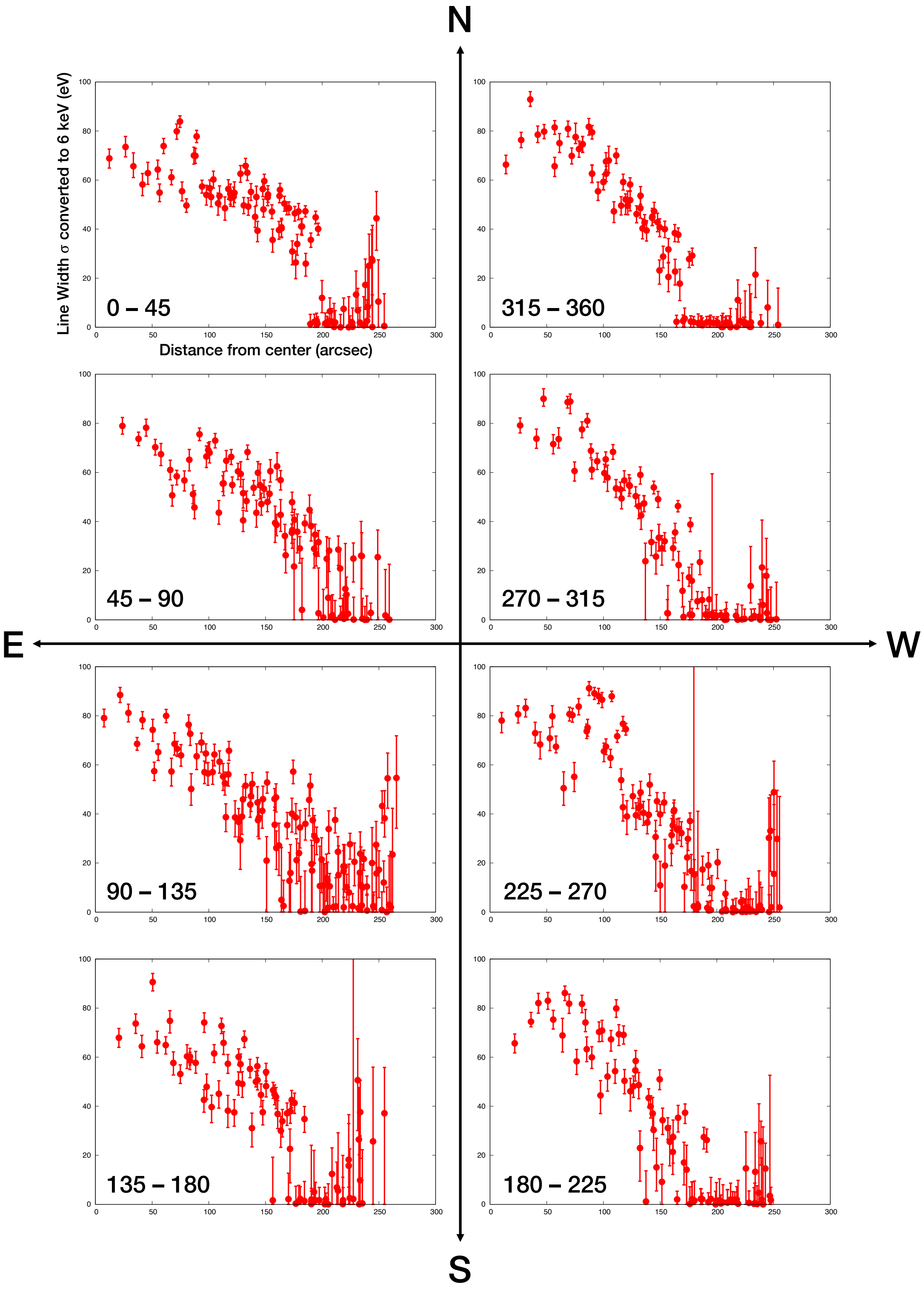

Figure 7.12: Same as Figure 4.9 but for Tycho.

7.4 Further analysis for IME ejecta

7.4.1 Spectral fitting

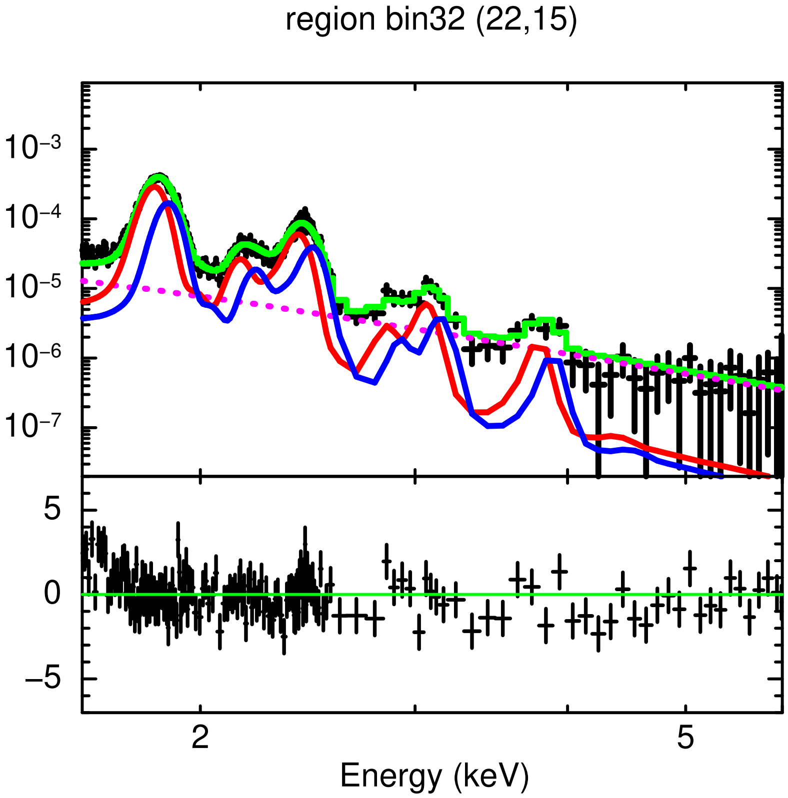

Figure 7.13: Same as Figure 4.4, but an example of the narrow-band spectral fitting. Here, the line color red and blue represents the Doppler-shifted direction of each IME component.

For further studies, we derive the expansion velocity quantitatively. As described in §2.4.2, the line width can be broadened by the line-of-sight velocity difference ($v_{\rm r} - v_{\rm b}$). Concentrating on it, which is twice of the expansion velocity $v_{\rm IME}$ in the line-of-sight direction, we introduce a two-velocity model for the IME component (cf., Hayato et al., 2010). Only choosing the narrow IME band in 1.6–6.0 keV, we adopt two NEI models for each velocity component and one `PL` as an phenomenological continuum component. Parameters of the NEI components, except for the normalization, velocity, and line width, are identical with each other and fixed to the best-fit values of the analysis in §7.2. The line width of each is set to be 0 eV assuming the line broadening effect by ($v_{\rm r} - v_{\rm b}$) is dominant. The velocity parameters are set as $v_{\rm r} = v_{\parallel} + v_0$ and $v_{\rm b} = -v_{\parallel} + v_0$ assuming the symmetrical expansion in each line-of-sight direction. The velocity offset v_0 is calculated as the average IME velocity at the edge of the remnant. We estimate v_0 is -420 km sec^{-1} by using our result in Figure 7.10. Although this offset velocity could be due to the bulk motion of Tycho's SNR or its original WD, this also could be explainable by the uncertainty of the energy accuracy in MOS detectors. The latest calibration documentation of MOS reported the uncertainty is 5 eV in all the energy band (XMM-Newton Calibration Technical Note 0018, Version 3.12, 2019), and it is converted to ~800 km sec^{-1} at the Si-Kα band. We cannot distinguish these two effects.

7.4.2 Results

Fitting statistics and results are shown in Figures 7.14 and 7.15. These fittings looks again successful. We show the radial profiles of $v_{\|}$ in Figure 7.16. Similar to the line width parameter in §7.3.6, $v_{\|}$ gets lower from the center to the edge generally. Based on these results, we will discuss the dynamics of Tycho's SNR in the next chapter.

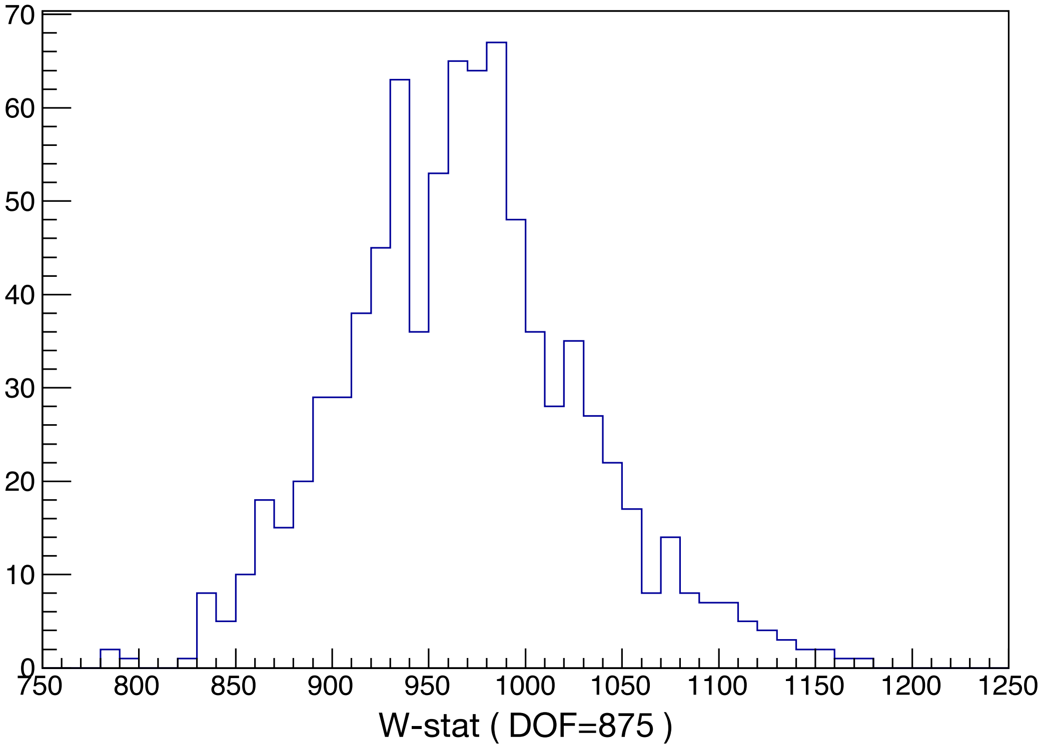

Figure 7.14: Histogram of w-stat values.

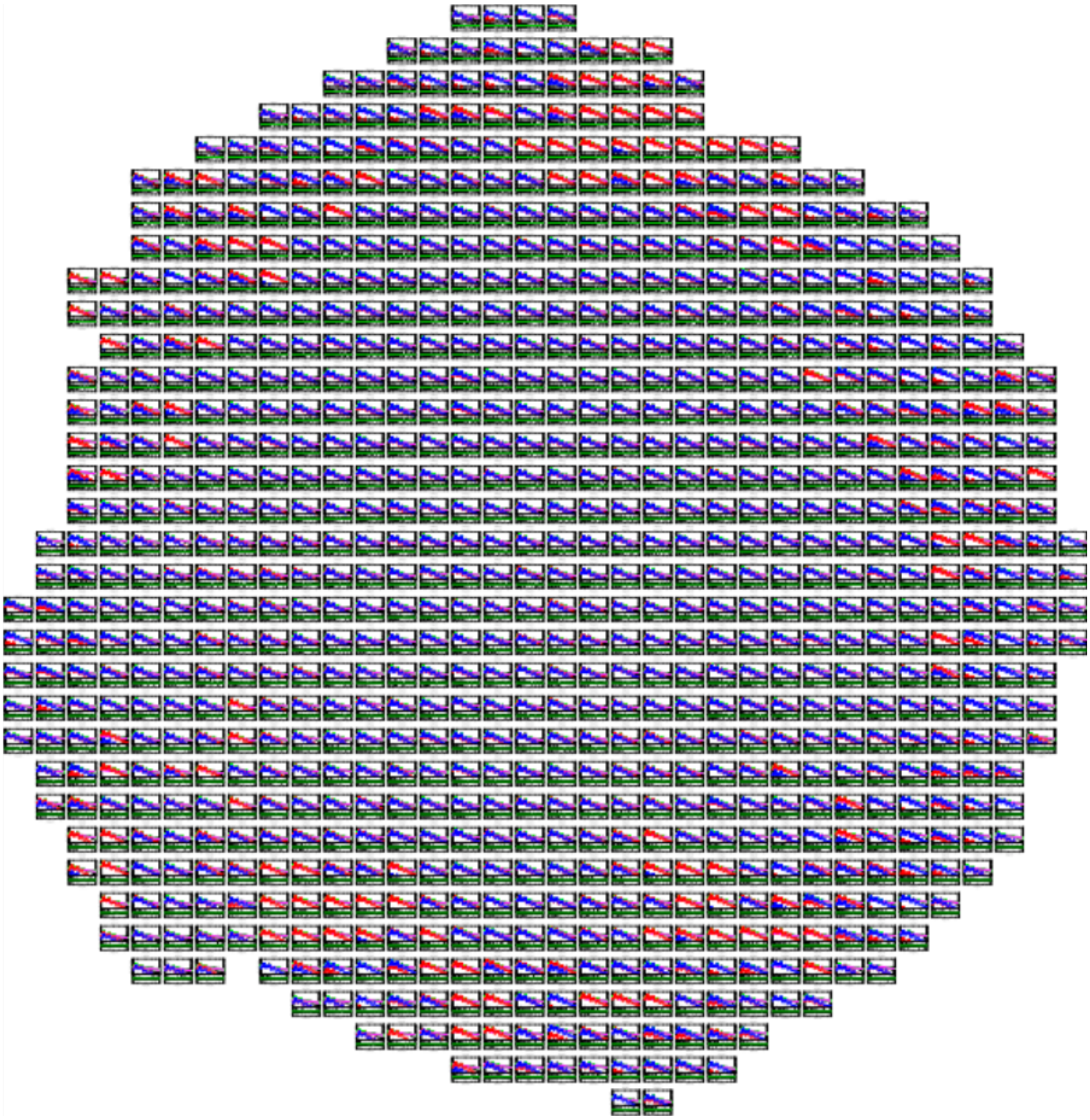

Figure 7.15: Spectral fitting results of Tycho's SNR. Full resolution data is available as electronic media.

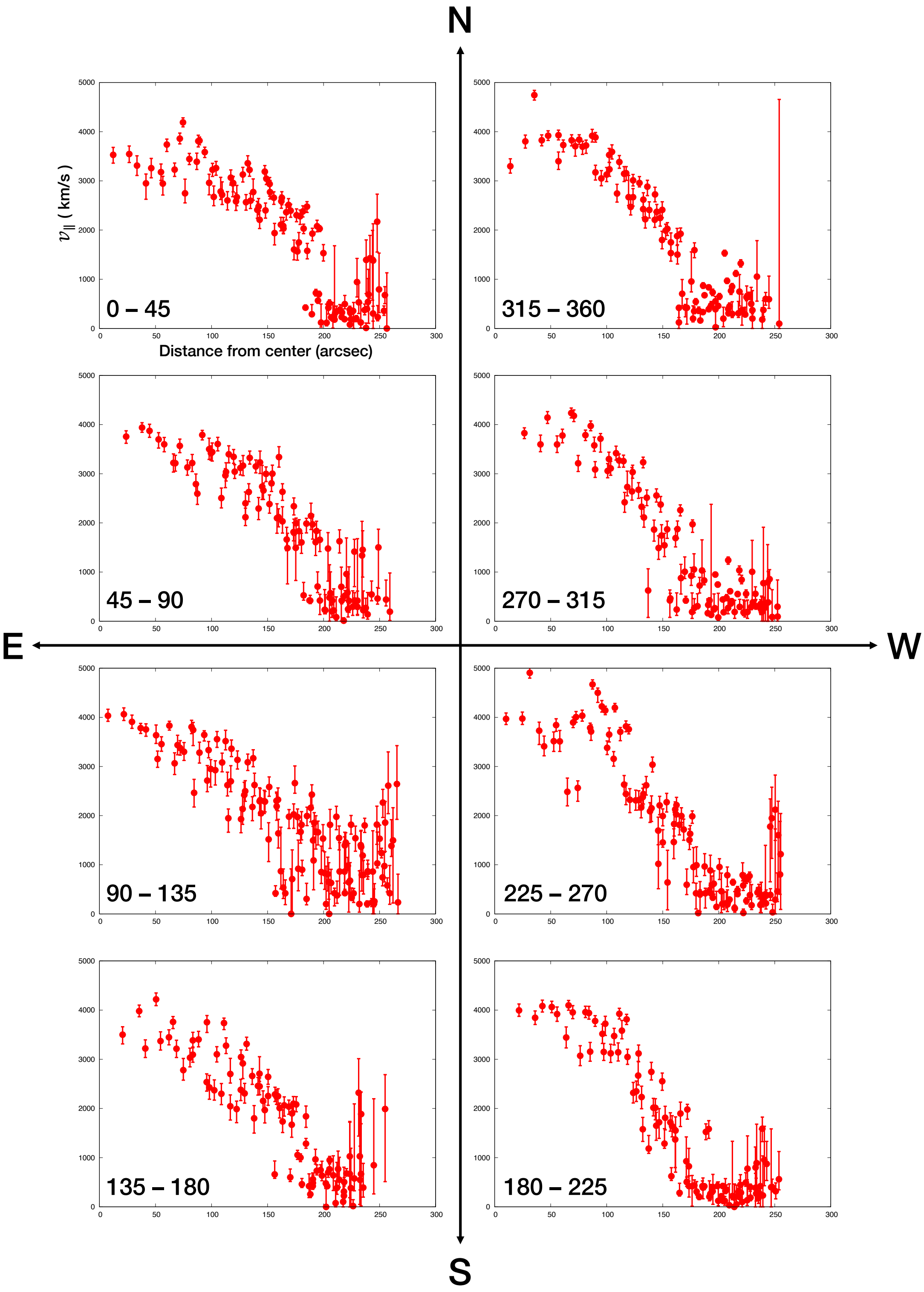

Figure 7.16: Similar to Figure 7.12, but the radial profiles of $v_{\|}$ at each sky pixel.

Chapter 8

Dynamics of Tycho's supernova remnant

8.1 Expansion in uniform and isotropic ISM

At first, we will interpret the radial profiles of the expansion velocity of IME ejecta (Figure 7.16) by assuming a uniform and isotropic environment with low density around the remnant, which is a reasonable assumption for the ISM. In such an environment, the heated ejecta results in expanding with keeping its velocity constant (Figure 2.1). We derive the projection effect from the 3-dimensional velocity $v_{\rm IME}$ to the line-of-sight velocity $v_{\parallel}$ with representing this velocity picture by the following steps.

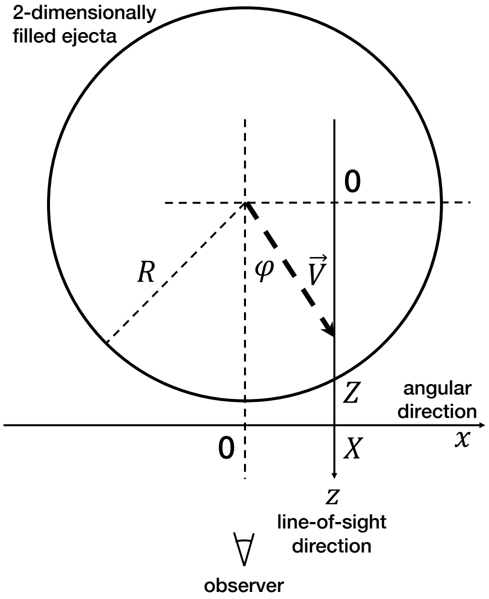

Figure 8.1: Schematic drawing of filled ejecta in a cutting plane of the angular direction. Definitions are written in the main text.

We focus on a 2-dimensional plane which is a cutting plane of the angular direction of the 3-dimensional remnant. At first, we assume ejecta groups are filled in the full of the plane (Figure 8.1). The expansion velocity of each ejecta is V and the outermost radius is R. We choose the z axis in the line-of-sight direction, which is orthogonally crossed at coordinate X on the angular axis x. The Z coordinate at the intersection between the z axis and the circumference of the ejecta group is defined as $Z \equiv \sqrt{R^2 - X^2}$. Between 0 and Z on z axis, the line-of-sight velocity of one ejecta element, whose location is described as $\vec{V}$, is $v_\parallel = V \cos\varphi$, where φ is the angle between $\vec{V}$ and z axis. Here, the integration of the line-of-sight velocity $v_\parallel$ of each ejecta element at X is calculated as:

$$f(X; R) = \int_{y=0}^{Y} \mathrm{d}y \; V \cos\varphi \ . \tag{8.1}$$

Defining $\Theta \equiv \arcsin{(X/R)}$ and using a relationship $y = X \tan{(\frac{\pi}{2} - \varphi)} = X / \tan\varphi$, this equation can be resolved as:

$$\begin{aligned} f(X; R) &= \int_{\varphi=\pi/2}^{\Theta} \mathrm{d}\varphi \; \frac{\mathrm{d}}{\mathrm{d}\varphi} \left(\frac{X}{\tan\varphi} \right) V \cos\varphi \\ &= \int_{\varphi=\pi/2}^{\Theta} \mathrm{d}\varphi \; \left(-\frac{X}{\sin^2\varphi} \right) V \cos\varphi \\ &= VX \left[\frac{1}{\sin\varphi} \right]_{\varphi=\pi/2}^{\Theta} \\ &= V(R - X) \ . \end{aligned} \tag{8.2}$$

Observed line-of-sight velocity $F_1(x; R)$ is the density averaged value of the velocity integration $f(x; R)$. Assuming the ejecta density is uniform, $F_1(x; R)$ is calculated as:

$$F_1(x; R) = \frac{f(x; R)}{\sqrt{R^2 - x^2}} = V \sqrt{\frac{R - x}{R + x}} \ . \tag{8.3}$$

Next, we assume the spherical expanding ejecta which are distributed from $R = R_1$ to $R = R_2$ where $R_1 < R_2$. In the hollow situation at $x < R_1$, the line-of-sight velocity $F_2(x; R_1, R_2)$ is the density averaged value of the difference of the velocity integration $(f(x; R_2) - f(x; R_1))$, as:

$$\begin{aligned} F_2(x; R_1, R_2) &= \frac{f(x; R_2) - f(x; R_1)}{\sqrt{R_2^2 - x^2} - \sqrt{R_1^2 - x^2}} \\ &= V \frac{\sqrt{R_1^2 - x^2} + \sqrt{R_2^2 - x^2}}{R_1 + R_2} \\ &= V \left(\frac{R_1}{R_1 + R_2} \sqrt{1 - \left(\frac{x}{R_1} \right)^2} + \frac{R_2}{R_1 + R_2} \sqrt{1 - \left(\frac{x}{R_2} \right)^2} \right) \ . \end{aligned} \tag{8.4}$$

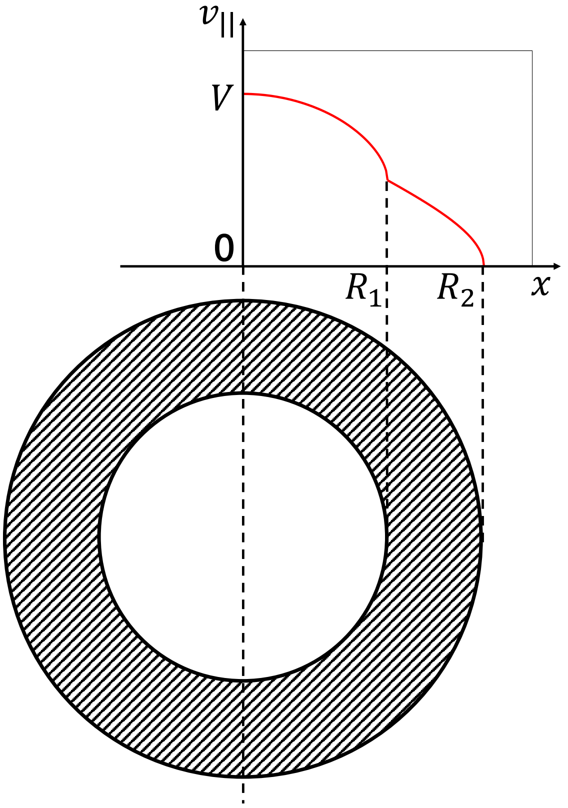

Figure 8.2: Schematic drawing of hollow ejecta in a cutting plane of the angular direction. Definitions are written in the main text. We also plot an example of the velocity profile written in Equation 8.7 above this figure.

It is obvious that the mathematical continuity at $x = R_1$ is satisfied as:

$$F_1(R_1; R_2) = F_2(R_1; R_1, R_2) = V\sqrt{\frac{R_2 - R_1}{R_2 + R_1}} \; . \tag{8.5}$$

If the ejecta distributes like a shell, whose radius is R, the radial profile performs as a cosine function:

$$F_2(x; R, R) = V\sqrt{1 - \left(\frac{x}{R}\right)^2} \; . \tag{8.6}$$

Concluding them, the line-of-sight velocity $v_\parallel$ as a function of the angular distance x is calculated as:

$$v_\parallel(r) = \begin{cases} V\left(\dfrac{R_1}{R_1 + R_2}\sqrt{1 - \left(\dfrac{x}{R_1}\right)^2} + \dfrac{R_2}{R_1 + R_2}\sqrt{1 - \left(\dfrac{x}{R_2}\right)^2}\right) & \text{if } 0 \le x < R_1 \quad , \\ V\sqrt{\dfrac{R_2 - R_1}{R_2 + R_1}} & \text{if } R_1 \le r < R_2 \quad , \\ 0 & \text{if } R_2 \le x \quad . \end{cases} \tag{8.7}$$

8.2 Estimation of 3-dimensional velocity of IME ejecta

Converting into the physical parameters, the line-of-sight velocity $v_\parallel$ as a function of the angular distance x is calculated as:

$$v_\parallel(x) =$$

$$\begin{cases} v_\mathrm{IME}\left(\dfrac{r_\mathrm{RS}}{r_\mathrm{RS}+r_\mathrm{IME}}\sqrt{1-\left(\dfrac{x}{r_\mathrm{RS}}\right)^2}+\dfrac{r_\mathrm{IME}}{r_\mathrm{RS}+r_\mathrm{IME}}\sqrt{1-\left(\dfrac{x}{r_\mathrm{IME}}\right)^2}\right) & \text{if } 0 \le x < r_\mathrm{RS} \quad , \\ v_\mathrm{IME}\sqrt{\dfrac{r_\mathrm{IME}-x}{r_\mathrm{IME}+x}} & \text{if } r_\mathrm{RS} \le x < r_\mathrm{IME} \quad , \\ 0 & \text{if } r_\mathrm{IME} \le x \quad , \end{cases} \tag{8.8}$$

where the radius of the reverse shock and the distance to the edge of the IME ejecta are r_RS and r_IME, respectively.

The projecting effect $v_\parallel(x)/v_\mathrm{IME}$ can be calculated using observable parameters by the following methods. r_IME is the distance to the observed edge of the IME ejecta. It is called Contact Discontinuity (CD) (cf., Truelove & McKee, 1999), whose position r_CD it may be difficult to distinguish from that of the forward shock by our spatial resolution. We measure r_CD using the averaged value of the distance to the outermost sky pixels in each sector. r_RS has been already studied in previous works. Warren et al. (2005) used *Chandra* observation data and determined r_RS comparing the Fe-Kα emission peak in almost all the azimuth angle except for the south-east. They estimated that r_RS was ∼183 arcsec. Because the Fe-Kβ emission is more sensitive to the heating by the reverse shock, Yamaguchi et al. (2014a) adopted the Fe-Kβ emission image as the more certain indicator of r_RS in the north-west direction observed by *Suzaku*, whose sensitivity around such an energy band is more reliable than that of *Chandra*. Their result of r_RS was ∼158 arcsec. We adopt the averaged value of them, so r_RS is assumed to be 170.5 arcsec.

Using these r_IME and r_RS, we calculate v_IME using our result in Figure 7.16 and the relationship in Equation 8.8. Figure 8.3 shows its result. Although v_IME is expected to be constant from the center to the edge (Figure 2.1), our result shows a two-velocity structure in almost all circular sectors. In the sector between 0–45 degree for example, the velocity of the inner ejecta is ∼3,500 km sec^{-1} while the outer ejecta shows ∼1,000 km sec^{-1}. The higher and lower velocity components are fit in the range of ±500 km sec^{-1} in the all sectors, except for one including the Fe knot, where we expect a different expansion structure.

Such velocity structure can be easily interpreted as a deceleration of the 3-dimensional velocity. It means our simple assumption fails to represent the observed expansion structure of the IME ejecta in Tycho's SNR. Instead of it, this deceleration suggests the interaction with denser materials (Figure 2.2).

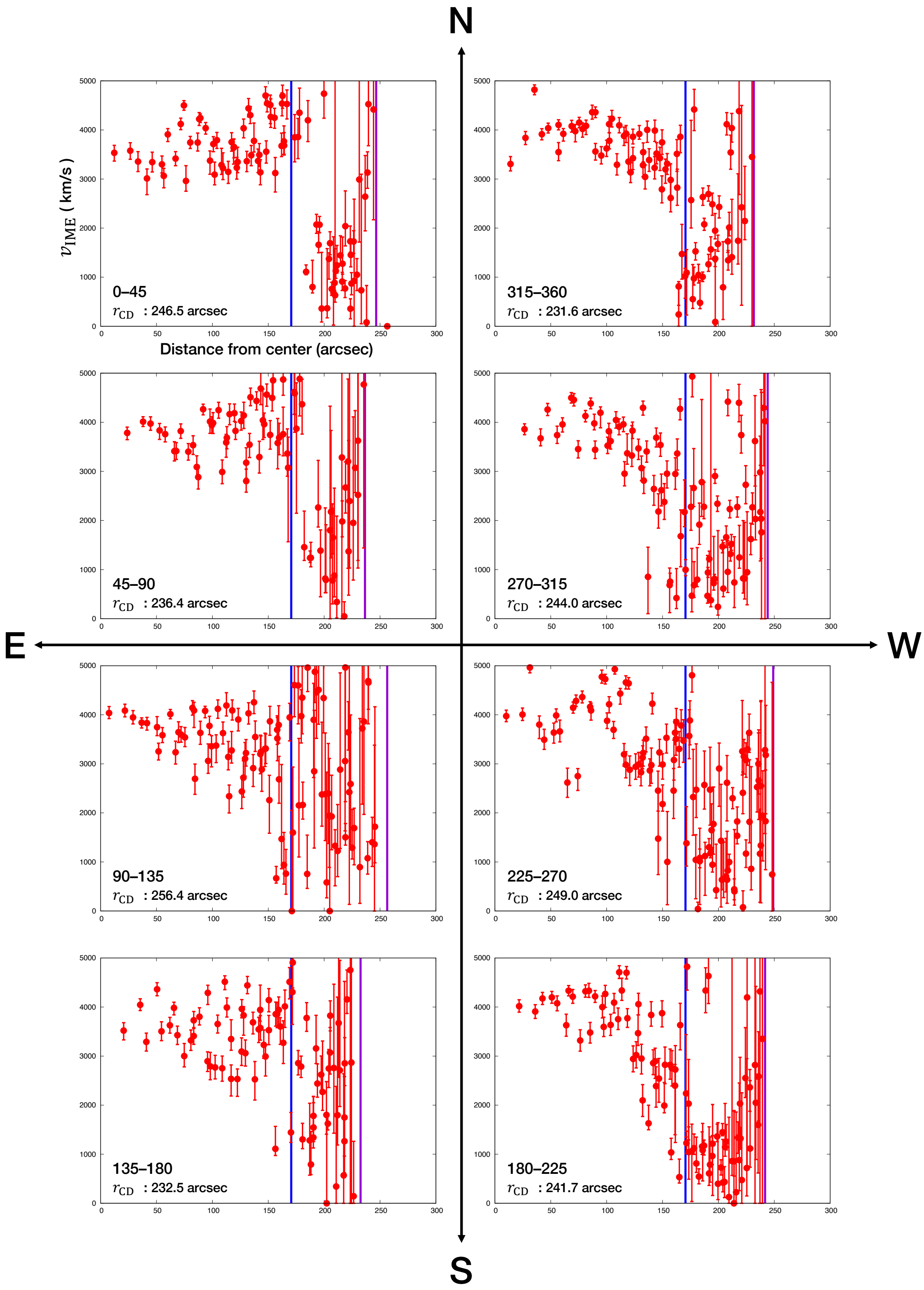

Figure 8.3: Similar to Figure 7.16, but radial profiles of the estimated v_{IME} at each data point by assuming the uniform and isotropic expansion. Used parameters are shown at a lower-left corner in each plot. We also plot assumed r_{RS} (blue) and r_{IME} (violet). Note that the plotting limit of v_{IME} is set to be 5,000 km sec^{-1} for easy comparison with Figure 7.16.

Before interpreting this result as a deceleration, we add some supplementary explanations. Our result is based on the two NEI model fitting in §7.4. It is reasonable for the hollow emission structure, where we can divide the red- and blue-shifted components. While this structure is valid in the range of $0 \leq x < r_{\mathrm{RS}}$, the outer region in $r_{\mathrm{RS}} \leq x < r_{\mathrm{IME}}$ is filled in the line-of-sight direction. Both shifted components are distributed sequentially, so it is skeptical that we can sufficiently explain there by our assumption. Instead, we need to adopt single NEI model to explain there. We have already done it in §7.3.6. Although the single line width is difficult to convert into the quantitative line-of-sight velocity, Figure 7.12 shows that the line width is ∼0 eV in the outer region. The fitting parameter 0 eV means our observed line broadening of the raw spectrum is sufficiently explained by the energy resolution of MOS detectors. Therefore, we should interpret our results of the two NEI fitting in the outer region are rather the upper limit than the best-fit value. In terms of this point, the two velocity structure in Figure 8.3 is valid at least.

Another point we want to mention is that the outermost data points get higher velocity, even though the estimated error also gets larger. This could be due to the weak line strength to the continuum emission, which is called the equivalent width, at the edge of the SNR. The synchrotron emission at the forward shock front is dominated and the ejecta emission should be weak because the emission volume is thin in the line-of-sight direction. Our analysis aims to mainly explain the ejecta dominant region, and we need to care to fit such spectra with small equivalent width because the line shape tends to be broaden to explain the continuum.

8.3 Expansion parameters of IME ejecta

Based on admitting the two-velocity structure, we again get back to the original velocity profile (Figure 7.16). We fit them using Equation 8.8 by the Levenberg-Marquardt method (Levenberg, 1944; Marquardt, 1963), which is a derived type of a least-squares method considering error bars. The best-fit value v_{IME}, r_{RS}, and r_{IME} will represent the higher velocity, the position of the reverse shock, and the position of the reflected shock, respectively. Figure 8.4 and 8.5 show the best-fit model and parameter list in each circular sector.

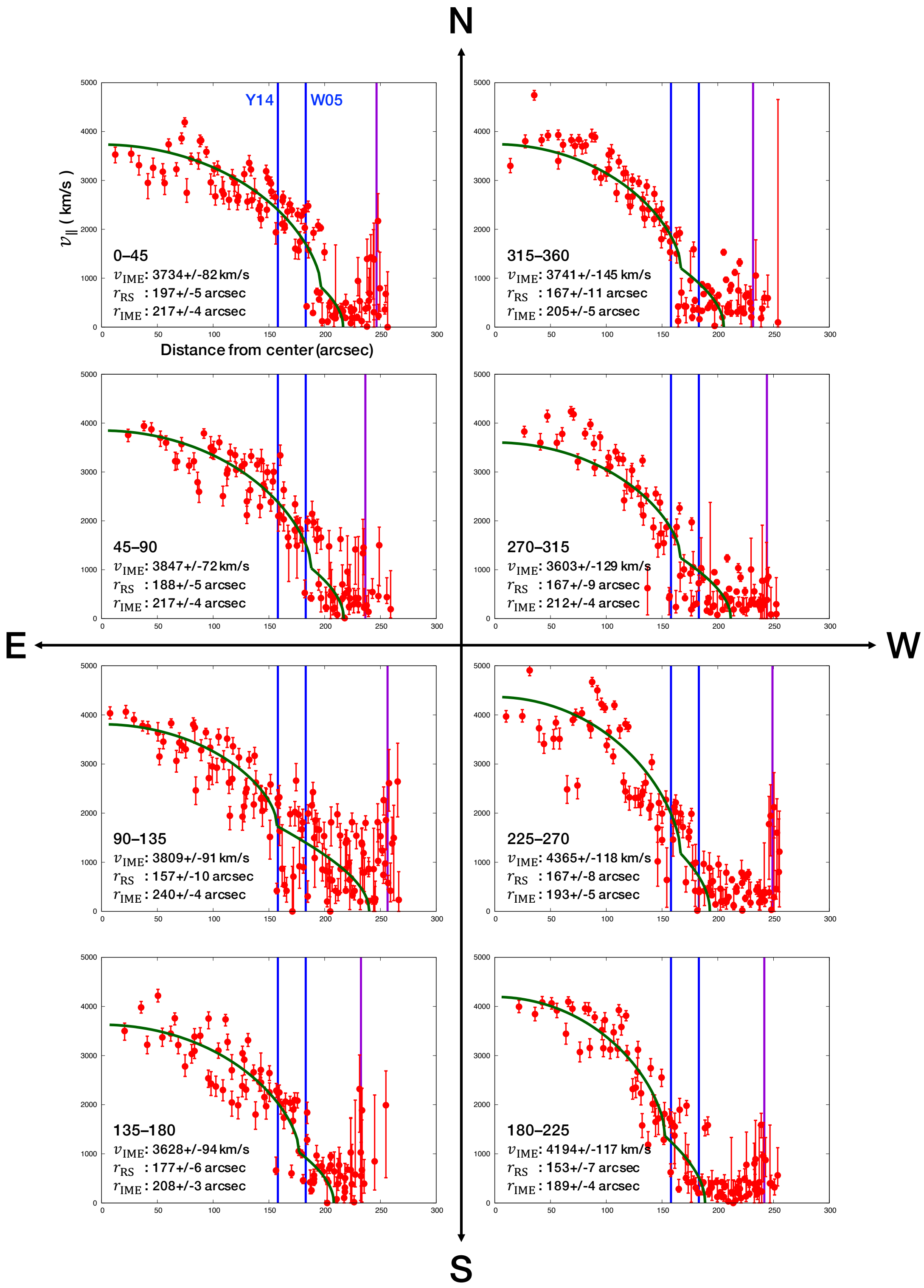

Figure 8.4: Same as Figure 7.16, but with the best-fit model of the function (Equation 8.8) as green lines. Best-fit parameters are written with 1σ confidence range at a lower-left corner in each plot. Previously reported positions of the reverse shock (W05: Warren et al. (2005) and Y14: Yamaguchi et al. (2014a) as the blue lines) and our observed $r_{\rm CD}$ (violet) are also plotted.

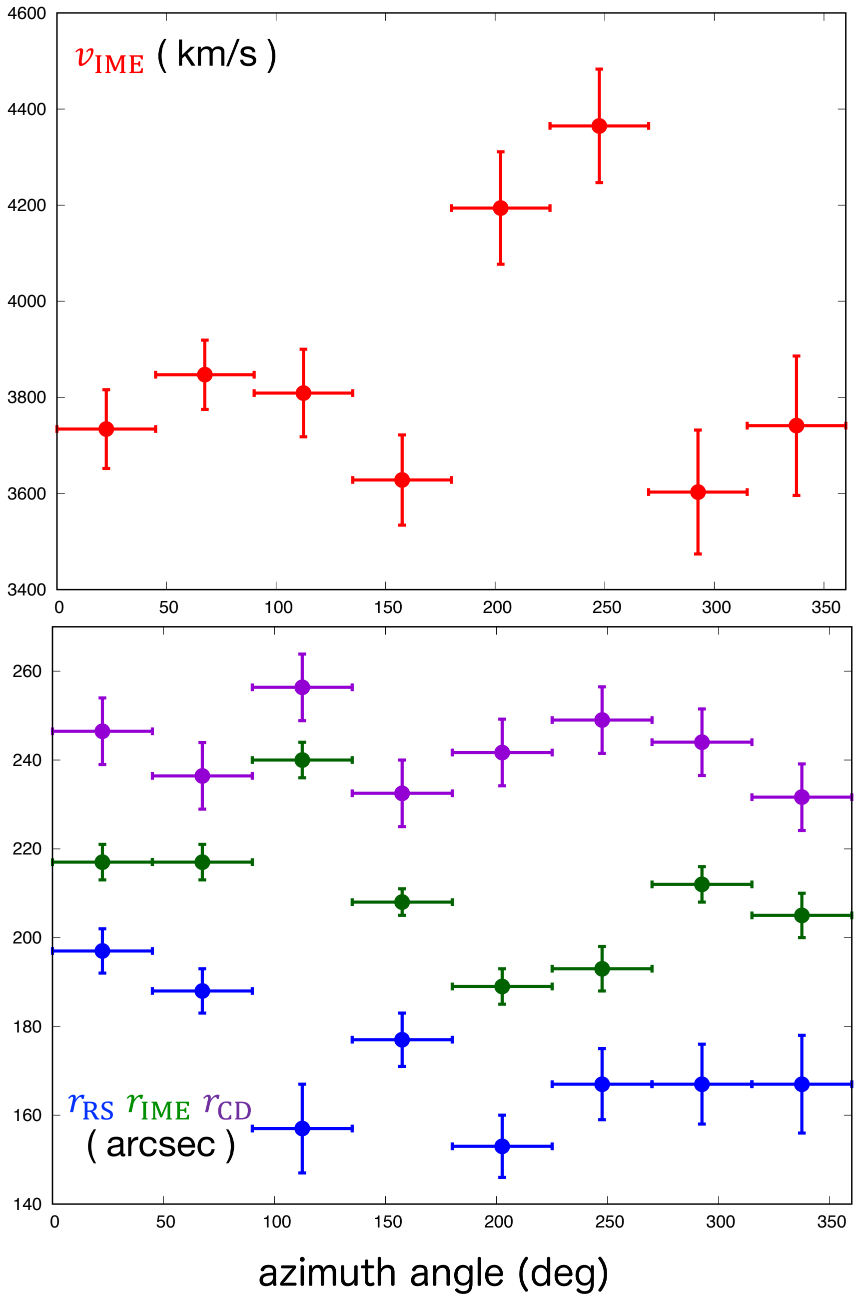

Figure 8.5: Fitting results of $v_{\parallel}$, $r_{\rm RS}$, and $r_{\rm IME}$ for each circular sector. We also plot observed $r_{\rm CD}$ in the bottom figure.

8.3.1 3-dimensional velocity for inner ejecta

The best-fit parameters $v_{\rm IME}$ in all sectors are similar, and the typical value is estimated to be 4,000±500 km sec^{-1}. This value is reasonable considering that the free expanding ejecta with the velocity of $\sim$10,000 km sec^{-1} is decelerated to half of its original velocity by the reverse shock.

Hayato et al. (2010) previously measured the 3-dimensional velocity of the silicon ejecta, and it was a little higher value, ~4,700 km sec^{-1}. On the other hand, their measured value of the line-of-sight velocity at the center of the remnant is ~3,500 km sec^{-1} and it is consistent with our results. This inconsistency of 3-dimensional expansion velocity could come from the difference of the conversion method from the line-of-sight velocity. Hayato et al. (2010) tried to compensate the worse spatial resolution of *Suzaku*, ~2 arcmin in FWHM (Serlemitsos et al., 2007) which is >25 times worse than that of *XMM-Newton*, by correcting its large point-spreading function. Their method could contain large systematic uncertainty, which would be able to explain this gap.

8.3.2 Position of the reverse shock

The bending point r_{RS} of the fitting curve can be regarded as the reverse shock position. In the north-west quarter, the best-fit value is 167±10 arcsec. It means the reverse shock has not reached the center of the remnant, which is natural for such young SNRs.

This position is located at the middle of the reported positions by previous works (183 arcsec: Warren et al. (2005) and 158 arcsec: Yamaguchi et al. (2014a)). As described above, these previous works used the position of the emission peak of Fe-K lines. Because its emission needs hotter temperature than lighter elements like IMEs, its distribution represents the recently shocked region by the reverse shock (cf., Hwang et al., 1998; Badenes et al., 2005). However, the studies using the Fe-K emission comes up against difficulties of its smaller photon statistics compared with the Si-K emission. Even though the Fe-Kβ study with the large efficiency of the detection of their energy band in *Suzaku* (Yamaguchi et al., 2014a) is relatively reliable, it is rare case to detect a clear Fe-Kβ line in small knots. The worse spatial resolution of *Suzaku* is again too blurred to determine the locations in detail. Nevertheless our method is completely independent way to them, the reverse shock position we report in the north-west is consistent with them. Our method uses the IME emission lines including the Si-K line which is dominant in almost all cases. Figure 8.4 shows we can also estimate reasonable positions in all of the other azimuth directions. Our method could be a strong method for the position estimation of the reverse shock systematically.

8.3.3 Position of the reflected shock

The remaining parameter r_{IME} means the boundary between the two velocity structure in this fitting, therefore it represents the reflected shock position. The estimated value is 200±20 arcsec except for the abnormal sector including the Fe knot. One of the important points is the uniformity of the reflected shock position in this remnant. We will discuss the reason for this deceleration in the following sections.

8.4 Circumstellar media in Tycho's SNR

8.4.1 Interpretation of our results

This almost uniform result suggests that such deceleration occurs everywhere around Tycho's SNR. It means that this remnant is surrounded by dense and cavity-like materials. According to the 1-dimensional hydrodynamical simulations, we need $\sim$100–1,000 times denser materials than the typical ISM density $\sim$0.1 cm^{-3}. Some studies have suggested the existence of associating molecular clouds by observing other wave length (e.g., Zhou et al., 2016; Arias et al., 2019). Although the typical density of the molecular clouds is $\sim$10–100 cm^{-3}, Zhou et al. (2016) suggested the density of this cloud is <0.1 cm^{-3}.

Nevertheless, our result may show another dense molecular cloud, it is unnatural that such existing interstellar gas had happened to form such cavity-like structure around the progenitor system of Tycho's SN. Instead, it is more reasonable to interpret this dense gas comes from the CSM, despite the expectation of the DD scenario. To test the hypothesis of the CSM, we need to calculate the mass loss rate of its progenitor system assuming the SD scenario. Such CSM is thought to be formed by the strong progenitor wind from the WD (Hachisu et al., 1996). Assuming the distance to Tycho's SNR from the earth to be 3 kpc, which is the mean value of previous studies (see Figure 6 in Hayato et al., 2010, for a review), $r_{\rm IME}$ $\sim$200 arcsec is converted to $\sim$3 pc $\simeq 1 \times 10^{14}$ km. Using typical wind speed $v_{\rm w}$ $\sim$100 km sec^{-1} (Kato & Hachisu, 1999), the time to approach the present position for the wind $t_{\rm w}$ is $3 \times 10^4 (v_{\rm w}/100~{\rm km/s})^{-1}$ yr. Note that $t_{\rm w}$ must be larger than the age of the remnant. Assuming the inner materials of the cavity without the ejecta is completely the CSM, the total mass can be calculated using the volume of the sphere whose radius is 3 pc, the density n, and the proton mass $\sim 10^{-57}~M_\odot$. Thus, the mass-loss rate $\dot{M}$ is $\sim 10^{-5} (n/0.1~{\rm cm}^{-3})(v_{\rm w}/100~{\rm km/s}) M_\odot~{\rm yr}^{-1}$. This approximate can get large or small considering the mass of the inner ISM and the CSM cavity. Thus, this value is regarded to be consistent with the typical value of $\dot{M} \sim 10^{-6} M_\odot~{\rm yr}^{-1}$ for the SD scenario (Zhou et al., 2016). Therefore, this dense cavity could be the CSM.

8.4.2 Comparison with forward shock observations

Tanaka et al. (2021) measured the time variability of the non-thermal emission at the edge of Tycho's SNR and found a decelerating structure with $\sim$2,000 km sec^{-1} of the angular motion of the forward shock mainly around the south half only in these 15 years. They concluded such deceleration is due to the collision with cavity-like CSM around the remnant right now.

The deceleration of the forward shock is mainly observed in the south half (Figure 2 in Tanaka et al., 2021). However, the reflected shock in our result seems to reach the inner position there than that in the north half compared to the geometrical edge of the ejecta

(Figure 8.5). Although it looks contradiction, we should keep in mind that they studied in the angular direction, while we study in the line-of-sight direction. This difference could be interpreted as suggesting that the CSM cavity of this remnant is anisotropic.

8.4.3 Interpretation of thermal parameters

Electron temperature

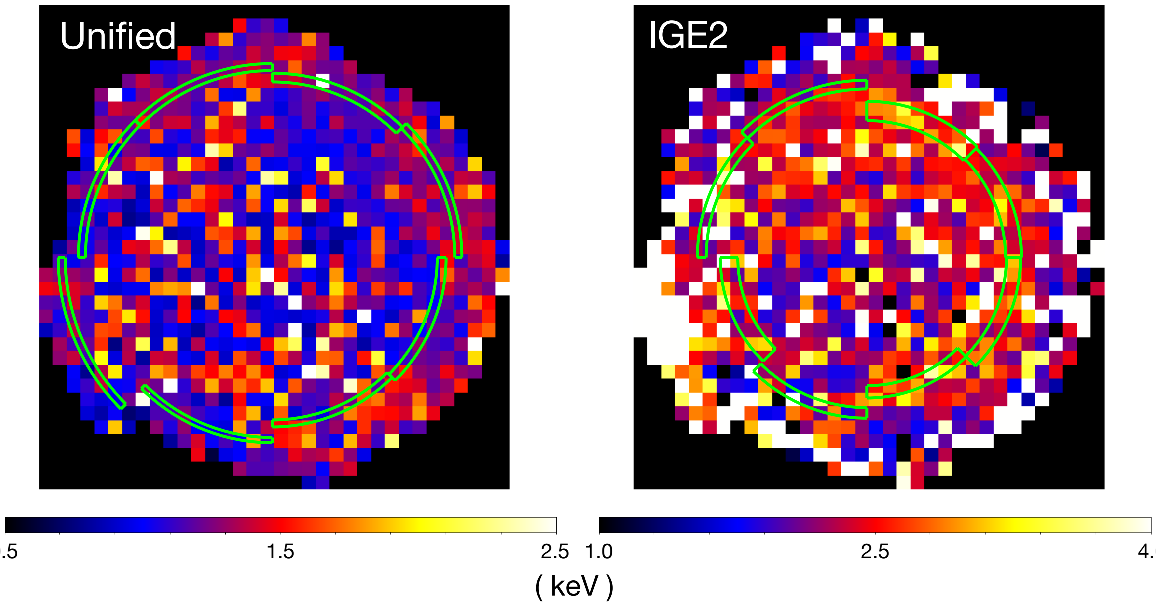

Figure 8.6: Same as Figure 7.7, but with r_{IME} on the unified electron temperature and r_{RS} on that of the second IGE component. The scale range is also changed.

If the deceleration is due to the collision between the ejecta and some dense materials, the electron temperature will be heated there. In order to confirm it, Figure 8.6 again shows the unified electron temperature map but with our estimated position of r_{IME} for each circular sector. Note that the 1σ error is typically 0.3 keV. In the south-west quarter, the general electron temperature is ~1.5 keV outer from r_{IME}, where bright non-thermal emissions are located. It looks heated by comparing with inner temperature ~1.0 keV, but such trend is not significant, unfortunately.

Because the Fe-K emission plays a role as an indicator of the reverse shock in previous works (Warren et al., 2005; Yamaguchi et al., 2014a), we also compare the electron temperature of the second IGE component with r_{RS} in Figure 8.6. Focusing on the inner structure of the electron temperature, it seems to get its peak along with the reverse shock. Despite the difficulty of estimating the electron temperature for each component, it could be the first direct observation of the reverse shock heating. Yamaguchi et al. (2014a) suggested so efficient collisionless shock heating at the reverse shock front that the ratio of the electron temperature to the ion temperature β is $\sim$0.01. Note that a general heating process via the ion-electron Coulomb collision following Equation 2.9 results for β in $\sim 10^{-5}$. Although Figure 7 in Yamaguchi et al. (2014a) shows the peak temperature at the reverse shock front will be $\sim$20 keV, the same figure shows electrons are cooled to $\sim$3 keV after leaving $\sim 20d_3$ arcsec. Our analysis with 15 arcsec grids cannot catch the peak temperature due to spatially smoothing. However, our averaged peak temperature $\sim$4 keV cannot be explained by $\beta <0.003$ models in Yamaguchi et al. (2014a). Therefore, our analysis would support their estimation of the efficient collisionless shock heating.

Ionization timescale

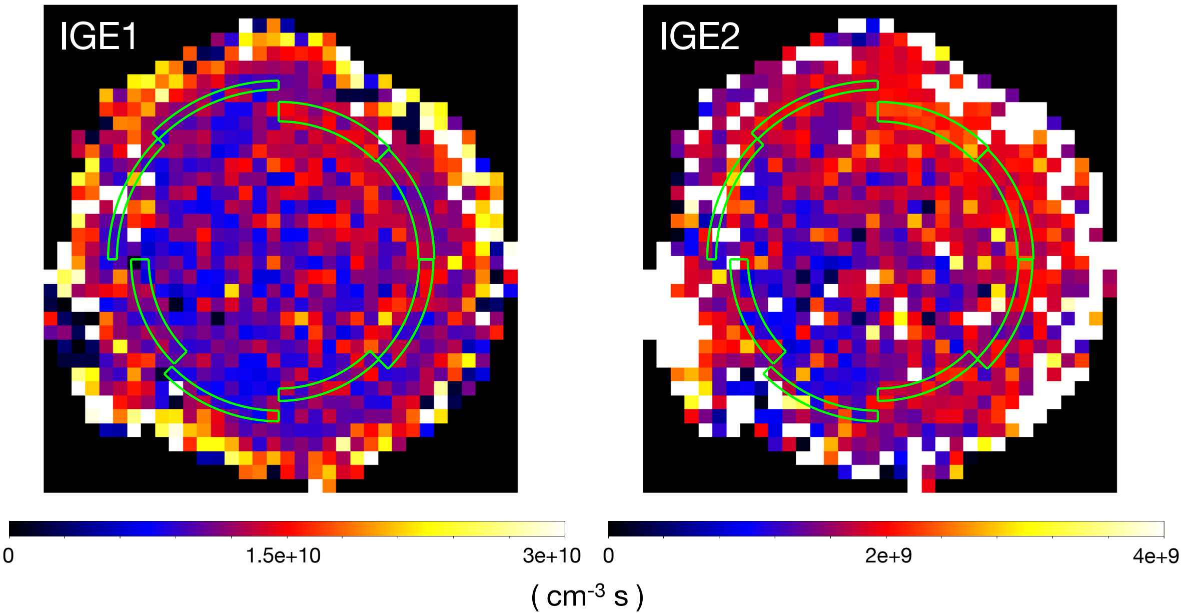

Figure 8.7: Same as Figure 7.8, but with $r_{\rm RS}$ for the ionization timescale maps of the IGE components. The scale range is also changed.

The ionization timescale, which is the product of the electron density by the elapsed time after being shocked by the reverse shock, should be the smallest at the reverse shock front and get larger monotonically if considered simply. However, our result in Figure 8.7 does not seem to have any correlation with our estimated position of the reverse shock. The ionization timescale shows rather the asymmetry between the west and east. It is probably because the difference of the density of heated materials. Except for the edge, where it is difficult to estimate this parameter due to weak emission lines, this parameter is generally twice larger in the west half than that in the east. It could indicate the asymmetry of the original SN of Tycho (cf., Ferrand et al., 2019, 2021).

Chapter 9

General Discussions

9.1 Similarity and difference of these two SNRs

In Kepler analysis, we have found the deceleration of the ejecta with 1,000 km sec^{-1} in our side including the shrinkage of the kinematics at the central torus. In Tycho analysis, we have also found the deceleration with 2,500 km sec^{-1} around the remnant. These results show that the kinematics of the ejecta in both SNRs is inhibited by their CSM.

While we suggest the existence of the CSM through the study of the kinematics of the ejecta, the emission from CSM is completely different in these two SNRs. Even before our study, Kepler's SNR has been reported as belonging to a dense CSM through X-ray observations (Kinugasa & Tsunemi, 1999; Reynolds et al., 2007). Katsuda et al. (2015) did high resolution spectroscopy and found that its CSM is distributed over the entire remnant, even though its density at the southern half is lower. In contrast to it, there has been no confirmed CSM emission around Tycho's SNR.

Admitting both our results and previous results, the possible solution is that the weak CSM emission is buried in other bright emission components from ejecta in Tycho's SNR, or they have not been emitted. Recent studies of the motion of the forward shock give us some hints at this point. Coffin et al. (2021) measured the acceleration of the forward shock front in Kepler's SNR and revealed that it had already been decelerated sufficiently. On the other hand, Tanaka et al. (2021) found the recent deceleration in Tycho's SNR. These results suggest the difference of the timing of the interaction with their own CSM. Older interaction in Kepler's SNR could realize enough time to heat the CSM. The CSM in Kepler's SNR would be close to the explosion center.

The reason for this difference in the CSM structure of both SNRs could be due to the difference of other diversity of type Ia SNe. While the existence of CSM is one of the critical clues of the SD scenario, we have still diversities in the mechanism of the explosion or the type of the companion star (see §2.1.3). For example, Katsuda et al. (2015) suggests that the progenitor of Kepler's SNR is sub-classified to 1991Tlikes, which is a little brighter SNe (Filippenko et al., 1992; Rest et al., 2008). We need to simulate the evolution of SNRs to discuss this point in detail. Recent simulations study the detailed history of young SNRs from the moment of the explosion without considering the anisotropy of their circumstances (cf., Ferrand et al., 2019, 2021). Our study will require such simulations to consider the more complicated situations accompanying CSM.

9.2 General meanings of this study

In our study, we choose only the two brightest Ia SNRs. Our study tries to reach the limit of the analysis using CCD detectors in terms of the spatial resolution and energy resolution. We need observational targets which are large enough for spatially resolving, bright enough for X-ray spectroscopy, and young enough for measuring the kinematics of the ejecta. These two SNRs are the best and only candidates for these conditions.

Although our results suggest the origins of these SNRs are both the SD scenario, we will not claim that all type Ia SNe are in the SD scenario. Hitomi Collaboration et al. (2017) required there are equivalent amounts of the SD and DD scenarios for explaining the observed abundance ratio of IGEs. However, our results warn that the absence of the CSM emission does not mean the absence of the CSM, i.e., the DD candidate. Note that we have not concluded any SNRs as the DD origin.

A similar claim is applied to the studies of morphology. Many previous studies have tried to study the 2-dimensional morphology of SNRs. Some of them revealed relationships between morphology and physical parameters. For example, Lopez et al. (2011) systematically analyzed 24 SNRs emitting X-rays by converting their X-ray morphology to the quadrupole power ratio. They found type Ia SNRs are more spherical than Core-Collapse ones, which indicates more complicated environment in CC SNRs due to the CSM as its common characteristics. Similar studies followed to it. Peters et al. (2013) re-confirmed it, and additionally shows the octupole power ratio also can discriminate SNRs into the two types by using 24 μm emission morphology. Stafford et al. (2019) analyzed the radio continuum image in 96 SNRs, and found the aged ones shows more asymmetric since they sweep up the ISM. Another example is Holland-Ashford et al. (2020), who analyzed the X-ray morphology of each ejecta element in Cassiopeia A and revealed the high asymmetricity for heavy elements.

Tycho's SNR shows circular appearance in contrast to Kepler's SNR (see Figures 7.3 & 4.3 and Lopez et al., 2011). Such morphological difference impresses us that such circular SNRs have a sparser environment. However, our analysis shows the possibility that the ejecta in such SNRs could interact with dense CSM to those in dumb ones. 2-dimensional morphology has only the information in the angular angle. Such difference could be only the difference of the direction to the earth, ultimately. We want to raise an example of the classification of AGN. AGN with broad Hα emission lines are called Seyfert I, and those with narrow lines are Seyfert II. However, these two different lines are emitted from two different regions in the same AGN structure, and the inclination angle to the earth makes such difference which emission is outstanding. Objects with complicated structure like AGN and SNRs always have an unavoidable bias that we have to observe only from the earth. We claim the importance of studies in the line-of-sight direction like this study as well as those in the angular direction for understanding such astrophysical phenomena.

9.3 Calorimeters

Throughout all of this study, we have sometimes been faced with some difficulties due to the limit of the performance of existing CCD detectors. The critical one is the energy resolution. We cannot resolve the red- and blue-shifted ejecta directly in the observed spectrum, and cannot resolve the ONeMg or Fe-L emission lines with 2-dimensional spatial resolution. We should not ignore the uncertainty of the other thermal parameters including the temperature and ionization timescale. Our studies have made some efforts to overcome these difficulties to approach new sciences, but detectors with superior energy resolution will make such studies more certain.

The calorimeter system will help us on this point. It determines the incident X-ray energy by measuring the rise in temperature of cryogenic detectors, which realize the superconductivity. It achieves the energy resolution with ∼5 eV in the entire X-ray energy band, thus the energy resolution of the Fe-K band gets improved sufficiently more than 10 times superior to existing CCD detectors. For example, this resolution is converted to the velocity of ∼0.1 % of the light speed, and we can even resolve the ejecta velocity which is equivalent to that of the ISM in the old SNRs.

The calorimeter system has unfortunately failed to sufficiently show its power in these 20 years including the accidents of *ASTRO-E*[1], the X-Ray Spectrometer (XRS) (Kelley et al., 2007) on board *Suzaku* (Mitsuda et al., 2007), and the Soft X-ray Spectrometer (SXS) (Kelley et al., 2016) on board *Hitomi* (Takahashi et al., 2016). However, the Resolve detector on board *XRISM* mission (Tashiro et al., 2018) will finally realize this detector. Even though the spatial resolution of *XRISM*, which is comparable with *Suzaku*, is insufficient to our spatially resolved study, the *Athena+* mission (Nandra et al., 2013) and the concept study of *Lynx* (Gaskin et al., 2019; Lynx Concept Study Report, 2019) will satify us in terms of both resolutions.

If we can use calorimeters with sufficient spatial resolution, the study of ejecta kinematics can be applied to smaller or darker SNRs (Figure 9.1). The best candidates are

---

[1] Satellites are named at the moment of the orbit insertion. In this sense, *ASTRO-E* was never named as *Hiryu* officially.

N103B and SNR 0509-67.5, whose ages are below 1,000 yrs. The origin of N103B is subclassified to the remnants of SNe Ia-CSM (Leloudas et al., 2015) and the strong X-ray emission of CSM with the double-ring structure is found (Yamaguchi et al., 2021). On the other hand, 0509-67.5 shows circular morphology and no emission from CSM. These pairs can be a good comparison with our targets, Kepler and Tycho. Another candidate pair is RCW86 and SN1006. They are well-studied old SNRs, and RCW86 has a clear CSM structure (Vink et al., 1997), while SN1006[2], who shows circular appearance, has not. In addition to them, we should study 3C397, whose origin is revealed as the SD scenario by studying the strong IGE emission line (Yamaguchi et al., 2015; Ohshiro et al., 2021).

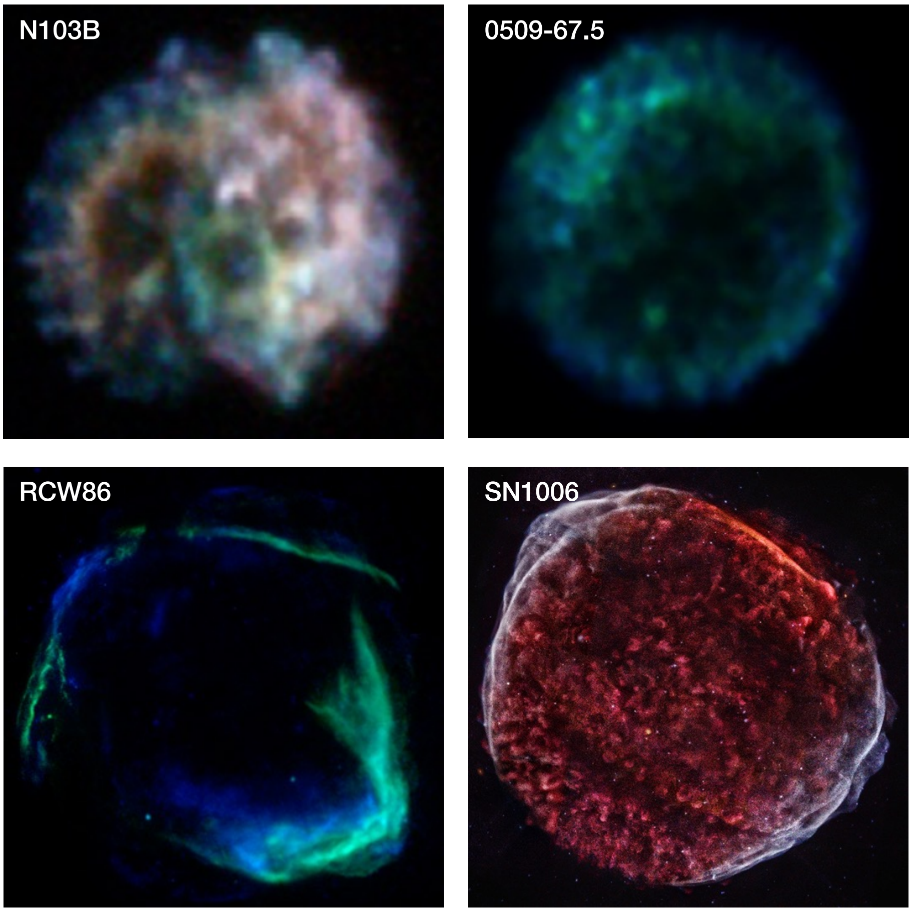

Figure 9.1: X-ray Images of other candidates for our study. Images are cited from *Chandra* Photo Album (NASA/CXC/SAO).

---

[2] We conventionally call the remnant of SN exploding in 1006 on the earth as “SN”1006. Note that the supernova itself in 1006 was also observed in Japan. This is recorded in Meigetsu-ki with the origin of Crab Nebula (SN1054) (Fujiwara, 1230), but Fujiwara-no Teika had never observed them by himself.

Chapter 10

Conclusions

The existence of CSM in type Ia SNRs is one of the important clues to the SD origin of its progenitor system. The unique method of our study is searching CSM by the ejecta kinematics in SNRs in the line-of-sight direction. Kepler's SNR is the main candidate of the SD remnant because it accompanies the strong CSM emission around it. We found the deceleration of the ejecta about 1,000 km sec^{-1} by the dense CSM in our side, according to our high resolution spectroscopy using the RGS detectors in *XMM-Newton*. We also found the inhibition of the ejecta kinematics in the dense torus at the central structure, where the line width of the characteristic X-ray lines of the ejecta emission is narrow compared to that in the outer region.

One of its strong points is that this method does not need the direct emission from CSM, we could not observe due to whose absence or whose weakness. Tycho's SNR is the famous remnant without any detection from its CSM and its ISM and is thought to be the remnant of the DD scenario. However, our spatially resolved analysis using the MOS detectors in *XMM-Newton* also found the deceleration of the ejecta velocity about 2,500 km sec^{-1} at the outer region in almost all the azimuth direction. This deceleration is interpreted as the evidence of the reflected shock generated by the interaction with the dense CSM cavity around the remnant.

Combining the previous results measuring the velocity of the forward shock in the angular direction in each SNR (Coffin et al., 2021; Tanaka et al., 2021), the evolution of these remnants are thought to be inhibited by their CSM. Therefore, these results favor the SD-like origin for these SNRs, although that of Tycho's SNR has been thought to be the DD origin. The difference of the emission from the CSM component could be due to the elapsed time from the interaction.

Our study exhibits that measuring the ejecta kinematics could help to distinguish the origin of type Ia SNRs, in addition to the direct detection of the key emission lines. Even though we have studied only two SNRs, the brand new technology of the calorimeters will increase the candidates of targets in the next generation of X-ray astrophysics.

Appendix A

Sacrificial Charge Problem in *Chandra* ACIS-I detectors

In the main text above, we adopt *XMM-Newton* EPIC-MOS detectors for spectroscopy. However, *Chandra* ACIS detectors are more widely used with their great spatial resolution and convenience for analyzing by the sophisticated software package `CIAO`. The reason why we avoid using them is that the observation data of Tycho's SNR by *Chandra* ACIS-I detectors has a critical error especially at the north-west region. In this chapter, we describe its details below.

A.1 Sacrificial Charge

A.1.1 Charge Transfer Inefficiency

The large difference between silicon detectors like CCD on the ground and ones in space is the radiation damages by cosmic rays. Cosmic rays around a spacecraft, high energetic protons, for example, could attack the silicon in the detectors and break its lattice structure, which is called lattice defect. Such defects lack electrons and could trap the charges generated by the incident X-rays being transferred in the read-out direction (Gendreau et al., 1995). If so, the read-outed charge number gets small, and the calculated incident energy E gets lower than the true value E_0. This effect is called Charge Transfer Inefficiency (CTI). To estimate the true energy E_0, we should correct CTI by assuming the number of lattice defects as a function of the elapsed time from the launch and the detector coordinate (cf., Townsley et al., 2000). Although *Chandra* ACIS and *XMM-Newton* EPIC have no choice but rely on this inaccurate CTI correction method, *Suzaku* XIS have another effective option for CTI. XIS detectors inject "artificial" charges for filling the lattice defects in advance and avoids being trapped for true charges we want (cf., Bautz et al., 2004). This is called spaced-row Charge Injection (CI).

A.1.2 Problem of sacrificial charges

When another photon incidents in the read-out line of CCD detectors during the read-out period, these additional “real” charges will behave as the injected charges of CI. Such charges are called “sacrificial charges” because their original photon event is never recognized. Although the word “sacrificial” focuses on wasting valuable events in the small photon statistics in the X-ray band, it also affects the energy calibration. The CTI correction process without CI assumes that there exists some lattice defects. If such defects are already filled by trapped sacrificial charges, the CTI correction will get over-estimated. We will recognize as if the photon energy E is higher than true energy E_0.

This effect could easily happen in the situations below. At first, it needs a high frequency of incident photons. It means the X-ray target is so bright. In addition, its probability gets larger when the detected position is distant from the read-out electrode. Especially, the most critical situation is that a bright and extended source that lies along the read-out direction is observed at the edge of the detector on the other side of the read-out electrodes. In *Chandra* ACIS-I detectors (see §3.2), we can see the read-out direction of all four CCDs lines up parallelly (Figure 3.6). An observation of a bright and extended source located around the center of ACIS-I detectors could be expected as the dangerous situation of this problem.

A.2 Tycho's SNR observed by *Chandra* ACIS-I detectors

A.2.1 Observations of Tycho's SNR

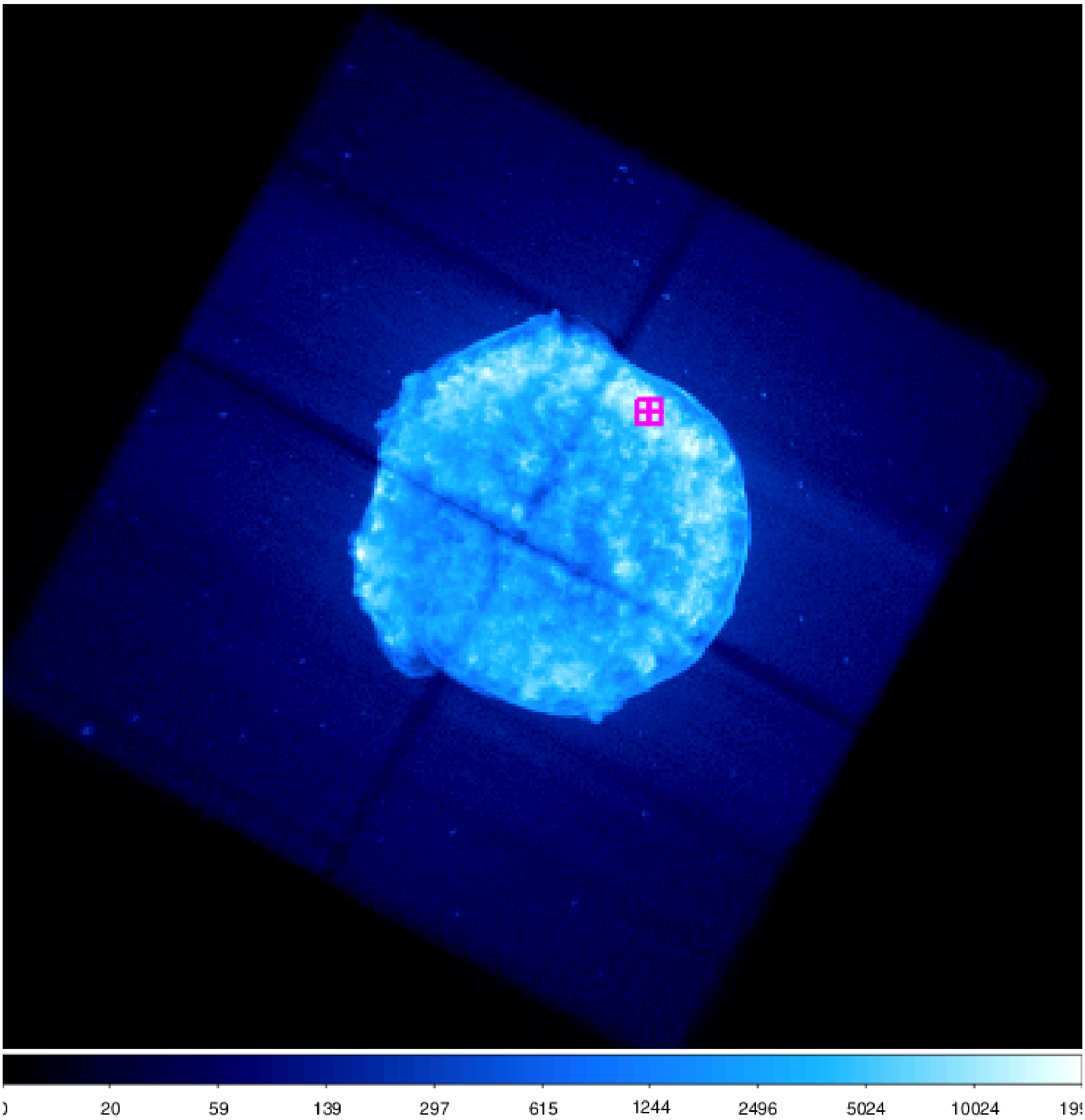

Figure A.1: Detected event count image of Tycho's SNR observed by *Chandra* ACIS-I detectors on a logarithmic scale. The groove is due to the gap of four CCDs in ACIS-I (see Figure 3.6). Four magenta boxes are sky pixels where we extract spectra.

Table A.1: Observation list of Tycho's SNR by *Chandra*.

Observation ID	Start Date	Exposure (sec)
10097	2009.04.11	107430
10904	2009.04.13	34700
10093	2009.04.13	118350
10902	2009.04.15	39530
10903	2009.04.17	23920
10094	2009.04.18	89970
10095	2009.04.23	173370
10096	2009.04.27	105720
10906	2009.05.03	41120
total		734110

Chandra spacecraft has observed Tycho's SNR several times. The most widely used data are the longest observation set ∼734 ksec in 2009 (Table A.1). These data are only observed by ACIS-I detectors because Tycho's SNR is too large to observe by a single CCD chip in ACIS-S. We reprocess the raw data by `chandra_repro` in the `CIAO 4.13` package. After that, we make the event count map by merging all the data of them (Figure A.1). Even though the CCD configuration gap in ACIS-I is smoothed because of the slightly different centering position of each observation, we still see the artificial cross in this image.

A.2.2 Comparison with ACIS-I and MOS spectra

To check the *Chandra* ACIS-I spectrum, we compare it with the one by *XMM-Newton* EPIC-MOS detectors. We choose bright sky pixels at the northwest of Tycho's SNR, whose (x, y) coordinates are (25,26), (25,27), (26,26), (26,27) in Figure 7.5. Here, the northwest rim of this remnant is one of the brightest regions in the observed X-ray sky. Also, here in the detector coordinate is the most distant position from the read-out electrode for the ACIS-I.

The extracted raw spectra from ACIS-I and MOS are shown in Figure A.2(a). The spectral shape is wider in ACIS-I than that in MOS and some weak emission lines are covered by a continuum-like component. Because this spectral shape could be only due to the difference of the detector response or the energy resolution and not affect fitting parameters, we test to fit each spectrum independently in the following step. For simplicity, we extract only the IME band and assuming single NEI component for the ejecta (see §7.2). The fitting results are shown in Figure A.2(b) and the best-fit parameters are

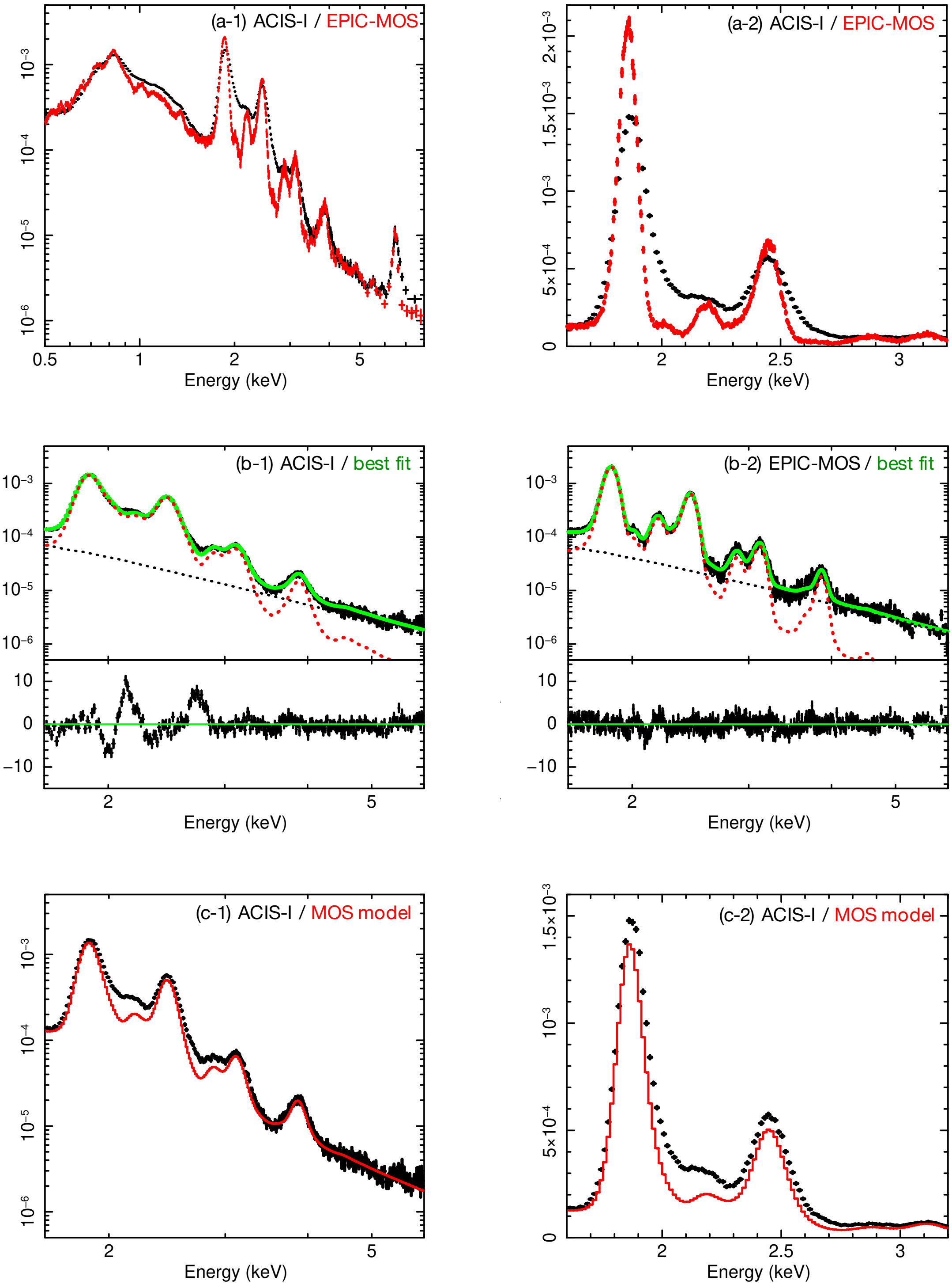

Figure A.2: (a) Extracted spectra from *Chandra* ACIS-I (black) and *XMM-Newton* EPIC-MOS (red) on a logarithmic scale (a-1) and linear scale (a-2). Observation list is in Table 7.1 and A.1. (b) Best-fitted fitting results for ACIS-I (b-1) and MOS (b-2) spectrum. (c) ACIS-I spectrum with MOS-fitted model on a logarithmic scale (c-1) and linear scale (c-2).

in Table A.2. According to the fitting residuals in Figure A.2(b), nevertheless this simplest emission model can explain the MOS spectrum generally, we cannot explain the two strong residuals in the ACIS-I spectrum. For comparison, we superpose the MOS-fitted model on the ACIS-I raw spectrum (Figure A.2(c)).

These comparison of raw spectra (Figure A.2(a)) and fitting results (Figure A.2(c)) tell us that the spectrum around silicon and sulfur emission lines extracted from *Chandra* ACIS-I is widened and shifted to higher energy due to some detector problems. The overestimated and uncertain CTI correction due to the sacrificial charge can easily explain our results as discussed above. The brightest continuous shell along the read-out direction distant from the read-out electrode is an easy prey of sacrificial charge. Williams et al. (2017) mentioned a "bad" calibration problem here, but this study reveals what happens here in detail. Figure A.2(c-2) also shows the raw spectrum around silicon and sulfur energy band of ACIS-I exceeds the true emission. It indicates that some incident photons approaching other positions are miss-judged to be detected there. This another problem may appear as the stripes along brightest regions in Figure A.1.

A.2.3 Effects on thermal parameters

Table A.2: Best-fit NEI parameters for ACIS-I and MOS spectra.

Parameter	*Chandra* ACIS-I	*XMM-Newton* MOS
Doppler velocity (km/s)	-476^{+29}_{-27}	-392 ± 14
Line width σ at 6 keV (eV)	64.1 ± 1.1	< 3.5
Electron temperature (keV)	$2.07^{+0.03}_{-0.01}$	1.05 ± 0.01
Ionization timescale (10^{10} cm^{-3} sec)	$4.62^{+0.07}_{-0.16}$	5.01 ± 0.04
Abundance ratio S/Si	$0.667^{+0.003}_{-0.005}$	0.986 ± 0.006
Abundance ratio Ar/Si	0.443 ± 0.010	1.457 ± 0.033
Abundance ratio Ca/Si	0.738 ± 0.021	3.77 ± 0.14
W-stat (DOF)	1380 (290)	1337 (879)

Errors are shown in 1σ confidential level.

The trial of fitting ACIS-I data forcibly intends to explain such an artificial spectrum by changing the thermal parameters of an NEI model representing an IME component. As a result, the best-fit parameters are contradictory (Table A.2). The broadening effect results in the wider parameter of the line width. It could be interpreted as a mysterious velocity difference in the line-of-sight of red- and blue-shifted ejecta even at the edge of the SNR, which is a completely different expansion structure discussed in the main part of this thesis. The ion temperature could get more than 100 times higher than that is estimated by analyzing *XMM-Newton*. The energy shift will be also explained by the highly blue-shifted structure. Other than such Doppler parameters, the overestimation of photon energy imitates the higher emission ratio of Heβ/Heα and Lyβ/Heα, especially of silicon and sulfur because of their brightness. To explain this result, the electron temperature parameter for ACIS-I is two times higher than that for MOS.

Although such thermal parameters are distorted, we still cannot explain strong residuals around Lyα lines of silicon and sulfur in Figure A.2(b-1). It is thought to be due to the overestimation of Heβ emission. To explain them by thermal emission parameters, we need extremely blue-shifted Heβ line ~10,000 km sec^{-1} in the line-of-sight direction, which is the highest 3D velocity of unheated ejecta nevertheless there is located near the edge. Alternative options are outstanding emission of satellite lines from the dielectronic recombination plasma, recombining plasma, or K-shell emission lines from phosphorus and chlorine (see Table 2.2). These would be "sensational" mistakes in the X-ray astrophysics. This problem could be occurred not only here but appear over this remnant. We should check the validity of the observational data before analyzing them.

A.2.4 Difference between ACIS-I and EPIC-MOS

Different from a novel CI process in *Suzaku* XIS detectors, both *Chandra* ACIS-I and *XMM-Newton* EPIC-MOS do not equip such a technical method and rely on normal CTI correction method. However, the fatal critical problem only appears in the ACIS-I spectrum. Some clues are already shown. The bright regions in Tycho's SNR are located distant from ACIS-I read-out electrodes (Figure A.1), which results in encountering large number of lattice defect, while the detected position on MOS is near the center of the CCD chip (Figure 7.1). MOS has also an advantage of equipping two detectors whose read-out directions are orthogonal. Other than these, we note a historical background. *Chandra* observatory was launched on July 23, 1999, and immediately after that the CCD detectors were damaged by the high radiation environment at the Earth's radiation belts (Townsley et al., 2002). Learning from this, *XMM-Newton* observatory, who was launched on December 10 in the same year, avoids there for the location of observing in order to decrease the number of lattice defects (cf., Ferrando et al., 2003). This thesis will not pursue the details of this problem, but we should investigate them in future.

Bibliography

Arias, M., Vink, J., Zhou, P., et al. 2019, The Astronomical Journal, 158, 253

Arnaud, K. A. 1996, in Astronomical Society of the Pacific Conference Series, Vol. 101, Astronomical Data Analysis Software and Systems V, ed. G. H. Jacoby & J. Barnes, 17

Aschenbach, B., Briel, U. G., Haberl, F., et al. 2000, in Society of Photo-Optical Instrumentation Engineers (SPIE) Conference Series, Vol. 4012, X-Ray Optics, Instruments, and Missions III, ed. J. E. Truemper & B. Aschenbach, 731–739

Baade, W. 1945, The Astrophysical Journal, 102, 309

Badenes, C., Borkowski, K. J., & Bravo, E. 2005, The Astrophysical Journal, 624, 198

Bamba, A., Yamazaki, R., Yoshida, T., Terasawa, T., & Koyama, K. 2005, The Astrophysical Journal, 621, 793

Bandiera, R. 1987, The Astrophysical Journal, 319, 885

Bandiera, R., & van den Bergh, S. 1991, The Astrophysical Journal, 374, 186

Bautz, M. W., Kissel, S. E., Prigozhin, G. Y., et al. 2004, in Society of Photo-Optical Instrumentation Engineers (SPIE) Conference Series, Vol. 5501, High-Energy Detectors in Astronomy, ed. A. D. Holland, 111–122

Blackburn, J. K. 1995, in Astronomical Society of the Pacific Conference Series, Vol. 77, Astronomical Data Analysis Software and Systems IV, ed. R. A. Shaw, H. E. Payne, & J. J. E. Hayes, 367

Blair, W. P., Long, K. S., & Vancura, O. 1991, The Astrophysical Journal, 366, 484

Blondin, J. M., & Ellison, D. C. 2001, The Astrophysical Journal, 560, 244

Borkowski, K. J., Blondin, J. M., & Sarazin, C. L. 1992, The Astrophysical Journal, 400, 222

Brahe, T., & Kepler, J. 1602, Tychonis Brahe Astronomiae instauratae progymnasmata: quorum haec prima pars de restitutione motuum SOLIS et lunae stellarumque inerrantium tractat, et praeterea de admiranda nova stella anno 1572 exorta luculenter agit.

Brinkman, A., Aarts, H., den Boggende, A., et al. 1998, in Science with XMM, 2

Burkey, M. T., Reynolds, S. P., Borkowski, K. J., & Blondin, J. M. 2013, The Astrophysical Journal, 764, 63

Cappellari, M., & Copin, Y. 2003, Monthly Notice of the Royal Astronomical Society, 342, 345

Carter, J. A., & Read, A. M. 2007, Astronomy and Astrophysics, 464, 1155

Cash, W. 1979, The Astrophysical Journal, 228, 939

Cassam-Chenaï, G., Decourchelle, A., Ballet, J., et al. 2004, Astronomy and Astrophysics, 414, 545

Cassam-Chenaï, G., Hughes, J. P., Ballet, J., & Decourchelle, A. 2007, The Astrophysical Journal, 665, 315

Chandra Proposers' Observatory Guide, Version 24.0. 2020, NASA: Chandra X-ray Center, ed. unknown. `https://cxc.cfa.harvard.edu/proposer/POG/pdf/MPOG.pdf`

Chandrasekhar, S. 1935, Monthly Notices of the Royal Astronomical Society, 95, 207

Chevalier, R. A. 1982, The Astrophysical Journal, 258, 790

Chiotellis, A., Schure, K. M., & Vink, J. 2012, Astronomy & Astrophysics, 537, A139

Coffin, S. C., Williams, B. J., & Katsuda, S. 2021, accepted in The Astrophysical Journal

Comastri, A., Setti, G., Zamorani, G., & Hasinger, G. 1995, Astronomy and Astrophysics, 296, 1

Decourchelle, A. 2017, Supernova of 1572, Tycho's Supernova, ed. A. W. Alsabti & P. Murdin, 117

Decourchelle, A., Sauvageot, J. L., Audard, M., et al. 2001, Astronomy and Astrophysics, 365, L218

delle Colombe, L. 1606, Discorso di Lodovico delle Colombe

den Herder, J. W., Brinkman, A. C., Kahn, S. M., et al. 2001, Astronomy & Astrophysics, 365, L7

Diehl, S., & Statler, T. S. 2006, Monthly Notice of the Royal Astronomical Society, 368, 497

Douvion, T., Lagage, P. O., Cesarsky, C. J., & Dwek, E. 2001, Astronomy & Astrophysics, 373, 281

Dwarkadas, V. V. 2005, The Astrophysical Journal, 630, 892

Ferrand, G., Warren, D. C., Ono, M., et al. 2019, The Astrophysical Journal, 877, 136

—. 2021, The Astrophysical Journal, 906, 93

Ferrando, P., Abbey, A. F., Altieri, B., et al. 2003, in Society of Photo-Optical Instrumentation Engineers (SPIE) Conference Series, Vol. 4851, X-Ray and Gamma-Ray Telescopes and Instruments for Astronomy., ed. J. E. Truemper & H. D. Tananbaum, 232–242

Filippenko, A. V., Richmond, M. W., Matheson, T., et al. 1992, The Astrophysical Journal Letters, 384, L15

Foster, A. R. 2015, AtomDB 3.0 Documentation, Revision 1.0. `http://www.atomdb.org/atomdb_300_docs.pdf`

Fruscione, A., McDowell, J. C., Allen, G. E., et al. 2006, in Society of Photo-Optical Instrumentation Engineers (SPIE) Conference Series, Vol. 6270, Society of Photo-Optical Instrumentation Engineers (SPIE) Conference Series, ed. D. R. Silva & R. E. Doxsey, 62701V

Fujiwara, T. 1230, Meigetsu-ki, Vol. 52

Furuzawa, A., Ueno, D., Hayato, A., et al. 2009, The Astrophysical Journal Letters, 693, L61

Gabriel, C., Denby, M., Fyfe, D. J., et al. 2004, in Astronomical Society of the Pacific Conference Series, Vol. 314, Astronomical Data Analysis Software and Systems (ADASS) XIII, ed. F. Ochsenbein, M. G. Allen, & D. Egret, 759

Gaskin, J. A., Swartz, D. A., Vikhlinin, A., et al. 2019, Journal of Astronomical Telescopes, Instruments, and Systems, 5, 021001

Gatti, E., & Rehak, P. 1984, Nuclear Instruments and Methods in Physics Research, 225, 608

Gendreau, K. C., Prigozhin, G. Y., Huang, R. K., & Bautz, M. W. 1995, IEEE Transactions on Electron Devices, 42, 1912

Gerardy, C. L., & Fesen, R. A. 2001, The Astronomical Journal, 121, 2781

Gondoin, P., van Katwijk, K., Aschenbach, B. R., et al. 1994, in Society of Photo-Optical Instrumentation Engineers (SPIE) Conference Series, Vol. 2209, Space Optics 1994: Earth Observation and Astronomy, ed. M. G. Cerutti-Maori & P. Roussel, 438–450

Hachisu, I., Kato, M., & Nomoto, K. 1996, The Astrophysical Journal Letters, 470, L97

—. 2008, The Astrophysical Journal, 679, 1390

Hanbury Brown, R., & Hazard, C. 1952, Nature, 170, 364

Harrison, F. A., Craig, W. W., Christensen, F. E., et al. 2013, The Astrophysical Journal, 770, 103

Hayato, A., Yamaguchi, H., Tamagawa, T., et al. 2010, The Astrophysical Journal, 725, 894

Hester, J. J., Raymond, J. C., & Blair, W. P. 1994, The Astrophysical Journal, 420, 721

Hitomi Collaboration, Aharonian, F., Akamatsu, H., et al. 2017, Nature, 551, 478

Holland-Ashford, T., Lopez, L. A., & Auchettl, K. 2020, The Astrophysical Journal, 889, 144

Hwang, U., Decourchelle, A., Holt, S. S., & Petre, R. 2002, The Astrophysical Journal, 581, 1101

Hwang, U., & Gotthelf, E. V. 1997, The Astrophysical Journal, 475, 665

Hwang, U., Hughes, J. P., & Petre, R. 1998, The Astrophysical Journal, 497, 833

Iben, I., J., & Tutukov, A. V. 1984, Astrophysical Journal, Suppl. Ser., 54, 335

Ilkov, M., & Soker, N. 2012, Monthly Notices of the Royal Astronomical Society, 419, 1695

Iwamoto, K., Brachwitz, F., Nomoto, K., et al. 1999, The Astrophysical Journal Supplement Series, 125, 439

Jansen, F., Lumb, D., Altieri, B., et al. 2001, Astronomy & Astrophysics, 365, L1

Kaastra, J. S. 2017, Astronomy & Astrophysics, 605, A51

Kaastra, J. S., Paerels, F. B. S., Durret, F., Schindler, S., & Richter, P. 2008, Space Science Reviews, 134, 155

Kasuga, T., Aizawa, Y., & Hatauchi, K. 2019, Pioneering the imaging polarimetry of the cosmic hard X-ray: cipher, 27th Satellite Designing Contest. `http://www.satcon.jp/history/prize27/pdf/doc00.pdf`

Kasuga, T., Sato, T., Mori, K., Yamaguchi, H., & Bamba, A. 2018, Publications of the Astronomical Society of Japan, 70, 88

Kasuga, T., Vink, J., Katsuda, S., et al. 2021, The Astrophysical Journal, 915, 42

Kasuga, T., Odaka, H., Hatauchi, K., et al. 2020, Journal of Astronomical Telescopes, Instruments, and Systems, 6, 035002

Katayama, H., Takahashi, I., Ikebe, Y., Matsushita, K., & Freyberg, M. J. 2004, Astronomy & Astrophysics, 414, 767

Kato, M., & Hachisu, I. 1999, The Astrophysical Journal Letters, 513, L41

Katsuda, S., Ohira, Y., Mori, K., et al. 2013, The Astrophysical Journal, 768, 182

Katsuda, S., Petre, R., Hughes, J. P., et al. 2010, The Astrophysical Journal, 709, 1387

Katsuda, S., Tsunemi, H., Uchida, H., & Kimura, M. 2008, The Astrophysical Journal, 689, 225

Katsuda, S., Mori, K., Maeda, K., et al. 2015, The Astrophysical Journal, 808, 49

Kelley, R. L., Mitsuda, K., Allen, C. A., et al. 2007, Publications of the Astronomical Society of Japan, 59, 77

Kelley, R. L., Akamatsu, H., Azzarello, P., et al. 2016, in Society of Photo-Optical Instrumentation Engineers (SPIE) Conference Series, Vol. 9905, Space Telescopes and Instrumentation 2016: Ultraviolet to Gamma Ray, ed. J.-W. A. den Herder, T. Takahashi, & M. Bautz, 99050V

Kepler, J. 1606, De Stella Nova in Pede Serpentarii et qui sub ejus exortum de novo iniit, Trigono igneo

Kerzendorf, W. E., Childress, M., Scharwächter, J., Do, T., & Schmidt, B. P. 2014, The Astrophysical Journal, 782, 27

Kerzendorf, W. E., Yong, D., Schmidt, B. P., et al. 2013, The Astrophysical Journal, 774, 99

Khokhlov, A. M. 1991, Astronomy and Astrophysics, 245, L25

Kinugasa, K., & Tsunemi, H. 1999, Publications of the Astronomical Society of Japan, 51, 239

Kuntz, K. D., & Snowden, S. L. 2008, Astronomy & Astrophysics, 478, 575

Lee, J.-J., Raymond, J. C., Park, S., et al. 2010, The Astrophysical Journal Letters, 715, L146

Leloudas, G., Hsiao, E. Y., Johansson, J., et al. 2015, Astronomy & Astrophysics, 574, A61

Levenberg, K. 1944, Quarterly of Applied Mathematics, 2, 164

Lopez, L. A., Ramirez-Ruiz, E., Huppenkothen, D., Badenes, C., & Pooley, D. A. 2011, The Astrophysical Journal, 732, 114

Lopez, L. A., Grefenstette, B. W., Reynolds, S. P., et al. 2015, The Astrophysical Journal, 814, 132

Lumb, D. H., Schartel, N., & Jansen, F. A. 2012, Optical Engineering, 51, 011009

Lynx Concept Study Report. 2019, NASA: The Lynx Team. `https://wwwastro.msfc.nasa.gov/lynx/docs/LynxConceptStudy.pdf`

Marconi, A., Risaliti, G., Gilli, R., et al. 2004, Monthly Notices of the Royal Astronomical Society, 351, 169

Marquardt, D. 1963, SIAM Journal on Applied Mathematics, 11, 431

Martin, D. C., Seibert, M., Neill, J. D., et al. 2007, Nature, 448, 780

Martin, J. C. 2006, The Astronomical Journal, 131, 3047

McKee, C. F. 1974, The Astrophysical Journal, 188, 335

Millard, M. J., Bhalerao, J., Park, S., et al. 2020, The Astrophysical Journal, 893, 98

Minkowski, R. 1941, Publications of the Astronomical Society of the Pacific, 53, 224

Minkowski, R. 1959, in URSI Symp. 1: Paris Symposium on Radio Astronomy, ed. R. N. Bracewell, Vol. 9, 315

Mitsuda, K., Bautz, M., Inoue, H., et al. 2007, Publications of the Astronomical Society of Japan, 59, S1

Nagao, T., Maeda, K., & Yamanaka, M. 2017, The Astrophysical Journal, 835, 143

Nagayoshi, T., Bamba, A., Katsuda, S., & Terada, Y. 2021, Publications of the Astronomical Society of Japan, 73, 302

Nandra, K., Barret, D., Barcons, X., et al. 2013, arXiv e-prints: 1306.2307

Nevalainen, J., Markevitch, M., & Lumb, D. 2005, The Astrophysical Journal, 629, 172

Nomoto, K., & Iben, I., J. 1985, The Astrophysical Journal, 297, 531

Nousek, J. A., Garmire, G. P., Ricker, G. R., Collins, S. A., & Reigler, G. R. 1987, Astrophysical Letters and Communications, 26, 35

Ohshiro, Y., Yamaguchi, H., Leung, S.-C., et al. 2021, The Astrophysical Journal Letters, 913, L34

Okuno, T., Tanaka, T., Uchida, H., et al. 2020, The Astrophysical Journal, 894, 50

Pakmor, R., Kromer, M., Taubenberger, S., et al. 2012, The Astrophysical Journal Letters, 747, L10

Park, S., Badenes, C., Mori, K., et al. 2013, The Astrophysical Journal Letters, 767, L10

Patnaude, D. J., Badenes, C., Park, S., & Laming, J. M. 2012, The Astrophysical Journal, 756, 6

Perlmutter, S., Aldering, G., Goldhaber, G., et al. 1999, The Astrophysical Journal, 517, 565

Peters, C. L., Lopez, L. A., Ramirez-Ruiz, E., Stassun, K. G., & Figueroa-Feliciano, E. 2013, The Astrophysical Journal Letters, 771, L38

Phillips, M. M. 1993, The Astrophysical Journal Letters, 413, L105

Rest, A., Matheson, T., Blondin, S., et al. 2008, The Astrophysical Journal, 680, 1137

Reynolds, S. P., Borkowski, K. J., Hwang, U., et al. 2007, The Astrophysical Journal Letters, 668, L135

Reynoso, E. M., Moffett, D. A., Goss, W. M., et al. 1997, The Astrophysical Journal, 491, 816

Riess, A. G., Filippenko, A. V., Challis, P., et al. 1998, The Astronomical Journal, 116, 1009

Sanders, J. S. 2006, Monthly Notices of the Royal Astronomical Society, 371, 829

Sato, T., Bravo, E., Badenes, C., et al. 2020, The Astrophysical Journal, 890, 104

Sato, T., & Hughes, J. P. 2017a, The Astrophysical Journal, 845, 167

—. 2017b, The Astrophysical Journal, 840, 112

Sato, T., Katsuda, S., Morii, M., et al. 2018, The Astrophysical Journal, 853, 46

Sedov, L. I. 1959, Similarity and Dimensional Methods in Mechanics

Serlemitsos, P. J., Soong, Y., Chan, K.-W., et al. 2007, Publications of the Astronomical Society of Japan, 59, S9

Shen, K. J., Boubert, D., Gänsicke, B. T., et al. 2018, The Astrophysical Journal, 865, 15

Short, A. D., Keay, A., & Turner, M. J. 1998, in Society of Photo-Optical Instrumentation Engineers (SPIE) Conference Series, Vol. 3445, EUV, X-Ray, and Gamma-Ray Instrumentation for Astronomy IX, ed. O. H. Siegmund & M. A. Gummin, 13–27

Stafford, J. N., Lopez, L. A., Auchettl, K., & Holland-Ashford, T. 2019, The Astrophysical Journal, 884, 113

Strüder, L., Holl, P., Lutz, G., & Kemmer, J. 1987, Nuclear Instruments and Methods in Physics Research A, 253, 386

Strüder, L., Briel, U., Dennerl, K., et al. 2001, Astronomy & Astrophysics, 365, L18

Takahashi, T., Kokubun, M., Mitsuda, K., et al. 2016, in Society of Photo-Optical Instrumentation Engineers (SPIE) Conference Series, Vol. 9905, Space Telescopes and Instrumentation 2016: Ultraviolet to Gamma Ray, ed. J.-W. A. den Herder, T. Takahashi, & M. Bautz, 99050U

Tanaka, T., Okuno, T., Uchida, H., et al. 2021, The Astrophysical Journal Letters, 906, L3

Tashiro, M., Maejima, H., Toda, K., et al. 2018, in Society of Photo-Optical Instrumentation Engineers (SPIE) Conference Series, Vol. 10699, Space Telescopes and Instrumentation 2018: Ultraviolet to Gamma Ray, ed. J.-W. A. den Herder, S. Nikzad, & K. Nakazawa, 1069922

Taylor, G. 1950, Proceedings of the Royal Society of London Series A, 201, 159

Toledo-Roy, J. C., Esquivel, A., Velázquez, P. F., & Reynoso, E. M. 2014, Monthly Notices of the Royal Astronomical Society, 442, 229

Townsley, L. K., Broos, P. S., Garmire, G. P., & Nousek, J. A. 2000, The Astrophysical Journal Letters, 534, L139

Townsley, L. K., Broos, P. S., Nousek, J. A., & Garmire, G. P. 2002, Nuclear Instruments and Methods in Physics Research A, 486, 751

Truelove, J. K., & McKee, C. F. 1999, The Astrophysical Journal Supplement Series, 120, 299

Tsebrenko, D., & Soker, N. 2013, Monthly Notices of the Royal Astronomical Society, 435, 320

Turner, M. J. L., Abbey, A., Arnaud, M., et al. 2001, Astronomy & Astrophysics, 365, L27

Uchida, H., Katsuda, S., Tsunemi, H., et al. 2019, The Astrophysical Journal, 871, 234

Velázquez, P. F., Vigh, C. D., Reynoso, E. M., Gómez, D. O., & Schneiter, E. M. 2006, The Astrophysical Journal, 649, 779

Vink, J. 2017, Supernova 1604, Kepler's Supernova, and its Remnant, ed. A. W. Alsabti & P. Murdin, 139

Vink, J., Kaastra, J. S., & Bleeker, J. A. M. 1997, Astronomy and Astrophysics, 328, 628

Warren, J. S., Hughes, J. P., Badenes, C., et al. 2005, The Astrophysical Journal, 634, 376

Webbink, R. F. 1984, The Astrophysical Journal, 277, 355

Weisskopf, M. C., Tananbaum, H. D., Van Speybroeck, L. P., & O'Dell, S. L. 2000, in Society of Photo-Optical Instrumentation Engineers (SPIE) Conference Series, Vol. 4012, X-Ray Optics, Instruments, and Missions III, ed. J. E. Truemper & B. Aschenbach, 2–16

Whelan, J., & Iben, Icko, J. 1973, The Astrophysical Journal, 186, 1007

Williams, B. J., Borkowski, K. J., Ghavamian, P., et al. 2013, The Astrophysical Journal, 770, 129

Williams, B. J., Borkowski, K. J., Reynolds, S. P., et al. 2012, The Astrophysical Journal, 755, 3

Williams, B. J., Coyle, N. M., Yamaguchi, H., et al. 2017, The Astrophysical Journal, 842, 28

Wilms, J., Allen, A., & McCray, R. 2000, The Astrophysical Journal, 542, 914

Woosley, S. E., & Weaver, T. A. 1994, The Astrophysical Journal, 423, 371

XMM-Newton Calibration Technical Note 0018, Version 3.12. 2019, ESA: EPIC Consortium, ed. M. J. S. Smith. `https://xmmweb.esac.esa.int/docs/documents/CAL-TN-0018.pdf`

XMM-Newton Users Handbook, Issue 2.19. 2021, ESA: XMM-Newton SOC, ed. J. Ebrero. `https://xmm-tools.cosmos.esa.int/external/xmm_user_support/documentation/uhb/XMM_UHB.html`

Yamaguchi, H., Acero, F., Li, C.-J., & Chu, Y.-H. 2021, The Astrophysical Journal Letters, 910, L24

Yamaguchi, H., Hughes, J. P., Badenes, C., et al. 2017, The Astrophysical Journal, 834, 124

Yamaguchi, H., Eriksen, K. A., Badenes, C., et al. 2014a, The Astrophysical Journal, 780, 136

Yamaguchi, H., Badenes, C., Petre, R., et al. 2014b, The Astrophysical Journal Letters, 785, L27

Yamaguchi, H., Badenes, C., Foster, A. R., et al. 2015, The Astrophysical Journal Letters, 801, L31

Zhou, P., Chen, Y., Zhang, Z.-Y., et al. 2016, The Astrophysical Journal, 826, 34

Acknowledgement

First, I want to start by thanking my supervisor Aya Bamba, and our group staff Hirokazu Odaka, Kazuhiro Nakazawa, and Kazuo Makishima. They have taught me not only specific subjects for studies of supernova remnants but also the basic principles as a scientist. I also appreciate all technical advice and mental support by all of the present and graduated members of our group, especially my group colleague Takahiro Matsumoto. In addition to them, I have never been able to carry out all of my studies for this five years without any administrative support by Kuniko Kono and Haduki Kutsuma.

Out of our group at the University of Tokyo, I want to especially thank Hiroyuki Uchida, who is the most important co-researcher of my studies described in this thesis. Without direct discussion with him, these studies would not have been achieved.

In my Kepler study, I give special thanks to Jacco Vink, who is my supervisor at de Universiteit van Amsterdam. He is very kind to me despite my poor English and gives me many valuable suggestions. Unfortunately, I couldn't work with him again in Amsterdam due to the COVID-19. These studies including older one are also helped by Tohsiki Sato, Satoru Katsuda, Hiroya Yamaguchi, John P. (Jack) Hughes, and Koji Mori. My short-term visiting research at de Universiteit van Amsterdam in the second half of 2019 was also supported by Ping Zhou, Hiroki Akamatsu, Shin'ichiro Ando, members of the SNR group in Anton Pannekoek Institute for astronomy, Sbarcea Oriana, and Chie Sakuta.

Concerning my Tycho study, I want to thank Takaaki Tanaka, Keiichi Maeda, Shiu-Hang (Herman) Lee, Takeshi "Go" Tsuru, Gilles Ferrand, and Shigehiro Nagataki for helpful discussions. As a preliminary step of this study, the technical problem written in the appendix section has been able to be found by the meaningful consultation with Hiromasa Suzuki and Paul P. Plucinsky. My short-term visiting research at Kyoto University in the second half of 2021 is also supported by members of the X-ray team in the Cosmic-Ray group, Toshihiro Fujii, Atsushi Takada, Hein Mallee, Takako Okamoto, and Shogo Benjamin Kobayashi.

Although we have not produced specific results, discussions with Hidetoshi Sano give me an interest in the circumstance environment of SNRs and other wave-length than the X-ray band. I also appreciate his setting of an opportunity for my visiting research at Nagoya University in the first half of 2019.

In addition to my astrophysical studies written in this thesis, I have parallelly proceeded with the development of the world first imaging polarimeter in the hard X-ray band, named "*cipher*" for these four years (e.g., Kasuga et al., 2019, 2020). From the launch of this project in my master thesis, I have been technically supported by Tadayuki Takahashi, Toru Tamagawa, Noriyuki Narukage, Shin-nosuke Ishikawa, Kiyoshi Hayashida, Yuanhui Zhou, and Asami Hayato.

As representatives of my Ph.D. colleagues, I thank Soichiro Hashiba first. He is a best friend at the department of physics at the University of Tokyo from the undergraduate period to this moment. I also thank some of my classmates at the Komaba period including Seiya Tanaka, Kana Moriwaki, Yosuke Ueno, Emari Ogawa, and Shun Suginome, who have done their own best in their research fields. Of course, I have enjoyed the intermission for chatting or blowing off our complains with a "flutist" Haruko Toyama.

This doctoral dissertation has been refereed by Takanori Yoshikoshi as the chief and Hiroyoshi Sakurai, Yasushi Suto, Fujihiro Hamba, and Masashi Yokoyama as the vice-referees. Their helpful suggestions improve this manuscript dramatically.

Finally, I greatly appreciate the all support of my family throughout my student life. I also thank all of my friends I've met, especially those whom I'm connecting through my musical activity by the violin and viola.

Tomoaki Kasuga,
December 2021